UNIVERSITY OF CALIFORNIA,
IRVINE

Quantification of Grain Boundary Mediated Plasticity Mechanisms in Nanocrystalline Metals

DISSERTATION

submitted in partial satisfaction of the requirements
for the degree of

DOCTOR OF PHILOSOPHY

in Mechanical and Aerospace Engineering

by

Jason F. Panzarino

Dissertation Committee:
Professor Timothy Rupert, Chair
Professor Yoonjin Won
Professor James Earthman

2016

DEDICATION

To my family,
Their hardworking nature and continuous encouragement
have been my greatest sources of motivation.

TABLE OF CONTENTS

Page

LIST OF FIGURES

ACKNOWLEDGEMENTS

First, I would like to thank my advisor, Professor Tim Rupert, who has guided me through the process of becoming a scientist. His help throughout my work at UC Irvine has been pivotal in all aspects of becoming an efficient researcher, from developing new ideas, to execution of experiments, to disseminating my research findings to the scientific community. In addition to his advice and encouragement during my time here, his easygoing nature has helped make my Ph.D. experience very enjoyable.

I would also like to thank the members of my thesis committee, Professor Yoonjin Won and Professor James Earthman. Their helpful criticisms and suggestions have given me invaluable insight which has helped me improve my thesis as well as my presentation skills.

I would also like to thank all of the members of the Rupert Lab for providing a great environment conducive to scientific discussion and an eagerness to assist fellow lab mates in need. I would especially like to thank Amirhossein Khalajhedayati, David Bober, and Zhiliang Pan for countless discussions which have helped me solve some of my most difficult research problems.

I would also like to acknowledge LEXI staff for their suggestions and training on several experimental techniques used throughout my time at UCI. Additionally, I would like to thank the Mazda Foundation and the Southern California Aero Club for generously providing scholarships which have helped support me during my graduate career.

Lastly, I would not have been able to complete this achievement without the amazing support of my friends. Their genuine motivation and vested interest into my success is supplemental to the fun that we have had during my time at UCI. Although there are many names

to mention, I would like to specifically thank Katie Dill and Daniel Howard. They play a much bigger role in my success than they probably know.

CURRICULUM VITAE

· EDUCATION/CERTIFICATIONS

University of California, Irvine Irvine, CA

2016 **Ph.D. in Mechanical & Aerospace Engineering**
Thesis: "Quantification of Grain Boundary Mediated Plasticity Mechanisms in Nanocrystalline Metals"
Advisor: Prof. Timothy J. Rupert

2014 **M.S. in Mechanical & Aerospace Engineering**
Concentration: Solid Mechanics & Structures

University of Florida Gainesville, FL

2012 **B.S. in Aerospace Engineering**
University Honors (all semesters)

Federal Aviation Administration

2007 FAA Licensed Private Pilot

· AWARDS AND HONORS

2015	UCI Engineering Student Council – MAE Graduate Student of the Year
2015	Aero Club of Southern California Graduate Scholarship 2015
2015	Experimental Aircraft Association 2015 Young Eagles Yearbook Recognition
2015	Mazda Foundation Fellowship Award
2015	Hysitron Presentation Silver Medal Award
2014	Aero Club of Southern California Graduate Scholarship 2014
2014	Graduate Assistance in Areas of National Need (GAANN) Fellowship Recipient
2013	University of California, Irvine Mech. & Aerospace Eng. Departmental Fellowship Recipient
2011	GA Tech. Space Shuttle Symposium, Univ. of FL representative
2009, 2010	Frederick W. & Grace P. Brecht Scholarship
2008	Grumman Retiree Club, George Skurla Memorial Scholarship
2008	Raytheon Scholarship Recipient
2008	Pratt & Whitney Scholarship Recipient
2008	Valedictorian, Melbourne High School
2006	Experimental Aircraft Association Chapter 1288 Flight Training Scholarship

· EMPLOYMENT

2012 **Intern, Launch Operations - United Launch Alliance** Cape Canaveral, FL

- Readied Delta IV vehicle propulsion and umbilical systems for several National Reconnaissance Office & GPS missions. Participated in final assembly, wet dress rehearsal, and launch of the Delta IV heavy NROL-15 mission.

2011 **Intern, Control Dynamics - United Launch Alliance** Denver, CO

- Researched the benefits of a new autopilot filter which provided the capability of multiple AtlasV vehicle configurations to be flown with the use of only a single gyro. Contributed to the control law configuration for the new common Atlas/Delta autopilot. In addition, performed space craft separation analysis to ensure proper orbit insertion of payload.

2010 **Intern, Factory Support Engineering - United Launch Alliance** Harlingen, TX

- Designed tools to help aid in the manufacturing of flight hardware for the ULA Atlas V and Lockheed Martin Terminal High Altitude Area Defense (THAAD) Programs. Assisted in developing solutions to recurring hardware nonconformance issues. Created 3-D cad models of all tools that were manufactured.

2008 **Aircraft Lineman, University Air Center** Gainesville, FL

- Tended to aircraft ranging from small single propeller piston planes to CRJ-700's. Responsible for marshalling, parking, & fueling all aircraft.

· UNDERGRADUATE RESEARCH

University of Florida

2011 - 2012 **Bend-twist Effects of Composite Shafts**

- Experimented with the effects and applications of bend-twist coupling on composite shafts. Used the data to help generate and verify analytical models of composite pipes whose plies are specifically oriented to generate this effect. Extensive testing of an awarded patent to implement this technology in golf club shafts for improved shot accuracy.

2009 – 2010 **Unmanned Aerial Systems / Army Corps of Engineers**

- Performed unmanned aerial vehicle research funded by the Army Corps of Engineers under Dr. Peter Ifju. Assisted in construction of an amphibious unmanned aerial vehicle out of composite materials that is capable of autonomous flight and navigation along pre-programmed paths. The airplane carried a payload consisting of a high resolution camera and infrared sensors for photographing and documenting wildlife in the everglades.

· PUBLICATIONS

Journal Articles:

- **Panzarino JF,** Pan Z, Rupert TJ. "Plasticity-induced restructuring of a nanocrystalline grain boundary network," *Acta Materialia* (2016) In Press. (http://arxiv.org/abs/1604.00088)

- **Panzarino JF**, Ramos JJ, Rupert TJ. "Quantitative tracking of grain structure evolution in a nanocrystalline metal during cyclic loading," *Modelling and Simulation in Materials Science and Engineering*, 23, 025005 (2015). (http://dx.doi.org/10.1088/0965-0393/23/2/025005)
- **Panzarino JF**, Rupert TJ. "Tracking Microstructure of Crystalline Materials: A Post-Processing Algorithm for Atomistic Simulations," *JOM*, 66, 417 (2014). (http://dx.doi.org/10.1007/s11837-013-0831-9)

· PRESENTATIONS

- **Panzarino JF,** Rupert TJ. "Plasticity-induced Restructuring of Nanocrystalline Grain Boundary Networks," *Materials Science & Technology 2016*, October 2016, Salt Lake City, UT
- **Panzarino JF**, Rupert TJ. "Mapping grains and interface networks in atomistic simulations: Tracking dynamic nanocrystalline microstructures," *The Minerals, Metals and Materials Society (TMS) Annual Meeting & Exhibition*, March 2015, Orlando, FL.
- **Panzarino JF**, Rupert TJ. "Tracking Microstructure Evolution in Crystalline Materials: A Post Processing Algorithm for Atomistic Simulations," *The Minerals, Metals and Materials Society (TMS) Annual Meeting & Exhibition*, February 2014, San Diego, CA.

***Contributed Presentations** (Presenters name is in bold):*

- **Bustamante J**, Panzarino JF, Rupert TJ, Loudon C. "Characterization of material properties of bed bug cuticle (Cimex lectularius)," *Society of Integrative and Comparative Biology (SICB) Annual Meeting*, January 2015, West Palm Beach, FL.
- **Bober DB**, Panzarino JF, Rupert TJ. "Nanocrystalline Grain Boundary Engineering: Experiments and Atomistic Modeling," *Materials Research Society (MRS) Fall Meeting*, November 2014, Boston, MA.
- **Bustamante J**, Panzarino JF, Rupert TJ, Loudon C. "Characterization of material properties of bed bug cuticle (Cimex lectularius)," *Entomological Society of America (ESA) Annual Meeting*, November 2014, Portland, OR.

· UNIVERSITY TEACHING EXPERIENCE

University of California, Irvine - Department of Mechanical & Aerospace Engineering

Winter 2016	MAE 157 Lightweight Structures (Teaching Assistant)
Winter 2014	MAE 157 Lightweight Structures (Teaching Assistant)

University of Florida - Department of Mechanical & Aerospace Engineering

Spring 2011	Advanced Aerospace Composites (Teaching Assistant)

· OUTREACH/VOLUNTEER ACTIVITIES

- ***Team Lead – Rescue Robotics Samueli High School*** – Lead an after school quadcopter robotics team consisting of several tenth graders. Build test and fly an autonomous quadcopter for a collegiate level search and rescue competition. 2nd Place in design competition for two consecutive years (2015-Present)
- ***Instructor - Rocket Science Tutors –*** Conduct weekly after school science lessons/experiments at various underrepresented middle schools in the Santa Ana school district. Classes are designed to engage students in Science, Technology, Engineering, & Math (STEM) and help to spark their interest in these fields. Experiments vary from rocketry, to electricity, to chemistry. (2012 – present)
- ***Young Eagles Program – Experimental Aircraft Association*** – Help to coordinate and execute community flying events which provide free flights to children. Teach youth about aviation and flight mechanics. (2006 – present)
- ***Alpha Phi Omega – National Service Fraternity*** – Weekly Volunteer & Community outreach activities ranging from elderly care to after school tutoring. 100 + Hours, Gainesville, FL (2010-2011)
- ***AIAA Aerospace Day*** – Coordinated an aerospace engineering day for 3 local middle schools to visit the University of Florida engineering department to conduct rocketry and engineering science. (2010,2011)
- ***Brevard Alzheimer's Foundation –*** Fundraising volunteer & foundation landscaper (2008)

· PROFESSIONAL DEVELOPMENT

Elected Positions:

- ***Experimental Aircraft Association (EAA)***
  EAA chapter 92 Orange County Chapter - *Membership Chair & Board of Directors 2016*
  EAA chapter 92 Orange County Chapter - *Membership Chair 2015*
- ***American Institute of Aeronautics & Astronautics (AIAA)***
  Student Chapter, University of Florida - *President (2011), VP (2009 & 2010)*

Current Memberships:

- ***American Society for Metals (ASM)*** *Irvine, CA*
- ***Experimental Aircraft Association (EAA) Chapter 92*** *Irvine, CA*
- ***Aero Club of Southern California*** *Los Angeles, CA*

· MENTORSHIP

Undergraduate Researchers:

· Carlos Ramirez	UC Irvine, MAE	Spring 2015 –2016
· Jim Mendez-Lopez	UC Merced, MAE	Summer 2015

· Jesus Ramos	UC Irvine, MAE	Fall 2013 – Spring 2014

High School Researchers:

· Rocky Mandayam	Irvine High School	Summer 2013 –2014

· SKILLS

MATLAB (5000+ Hours)
Microscopy SEM/TEM
Focused Ion Beam Sample Preparation, Mechanical & Chemical Sample Preparation
X-ray Diffraction, Nanoindentation
Molecular Dynamics Simulations
Pro Engineer, Solid Works
FEA/Abaqus
Electrodeposition, Composite Materials Layup/Design

ABSTRACT OF THE DISSERTATION

Quantification of Grain Boundary Mediated Plasticity Mechanisms in Nanocrystalline Metals

By

Jason F. Panzarino

Doctor of Philosophy in Mechanical & Aerospace Engineering

University of California, Irvine, 2016

Professor Timothy J. Rupert, Chair

Nanocrystalline metals have been a topic of great discussion over recent years due to their exceptional strengths and novel grain boundary-mediated deformation mechanisms. Their microstructures are known to evolve through dynamic processes such as grain boundary migration and grain rotation, but how the collective interaction of these mechanisms alter the microstructure on a larger scale is not completely understood. In this thesis, we present coupled atomistic modeling and experimental tasks that aim to understand how the grain structure, grain boundaries, and associated grain boundary network change during nanocrystalline plasticity. Due to the complex three-dimensional nature of these mechanisms and the limited spatial and temporal resolution of current in-situ experimental techniques, we turn to atomistic modeling to help understand the dynamics by which these mechanisms unfold. In order to provide a quantitative analysis of this behavior, we develop a tool which fully characterizes nanocrystalline microstructures in atomistic models and subsequently tracks their evolution during molecular dynamics simulations. We then use this algorithm to quantitatively track grain structure and

boundary network evolution in plastically deformed nanocrystalline Al, finding that higher testing temperature and smaller average grain size results in increased evolution of grain structure with evidence of larger scale changes to the grain boundary network also taking place. This prompts us to extend our analysis technique to include full characterization of grain boundary networks and rigorous topographical feature identification. We then employ this tool on simulations of Al subject to monotonic tension, cycling loading, and simple annealing, and find that each case results in different evolution of the grain boundary network. Finally, our computational work is complemented synergistically by experimental analyses which track surface microstructure evolution during sliding wear of nanocrystalline Ni-W thin films. These experiments track the development of a surface grain growth layer which evolves through grain boundary mediated plasticity and we are able to make direct connections between this evolution and that which was observed in our simulation work. All of the findings of this thesis are a direct result of the dynamic and collective nature by which nanocrystalline materials deform.

CHAPTER 1. Introduction

1.1 Motivation

The push for lighter, stronger, and application-based materials will forever exist in the development of new technologies for the mechanical & aerospace industries. Increased ingenuity and performance requirements have resulted in a wide understanding of bulk material response on the macroscale. In order to achieve substantial advancements in materials development, researchers must look internally within the microstructure in order to tailor material properties for their specific engineering applications and designs. In the words of the famous talk by physicist Dr. Richard Feynman, "there's plenty of room at the bottom," with his lessons largely responsible for the concept of bottom-up, atomic-scale design of materials and thus the field now known as Nanotechnology. By observing the interactions taking place deep within the microstructure of materials and understanding deformation at the atomic level, researchers can more efficiently engineer the arrangement of atoms in order to optimize bulk material response.

1.2 Mechanical Properties of Nanocrystalline Metals: A shift in deformation mechanisms

Nanostructured metals are a class of materials with structural features smaller than 100 nm and they frequently exhibit novel characteristics across a wide range of properties including increased hardness [1], super plasticity [2] and electrical conductivity [3]. The altered response of such properties is a direct consequence of the nano-scale microstructural arrangements of the atoms themselves. For nanocrystalline metals, atoms are arranged in polycrystals with an average

grain diameter (*d*) within the 100 nm range. Regarding engineering design, these metals pose significant promise as next generation structural materials due to reported increases in ultimate strength [4, 5], resistance to fatigue [6, 7], and wear resistance [8, 9]. The discoveries of many of these mechanical advantages are a resulting consequence of instrumental work by Hall [10] and Petch [11] in the 1950's, whose independent research confirmed the relationship between grain size and strength of metals, leading to increased scientific interest in grain refinement. The Hall-Petch relation predicts that strength is inversely proportional to grain size, explaining why nanocrystalline metals can exhibit strengths approaching their theoretical limits as grains are refined. The Hall-Petch relation is given as follows:

$$(1)\ \sigma_y = \sigma_0 + \frac{k}{\sqrt{d}}$$

Where σ_y is the yield strength, σ_0 is a material constant pertaining to the resistance of the lattice to dislocation motion (starting stress), *k* is the strengthening coefficient, and *d* is the average grain diameter. The Hall-Petch relationship essentially describes grain boundary strengthening, a process by which grain boundaries, or regions between crystallites of different lattice orientation, act as physical barriers for continued dislocation movement within the material. For more traditional, course grained materials consisting of average grain sizes ranging from 100 nm upwards of several microns, gliding dislocations act as the main carriers of plasticity. For this reason, as grain size is decreased, significant strengthening can be expected. For example, Figure 1-1 illustrates the mechanical response of ball-milled and hot pressed aluminum powders containing a range of grain sizes. It can be clearly seen that as the average grain size falls below 100 nm, significantly higher ultimate strengths can be attained, albeit with a decrease in ductility.

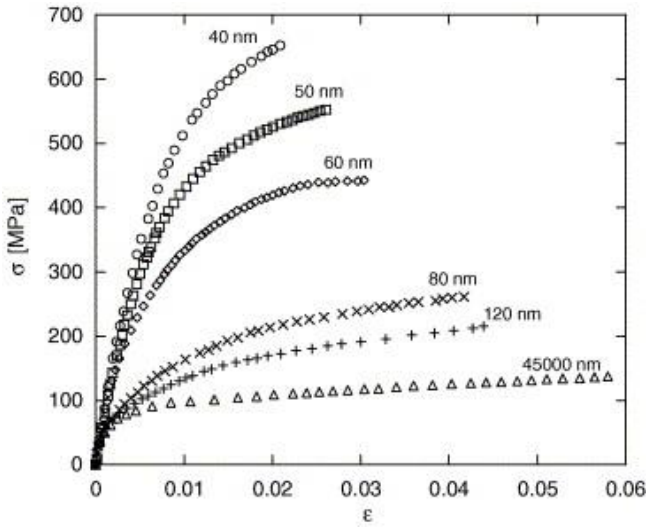

Figure 1-1 True stress-strain curves for nanocrystalline Al of varying grain sizes tested at a constant strain rate. Samples were created using ball milling before being tested in compression [12].

Interestingly, grain size strengthening has its limits, and this trend begins to break down near the d ~ 100 nm mark, with many studies reporting a plateau in strengthening or even an inverse Hall-Petch behavior which results in softening of the material[13]. For example, El-Sherik and colleagues [14] observed a plateau in Vickers hardness of electroplated nanocrystalline Ni with average grain sizes varying from 100-10 nm with the linear increase in hardness values tapering off below d~25 nm. Chokshi et al. [15] analyzed hardness values for polycrystalline Cu and Pd with average grain sizes varying from 16 nm down to 6.25 nm and found an inverse relationship of strength to grain size. Trelewicz and Schuh [16] observed the full breakdown from strengthening, to plateau, and then softening for a range of 150-3 nm Ni-W alloys. While initial causes of softening were believed to be manufacturing or testing artifacts, this idea has been ruled out with the emergence of more and more studies which report such a breakdown in Hall-Petch behavior, confirming it is in fact a real phenomenon [17].

One common feature of many of these studies is the fact that the transition in properties occurs once the average grain size falls below a certain point, although the exact grain size can be

difficult to pinpoint experimentally and should vary slightly for each material system. The majority of studies report the transition beginning below ~100 nm with the inverse relationship appearing at even finer grain sizes near 10-30 nm. Regardless of the exact transition points, it has been verified that the reason for such changes are due to the increased volume fraction of grain boundary material present in nanocrystalline systems as indicated by Figure 1-2(a). These abnormally high volume fractions of non-crystalline material exaggerate the importance of the grain boundaries, ultimately leading to a shift in the physical plasticity mechanisms which take place during deformation. Figure 1-2(b) highlights the changes in flow strength of a general material as the grain size is reduced, indicating that the dominant plasticity mechanisms are changing from traditional intragranular dislocation interactions to the emergence of new "grain boundary mediated" plasticity mechanisms such as grain boundary mediated dislocations, grain boundary sliding, and grain rotation. Observation and documentation of these new mechanisms, which are ultimately responsible for the disturbances in the Hall-Petch scaling trend, are discussed in the following section.

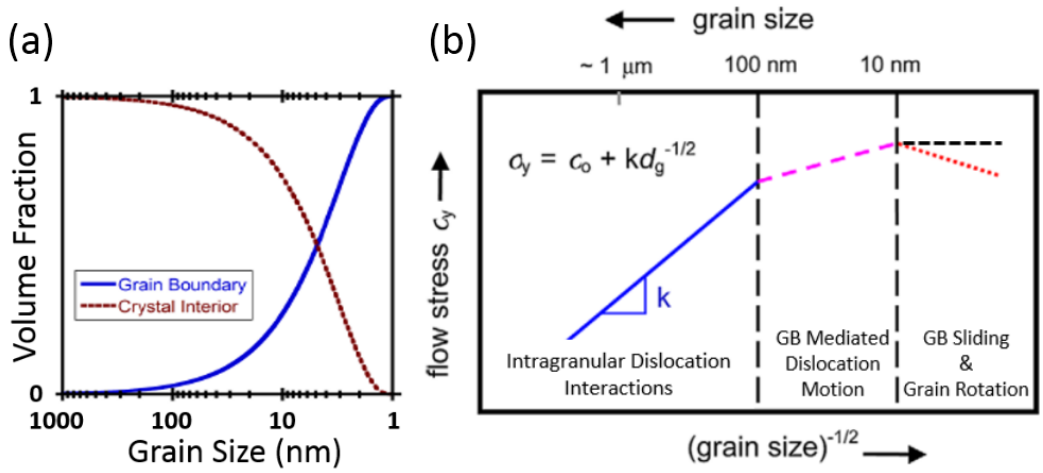

Figure 1-2 Hall-Petch relationship describing flow stress as a function of grain size (adapted from [1]).

1.3 Observing and Understanding Grain Boundary Mediated Plasticity

At the smallest grain sizes traditional intragranular dislocation based mechanisms begin to shut off which leads to the dominance of grain boundary mediated mechanisms. Because this transition begins to take place at such small length scales, direct observation has been difficult to achieve experimentally. Fortunately, recent technological advancements have allowed for direct evidence of the emergence of new physical processes such as grain rotation [18-21], and grain boundary migration [22, 23]. For example, Harris et al. [21] used transmission electron microscopy (TEM) to observe rotated grains in gold thin films which were subjected to annealing. Additionally, improvements in in-situ automated orientation crystal mapping (ACOM) have been combined with precession enhanced electron diffraction inside a TEM in order to achieve extremely high resolution texture maps. Kobler et al. [24] were able to use this in-situ technique to obtain nanoscale crystal orientation maps during several stages of deformation allowing for quantification of grain growth and orientation changes during their experiment. Figure 1-3 shows three consecutive maps from their study with an interesting grain pointed out by a black arrow in the first map. As the foil was strained the change in color of the grain corresponds to a change in lattice orientation, providing direct evidence of grain rotation. Unfortunately, the resolution of the technique by Kobler et al. [24] was limited to grain sizes above 15 nm with data confidence further limited by sample thickness since a sample with multiple grains in the beam direction will provide a convolution of the underlying texture present. Another important note is that such TEM orientation maps can only give two-dimensional maps of the microstructure. Since a grain's rotation and sliding with respect to its neighbors is likely a complicated three-dimensional process,

techniques which can track structural changes in all spatial dimensions would be extremely useful for observing the intricacies of how these new processes develop during plasticity.

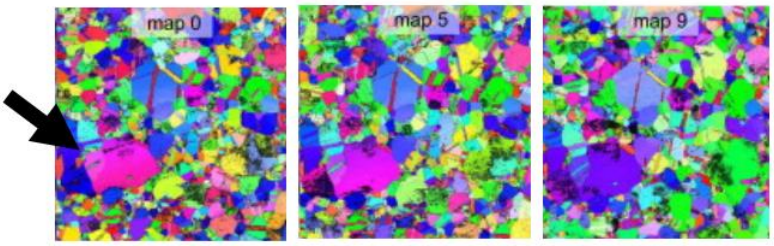

Figure 1-3 *In-situ* study which utilizes ACOM to study grain rotation in gold thin films with resolution approaching 15 nm (figure adapted from [24]) .

Fortunately, atomistic simulations provide researchers with a level of spatial and temporal resolution that cannot be matched experimentally. The three-dimensional nature of these data sets provide the exact position of all atoms so that researchers may visualize dynamic changes to the microstructure during the entirety of deformation. A widely used technique for simulating material deformation is to employ molecular dynamics (MD) simulations, however, these simulations are not without limitation. In order to accurately capture atomic processes, one must utilize an extremely small time step (~1 femtosecond) which in turn means that an impossible amount of integration time steps will have to be carried out in order to simulate realistic strain rates. In order to limit the number of time steps to tens of millions (simulating a few nanoseconds) MD simulations require unusual strain rates in the range of 10^{7} - $10^{10}s^{-1}$. Despite these limitations, careful consideration of the simulated results alongside proper selection of an adequate interatomic potential can produce invaluable insight for materials researchers. This insight can be used to help explain and model the behaviors that are being seen in nanocrystalline materials and expedite experimental validation of such processes.

1.3.1 Uncovering New Plasticity Mechanisms with Molecular Dynamics Simulations

Molecular dynamics (MD) simulations have been a valuable resource in studying these new mechanisms of crystal plasticity which take place at the smallest length scales within the nano regime. Schiotz et al. [25] used MD to analyze tensile deformation of nanocrystalline Cu with grain sizes ranging from 3.28 to 13.2 nanometers. By quantifying the motion of all atoms relative to homogeneous deformation the authors were able to observe that the majority of plasticity was being accommodated by grain boundary activity, as can be seen in Figure 1-4(a). This snapshot, taken after deformation of the sample, indicates downward relative movement as blue and upward as red with the majority of the color gradient appearing in the interfaces between grains. Additionally, grain rotation was manually calculated in a select number of grains using a Fourier transform of the atomic positions, also confirming that rotation was indeed taking place during sample elongation. Schiotz et al. [25-27] have performed other pioneering works which probe the microstructural evolution of nanocrystalline materials in the same manner, shedding light on grain coarsening, strain-rate dependency, and flow strength.

This type of atomistic analysis has gained significant popularity in the scientific community for uncovering a variety of new boundary mediated plasticity mechanisms. Van Swygenhoven and Derlet [28] utilized MD to observe grain boundary sliding which was accommodated by atomic shuffling within the grain boundaries along with stress-assisted free volume migration. Additionally, Van Swygenhoven and coworkers [29] were also able to uncover the relationship between generalized planar fault energy and how it plays a role in partial dislocation emission and absorption from grain boundaries, a slip mechanism which is unique to that of the nanocrystalline metals [30-32]. Figure 1-4(b) and (c) illustrate the emission of partial

dislocations from the grain boundary, leaving behind stacking defects indicated by red atoms within the grain.

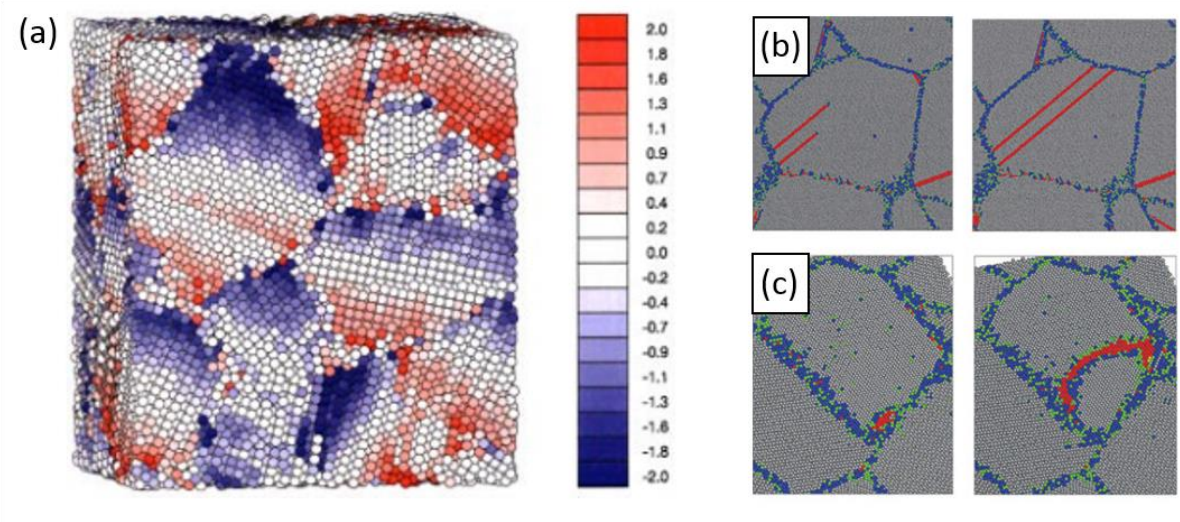

Figure 1-4 (a) Nanocrystalline sample deformed to 10% true strain with atoms colored by displacement relative to homogeneous displacement [25]. (b)-(c) indicate instances where dislocation activity originated from the grain boundaries. (c) is a view perpendicular to the faulted region (red) in which is bounded by leading and trailing shockley partials [29].

Unfortunately, the vast majority of characterization in atomistic modeling consists of the calculation of local properties of each atom, such as energy, stress, or local lattice distortion, and qualitative observations, such as the migration of a certain grain boundary or the rotation of a specific grain. Even though atomic metrics exist which can determine crystal structure, potential energy, and bonding neighborhood [33], the majority of past works have required the manual calculation and detection of important larger scale structural features such as grains and interface types. Since the exact locations of all atoms is known throughout deformation, all of the required data is available to calculate such features, however, until recently there have been no automated tools available to researchers for identifying such features in a quantitative manner, making this type of data extraction a manual task that can be tedious and time consuming.

1.3.2 Toward a Quantitative Analysis of Nanocrystalline Plasticity

Quantification of microstructural evolution through rigorous feature tracking would provide valuable insight into how these mechanisms play a role in overall microstructural rearrangement. A number of computational materials scientists have recently acknowledged this limitation and have started working to develop tools for quantifying structure in atomistic simulations. For example, Stukowski and colleagues have created a crystal analysis tool that can identify both lattice [34] and grain boundary dislocations [35], providing the full dislocation network including Burgers vectors and dislocation junction information. An example of such a calculated network can be seen in Figure 1-5(a) during the simulated nanoindentation of a Σ11 bicrystal where dislocation lines are colored according to type [35]. In work that is closer to the goal of analyzing nanocrystalline materials directly, Tucker and Foiles have also developed a technique for finding individual grains within a polycrystalline sample, allowing for quantitative measurements of grain size [36]. Barrett et al. [37] and Tucker et al. [38] have also developed metrics which can identify hexagonal basal plane vectors and microrotation vectors for all atoms, respectively. Xu and Li [39] have developed their outward-layering algorithm which is capable of extracting microstructural features such as grains, grain boundaries, triple junctions, and vertex points from polycrystalline samples, with an example of a post-identified structure illustrated in Figure 1-5(b). Some authors have gone an alternative route by simulating scattering physics in order to characterize microstructure, with Derlet et al. [40] and Coleman et al. [41] developing techniques for producing virtual diffraction profiles from atomistic data. An example of a [010] low-angle symmetric tilt grain boundary with the accompanying selected area electron diffraction (SAED) pattern can be seen in Figure 1-5(c).

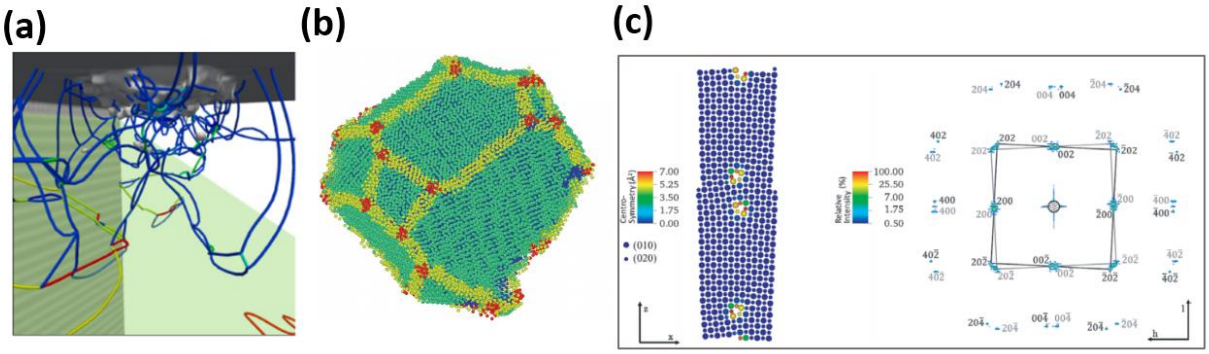

Figure 1-5 (a) Dislocation network extracted using the Crystal Analysis Tool developed by Stukowski et al. [35] (b) Outward layering developed method by Xu & Li [39] which can identify microstructural attributes such as grain interior atoms which are colored blue, boundary atoms green, triple junction atoms yellow, and vertex points red [39]. (c) [010] symmetric tilt grain boundary which has been analyzed using the virtual diffraction technique of Coleman et al. [41] with the corresponding SAED pattern.

These algorithms have begun to allow a more quantitative approach to post processing of atomistic data, resulting in a variety of studies which can then quantify the relative contributions of each mechanism and allow more accurate understanding of how these mechanisms collectively rearrange the microstructure and affect material properties of nanocrystalline materials. For example, Vo et al. [42] utilized localized slip vectors in order to quantify the relative amounts of different dislocation activity that contribute to the overall strain within polycrystalline Cu consisting of average grain sizes varying from 5-20 nm. A visual representation of their compressed sample is shown in Figure 1-6(a). The colors indicate which atoms belong to partial (green) and perfect (red) dislocation slip traces allowing for volumetric measurements of the contribution of each activity to the overall plastic strain. A recent study by Tucker and Foiles [43] used kinematic metrics to compute atomically-resolved rotation and strain fields across columnar nano-twinned Cu samples under tension and compression. They were then able to use this information to quantitatively resolve the total strain accommodation within the microstructure and elucidate how varying the number of twins plays a role in each individual contribution. Figure

1-6(b) shows the relative strain contributions for both tension (closed circles) and compression (open circles) of highly twinned samples caused by the nucleation and/or motion of different defect types through the microstructure. An image of the twinned microstructure fully deformed in tension is included at the top of Figure 1-6(b). The ability to characterize three-dimensional microstructures in this fashion will allow for new structure-property correlations to be drawn and enable microstructure-mediated design [44], allowing for more widespread use of these nanocrystalline materials in engineering designs.

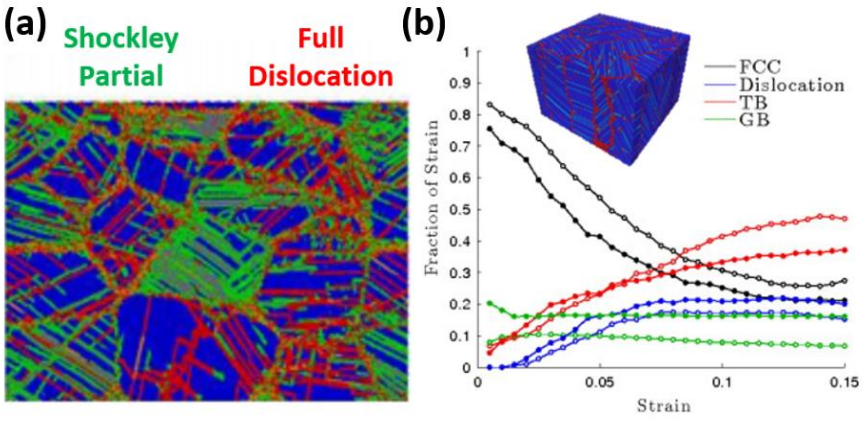

Figure 1-6 (a) Nanocrystalline sample subject to compression showing the relative contributions to plastic strain from partial and full dislocation activity within the microstructure (adapted from [42]). (b) Relative fractions of contributions to strain due to the nucleation and migration of several types of defects and the effect of nanoscale twins (adapted from [43]).

1.4 Problem Statement and Research Objectives

All of these examples illustrate the power of quantitative analyses of these structures, however, there is still more work to be done. To date, the majority of these tools only provide defect and crystallite structure information, leaving out grain boundary characterization and topological arrangement of the grain boundary network. Additionally, since these novel nanocrystalline plasticity mechanisms are also very dynamic in nature, the ability to track their

progress during plasticity is a key element in facilitating our understanding of how they work. Knowing that plasticity of nanocrystalline metals is ultimately dictated by the grain boundaries themselves, it is also apparent that the structure and connectivity of the grain boundary network will play an important role in determining how these processes interact to evolve the microstructure. Tools which characterize not just grain structure evolution but also the associated grain boundary network evolution must be developed for understanding plasticity in ultrafine nanocrystalline materials. Once this is accomplished these tools can then be used to understand how grain boundary mediated mechanisms collectively evolve the microstructure during plasticity. Finally, the knowledge gained from such computational work can be used to guide experimental validation and help to hypothesize and explain what is taking place during experimental investigations of nanocrystalline plasticity.

This thesis addresses the concerns made in the preceding paragraph with the steps taken to achieve these goals outlined in the following chapters:

- Chapter 2: Since quantitative tools for identifying crystallites, their crystallographic orientation, and overall sample texture do not exist, we develop a post-processing algorithm capable of characterizing such features and test the utility of the algorithm on several atomistic examples which are commonly found in the literature.
- Chapter 3: Molecular dynamics simulations are used to quantify mechanically-induced structural evolution in nanocrystalline Al. A polycrystalline sample is cyclically strained at different temperatures, and our algorithm is used to measure the relative contributions of deformation mechanisms such as grain rotation and grain sliding. Our focus is to

understand the collective nature by which grain boundary mechanisms alter grain structure and mechanical properties at different temperatures.

- Chapter 4: Since grain boundary-mediated mechanisms directly alter the interfacial structure between crystals, our algorithm is updated to include boundary network characterization. We employ molecular dynamics simulations on nanocrystalline Al to quantitatively study the evolutions of grain boundary character distribution, triple junction type, grain boundary plane normal, and other interfacial network characteristics during several modes of plastic deformation. Grain size is also varied in an attempt to capture a crossover in the activation of grain boundary plasticity mechanisms.
- Chapter 5: The underlying grain structure evolution of an electrodeposited Ni-W alloy is explored with nanoscratch testing used as a driver for cyclic plasticity. The subsurface microstructure is characterized throughout development in order to track grain structure evolution during plasticity and any synergy between the experiments and our previous simulations is addressed.

CHAPTER 2. Tracking Microstructure of Crystalline Materials: A Post-processing Algorithm for Atomistic Simulations[1]

2.1 Introduction

In order to facilitate the location and extraction of important structural features within crystalline materials, post processing tools must to be developed which can filter through the enormous atomistic datasets and output truly quantitative analyses of the underlying evolution. This will not only allow for immediate detection of important structural features, but also help researchers discover microstructure-property relationships. We therefore aim to add to the toolbox currently available to researchers an analysis technique which can identify and track crystallites, their crystallographic orientation, and overall sample texture. We have developed an original post-processing tool which identifies all crystalline grains and precisely calculates grain orientations with no a priori knowledge of the simulated microstructure. In addition, the algorithm also defines a mapping between simulation time steps, allowing for the analysis of individual grain movement, rotation, or coalescence as time progresses. In the present chapter, we explain the details of this algorithm, while also providing several case studies showing its utility for characterizing and visualizing microstructural features in atomistic simulations.

2.2 Analysis Methods

The *grain tracking algorithm* (GTA) presented in this chapter consists of five principle steps:

[1] The contents of this chapter have been previously published as Panzarino JF & Rupert TJ. JOM 65(3): 417-428.

(i) Crystalline atoms in the simulation set are identified by centrosymmetry parameter (CSP) [45], common neighbor analysis (CNA) [46, 47], or any other comparable measurement which can identify defects in local crystalline structure such as bond angle analysis [48] or neighbor distance analysis [33].

(ii) The local crystallographic orientation of each atom in a crystalline environment is calculated using the geometry of the material's unit cell.

(iii) Individual crystallites are identified by an iterative process where nearest neighbors must have similar crystallographic orientations to be included in the same grain.

(iv) Grains are indexed and tracked over time using the center of mass of each crystallite.

(v) The measured orientation of each grain and the overall sample texture are visualized with pole figures, inverse pole figures, and orientation maps. We aim to recreate the familiarity of experimental visualization methods and better integrate atomistic datasets into Integrate Computational Materials Engineering.

It is important to note that the GTA is largely a generic algorithm that can be applied to any crystalline material regardless of the crystal structure. In this chapter, we describe the algorithm's implementation for face centered cubic (fcc) crystals, although only minor modifications to Steps (ii) and (v) would be necessary to analyze other crystal structures. The algorithm is currently implemented as MATLAB code, which has been made available as and open-source tool to the scientific community.

2.2.1 Atom Classification

The first step in our GTA method is the separation of atoms based on their local environment. Specifically, we classify atoms as *grain interior*, *grain edge*, or *non-crystalline*.

Many techniques for local structural analysis exist, and a detailed discussion of the advantages of each method can be found in a recent article from Stukowski [33]. While any of these metrics can be used with our algorithm, we focus here on CSP and CNA as potential techniques for defect identification, due to their widespread usage in the literature and because they are built into common MD simulation packages such as the Large-scale Atomic/Molecular Massively Parallel Simulator (LAMMPS) code [49].

A centrosymmetric lattice, such as fcc or body centered cubic (bcc), has pairs of equal and opposite bonds between nearest neighbors. CSP measures the deviation from this perfect centrosymmetry and can be used to identify defects when a threshold value associated with thermal vibrations is exceeded. One method for determining an appropriate threshold for defect identification is the Gilvarry relation [50], which places an upper limit on the thermal vibrations a crystal can experience before it melts (~12% of the nearest neighbor distance), but such a distinction is not perfect and the CSP method struggles with false positives in defect identification at high temperatures. However, the CSP metric is well-suited for analyzing highly strained atomistic systems, as it is not sensitive to homogeneous elastic deformation. Alternatively, CNA analyzes the topology of the bonds within a cut-off distance around an atom and assigns a structural type (fcc, bcc, hexagonal close packed (hcp), or unknown structure are the distinctions which are commonly used) to the atom in question. Therefore, any atom with a structure different than that expected for the material can be classified as a defect. For example, when analyzing fcc Ni, all bcc, hcp, and unknown atoms would be considered defects. CNA tends to be less sensitive to thermal vibrations, but large elastic strains can pull the nearest neighbors outside of the cut-off distance for analysis. Hence, the CNA metric is most useful when dealing with materials at high temperatures but struggles with highly strained systems.

Using either CSP or CNA in its current formulation, the GTA first identifies defect atoms and labels them *non-crystalline*. We then further sort the remaining crystalline atoms by examining the nearest neighbors. If all of an atom's nearest neighbors (12 in the case of fcc) are also in a crystalline environment, then the atom is labeled *grain interior*. Alternatively, if one or more nearest neighbor is non-crystalline, then the atom in question is labeled *grain edge*. This distinction ends up being important for identifying grains and avoiding large errors in the calculated orientation of the crystallites. Figure 2-1 shows a polycrystalline Al atomistic sample, with atoms separated into grain interior, grain edge, and non-crystalline.

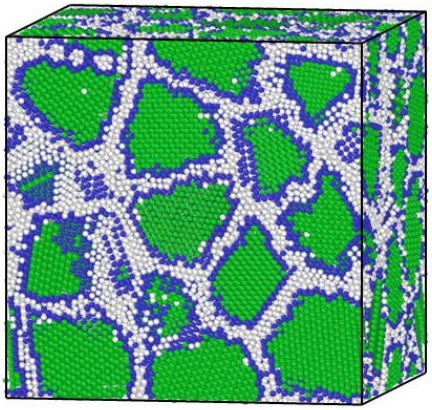

Figure 2-1 Nanocrystalline Al atomistic sample, with atoms separated into grain interior (green), grain edge (blue), and non-crystalline (white). CSP was used to find defective atoms, and the non-crystalline atoms are all grain boundary atoms since there is no stored dislocation debris.

2.2.2 Local Crystallographic Orientation

Once all atoms in grain interior environments have been found, we calculate the local orientation of each atom based on the unit cell of the material. The process of determining the local orientation at each atom is highlighted in Figure 2-2(a) for an fcc material. The nearest neighbors of an atom must be found, and then an arbitrary vector is chosen in the direction of one of these neighbors. For an fcc lattice, there will be four other neighbors whose directional vectors

will lie approximately 60° from the original arbitrary vector. These four new vectors will reside in two separate {100} planes of the unit cell, with each plane containing a pair of nearest neighbors and a <100> direction which must be perpendicular to its counterpart. The cross product of these two <100> directions then gives the third <001> direction. Finally, we find the inverse of these three vectors as well, giving all six <100> axes of the unit cell. The local orientation of the atom is now described fully and can be stored. This calculation is repeated for each grain interior atom, providing crystal orientation as a function of position within the atomistic sample. It is important to note that any periodic boundary conditions must be enforced before this calculation, in order to avoid errors in atoms near the boundaries of the simulation cell. Our code takes care of this requirement by adding virtual images of the simulation cell when necessary.

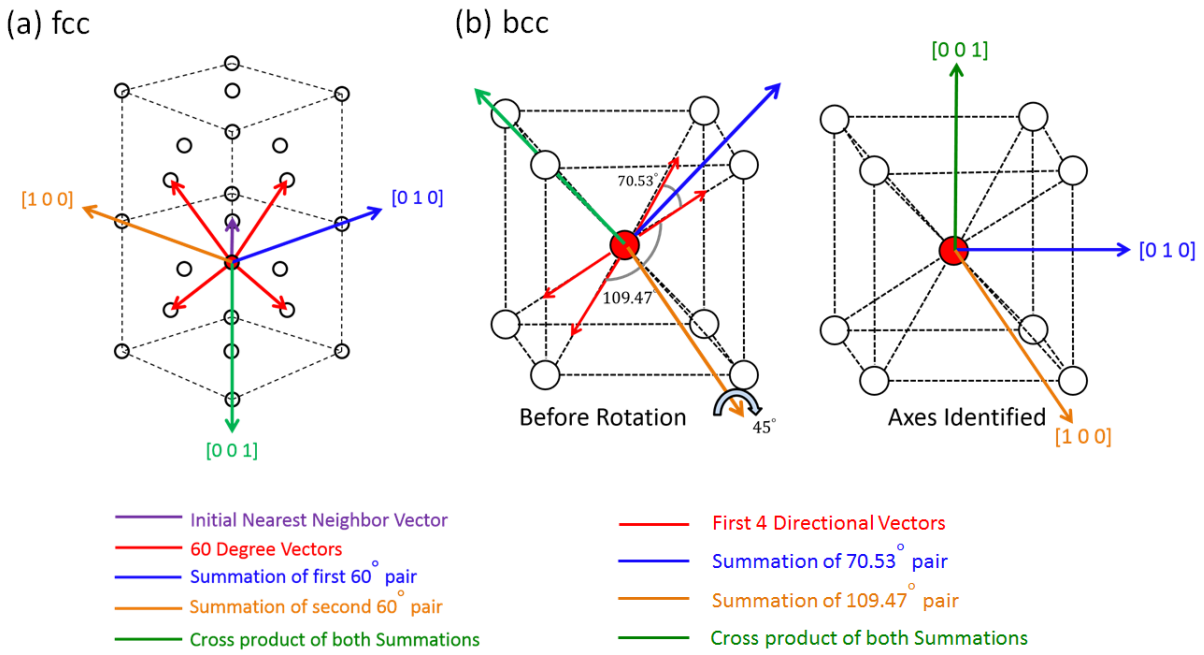

Figure 2-2 (a) A schematic of atoms in two stacked fcc unit cells which illustrates the process of calculating the local crystallographic orientation of an atom. The inverse of the three calculated <100> directions must also be taken to find all six <100> directions. (b) A similar schematic illustration of the process used to find the orientation of atoms in bcc environments. Again, all <100> directions are found and uses to store orientation information.

While the exact description provided above is unique to an fcc lattice, only small changes are required for other lattice structures. For example, if the equilibrium crystal structure is bcc, then a similar method for finding the local orientation can be employed and is outlined in Figure 2-2(b). We start by calculating the vectors connecting our atom of interest to its 8 nearest neighbors. Then, we can select two of the nearest neighbor vectors and their inverse vectors which are 180° away, giving four vectors which lie in a {110} plane. Next, we separate the pair of vectors which are 109.47° apart from the other pair that lies 70.53° apart. Adding the vectors in each pair gives the blue and orange axes shown in Figure 2-2(b), and the cross product of these vectors gives the green axis. Because our vector algebra has been done on a {110} plane up until this point, we only need to rotate this new orthogonal coordinate system by 45° about the orange axis vector to find three <100> directions and obtain the center atom's local crystallographic orientation.

2.2.3 Grain Identification

After orientations are calculated for every grain interior atom, the GTA begins searching for and identifying individual grains. To begin, a randomly selected grain interior atom is picked and added to the current grain of interest as the first atom. This atom will temporarily be labeled as the *reference atom*. The nearest neighbors are then reviewed one by one and must meet certain criteria before being added to the grain currently being indexed.

The GTA first checks to make sure that the atom is also a grain interior atom. It is common for grains to be artificially connected by one or two atoms that are in a crystalline environment. Therefore, the segregation of grain edge atoms from the grain interior atoms which are deeper within the crystallite ensures more accurate grain identification by closing some of these artificial connections. Next, the orientation of our reference atom is compared with the orientations of its nearest neighbors, using a user defined *orientation-cutoff angle* as our metric. In its current

formulation, the GTA calculates the angles separating the <100> directions associated with the reference atom and the <100> directions associated with the nearest neighbor in question. If all of these angles are less than the orientation-cutoff angle, the nearest neighbor atom is added to the grain. We currently use an orientation-cutoff of only a few degrees, which will be discussed more extensively in the Applications and Examples section of the text. The chosen orientation-cutoff angle can be adjusted for a variety of reasons, with an obvious example being the decision whether to identify low-angle grain boundaries or not. A low-angle grain boundary composed of an array of dislocations would not appear as a continuous plane of non-crystalline atoms and would therefore not be identified as a grain boundary if only CSP or CNA is used. However, the GTA recognizes the change in crystal orientation across such a boundary if the orientation-cutoff is low and allows the two grains to be distinguished from one another. Since the GTA stores all orientation information needed to completely describe each atom's local crystallographic environment, one could also choose to calculate alternative metrics, such as misorientation angle, to compare with the orientation-cutoff angle.

After examining the nearest neighbors of the first reference atom, the GTA then selects one of the atoms which was just added to the grain as the new reference atom and repeats the procedure for this atom's nearest neighbors. By repeating this process, the algorithm builds the current grain outward, identifying suitable atoms along the way, until it has found all of the atoms associated with the current grain. The GTA then calculates the center of mass and the average crystallographic orientation of the current grain, saving this data with the grain number. With the first grain complete, the GTA then selects another random grain interior atom, making sure that it has not already been checked and added to a grain, as the first reference atom for the second grain. After all grains are identified, a nearest neighbor search of the grain edge atoms is used to find

which grain these atoms should be added to. This final step is important if one is interested in metrics such as grain size. While the grain edge atoms can be problematic for calculating orientation information, they are still crystalline and can be a significant fraction of the grain volume for very fine grained samples.

2.2.4 Grain Tracking

The GTA algorithm can analyze multiple output files from atomistic simulations and thus provide data regarding microstructural evolution through time. After all grains have been identified in each output file, the GTA then begins to identify and reassign each grain number such that it corresponds with its counterpart in the following time step. In order to accomplish this mapping, the center of mass of each grain in the initial reference configuration is compared to the next time step and the closest center of mass in the new file is found. Once these two grains are matched, the grain number of the new file is updated to match the grain number from the reference configuration. This process is then repeated for the remaining grains, until all grains are matched. While such a tracking mechanism can fail if a grain has moved too far away between successive output files, this problem can often be solved by simply analyzing the microstructure and tracking the grains more frequently during the simulation.

2.2.5 Visualization Techniques

In order to help facilitate the integration of the GTA into the combined computational-experimental framework needed for ICME, several common visualization techniques are employed by the algorithm. First, pole figures are developed by stereographically projecting a family of crystal axes for each grain with respect to a specified viewing direction. In the examples shown in this chapter, we project the <100> poles. In order to simplify interpretation of the data,

inverse pole figures can also be generated. Because of crystallographic symmetry for the fcc materials we focus on here, visualization of the inverse pole figure can be abbreviated into a single stereographic triangle. To produce these figures, the GTA automatically imposes all crystallographic symmetry operations for each grain and projects all associated poles stereographically. Those points which lie within the stereographic triangle are then plotted and graphically represent the orientation for each grain. Both of these methods are used extensively in the experimental community for visualizing texture. Finally, 3D orientation maps are also created by plotting all atom positions and color coding each grain according to its projected inverse pole. Such a visualization technique replicates traditional output of orientation imaging microscopy (OIM) software. All of these capabilities provide a direct link for simplifying the comparison of experimental texture data with those results produced by atomistic modeling.

2.3 Applications and Examples

To illustrate the utility of the GTA as well as highlight user-controlled features and practical concerns for the algorithm, several common examples of atomistic samples were analyzed. MD simulations were carried out with the open-source LAMMPS code [49] using an integration time step of 2 fs, and embedded atom method (EAM) potentials for Ni and Al developed by Mishin et al. [51] were used. CSP is used to identify non-crystalline atoms, with CSP $\geq$ 2.14 $Å^2$ and CSP $\geq$ 2.83 $Å^2$ characterizing defects in Ni and Al, respectively. Additional simulation details will be given when necessary. All atomistic visualization in this manuscript was performed with the open-source visualization tool OVITO [52].

2.3.1 Effect of Temperature on a Ni Σ5 (310) Symmetric Tilt Grain Boundary

We begin our analysis of atomistic examples by investigating a very simple, known sample microstructure: the Σ5 (310) grain boundary in Ni. The bicrystal sample shown in Figure 2-3 was created by tilting the crystals around the [100] crystallographic axis until there is a misorientation of 36.87° between the top and bottom half. Figure 2-3(a) shows this misorientation by drawing the <100> directions from each grain. Periodic boundary conditions were applied in the X- and Y-directions, while free boundary conditions were implemented in Z. Bicrystal samples such as these have been used extensively to investigate behavior such as dislocation emission from grain boundaries [53] or grain boundary migration [54]. These samples were equilibrated at zero pressure and temperatures of 10 K, 300 K, and 600 K for 20 ps.

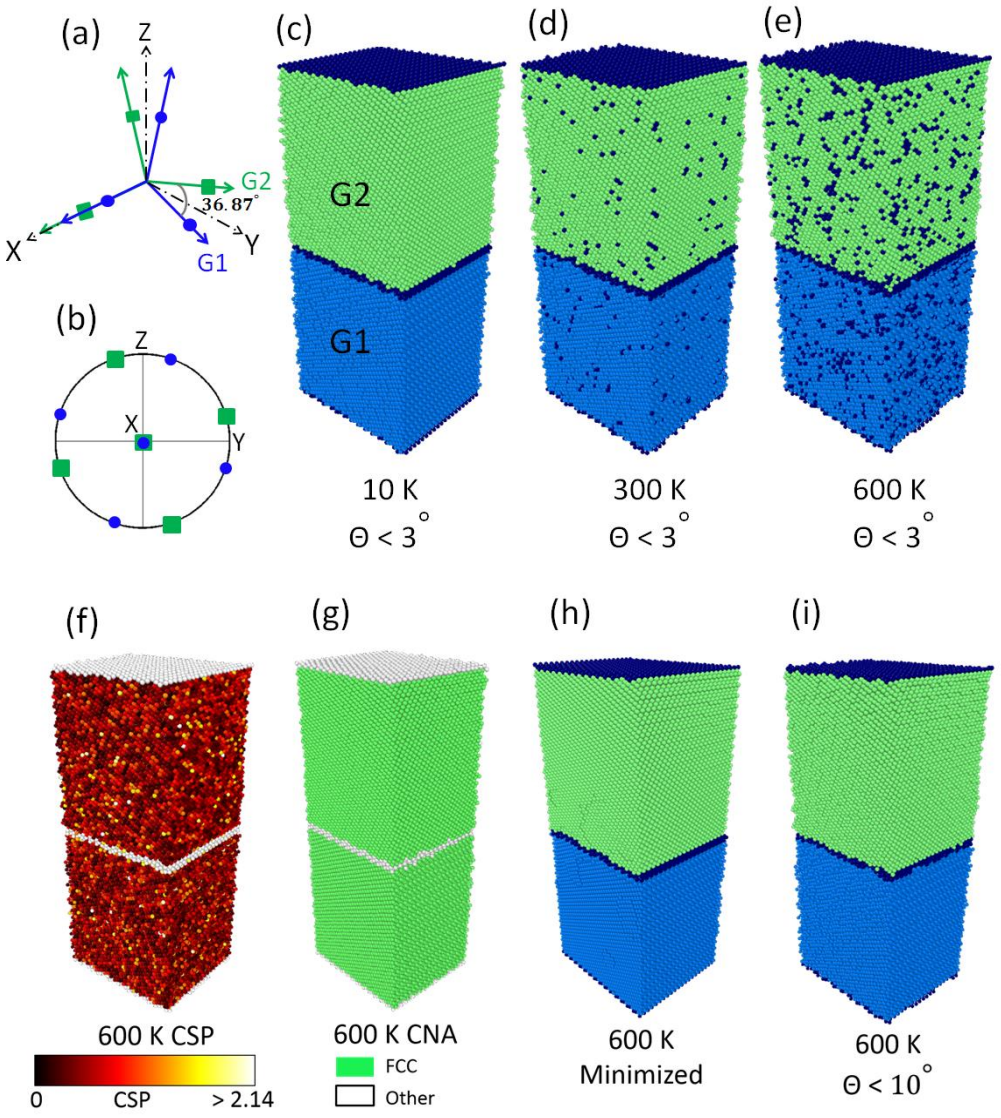

Figure 2-3 (a) and (b) show the <100> axes of the two grains from a Ni bicrystal in a vector schematic and a pole figure, respectively. (c)-(e) Samples colored according to grain number, using an orientation-cutoff angle (θ) of 3°, with light blue for G1 and green for G2, show increasing numbers of dark blue, unindexed atoms as temperature is increased. (f) and (g) show that CSP and CNA are not always good indicators of those atoms which will have large variations in local orientation. A conjugate gradient minimization (h) or an increase in the orientation-cutoff angle (i) will reduce the number of unindexed atoms.

Each sample was analyzed with the GTA using an orientation-cutoff of 3°, with results shown in Figure 2-3(c)-(e). In these images, atoms are colored according to grain number, with light blue signifying the first grain (G1) and green showing the second grain (G2). Atoms which

are not part of either grain are shown in dark blue. It is instructive to first focus on the sample at 10 K shown in Figure 2-3(c), where thermal vibrations are very small. In this case, dark blue atoms only appear at the bicrystal interface and at the free surfaces, meaning all atoms inside of the grains have been properly indexed. Figure 2-3(b) shows a {100} pole figure centered on the tilt axis of the bicrystal, or the X-axis of the simulation coordinates. While one <100> direction of each crystal is centered on the pole figure, the other <100> directions show the expected tilt rotation. As temperature is increased in Figure 2-3(d) and (e), a significant number of atoms cannot be indexed to either grain. It is important to note though, that the average orientation we measure is unchanged by this noise.

At first glance, one might think that this behavior is simply the result of CSP artificially identifying atoms as being in a defective local environment. However, Figure 2-3(f) shows atoms in the sample at 600 K colored according to CSP. Only a select few atoms within the grains are incorrectly identified as defects (white in this image), so this cannot explain the large number of dark blue atoms in Figure 2-3(e). Closer analysis shows that these atoms are not assigned to a grain because their local crystallographic orientation is different than their neighbors' due to thermal vibrations. To highlight that the GTA is not sensitive to the choice of CSP or CNA, Figure 2-3(g) shows the atoms colored according to CNA. While CNA has less trouble finding non-crystalline atoms at elevated temperature, we obtain the exact same result shown in Figure 2-3(e) when we repeat the GTA analysis, again because of local orientation fluctuations due to temperature.

Whether or not this issue needs to be addressed will depend on the information that is of interest for the particular application. For example, if finding the average orientation of each grain is the main goal, then the false negatives inside the grain can be ignored and a restrictive

orientation-cutoff angle can still be used. However, if it is necessary to accurately track grain size over time, all of the atoms inside the grain must be counted. One potential solution would be to run a subtle energy minimization procedure on the computational sample before analyzing with the GTA. Such a minimization will remove the noise from thermal vibrations, but care must be taken to ensure that it is not aggressive enough to significantly change larger features of the microstructure being analyzed. For all studies in this manuscript, we deemed a minimization to be appropriate if no significant orientation changes to the grains occurred. Justification of our energy minimization tolerance is further discussed in the next section. Figure 2-3(h) shows the 600 K sample which was minimized with the conjugate gradient method in LAMMPS (using a unitless energy tolerance of 10^{-6} and a force tolerance of 10^{-6} eV/Å) and then analyzed, showing that all atoms in the grains are identified. Alternatively, a user can increase the orientation-cutoff angle to a larger value. Figure 2-3(i) shows the 600 K sample analyzed again, but with an orientation-cutoff angle of 10°. In this case, all of the noise in local orientation induced by thermal vibrations is less than the cutoff value and all of the atoms are correctly identified. It is worth noting that increasing the orientation-cutoff angle could artificially lead to the merging of two grains into one, a possibility that will be discussed further in the next section.

2.3.2 Texture Analysis of Nanocrystalline Al Samples

We envision that a major application of the GTA will be the analysis of texture in atomistic simulations. For example, texture could be tracked during simulations of film deposition or deformation in nanostructured materials. To show the power of the GTA for such analysis, we next analyze two common types of nanocrystalline samples which are commonly found in the literature. Nanocrystalline materials are promising structural materials due to their extremely high strength [1] and atomistic simulations are often used to study their deformation physics in either

columnar grained [55, 56] or random polycrystalline samples [57, 58]. Columnar grained structures allow for easy viewing of dislocation-boundary interactions, while random polycrystalline samples are more realistic microstructures. A columnar grained sample was generated by creating 36 random grain centers on a hexagonal lattice, and then building crystallites with a common <100> axis and a random rotation angle around this axis for each grain. A random polycrystalline sample with 46 grains was created using a Voronoi tessellation construction modified to enforce a minimum separation distance between grain nucleation sites [59] and Euler angles that were randomly selected for each grain. Since simply filling space with atoms until grains impinge gives an artificial microstructure, conjugate gradient minimizations in LAMMPS (energy and force tolerances of 10^{-6}) were applied to both samples to create fully dense simulation samples by letting the atoms relax slightly. Both samples have an average grain size of 5 nm and contain Al atoms, and periodic boundary conditions are applied in all directions.

We begin our discussion of these samples by using the GTA, with an orientation-cutoff angle of 1°, to analyze the columnar grained sample in more detail. Figure 2-4(a) and (b) show the columnar grained sample in both its as-assembled state and after minimization, with atoms colored according to their grain number. It is clear that the as-assembled sample is not fully dense, as many grain boundaries contain small nanoscale voids, but minimization closes this porosity. A few grains coalesce, most notably the two at the top left and the three near the top right of the sample. These grains actually had very similar rotations around the <110> axis and were only artificially separated by porosity in the as-assembled sample. After minimization, the artificial boundary is removed and the crystallographic orientations are close enough that they are considered one grain.

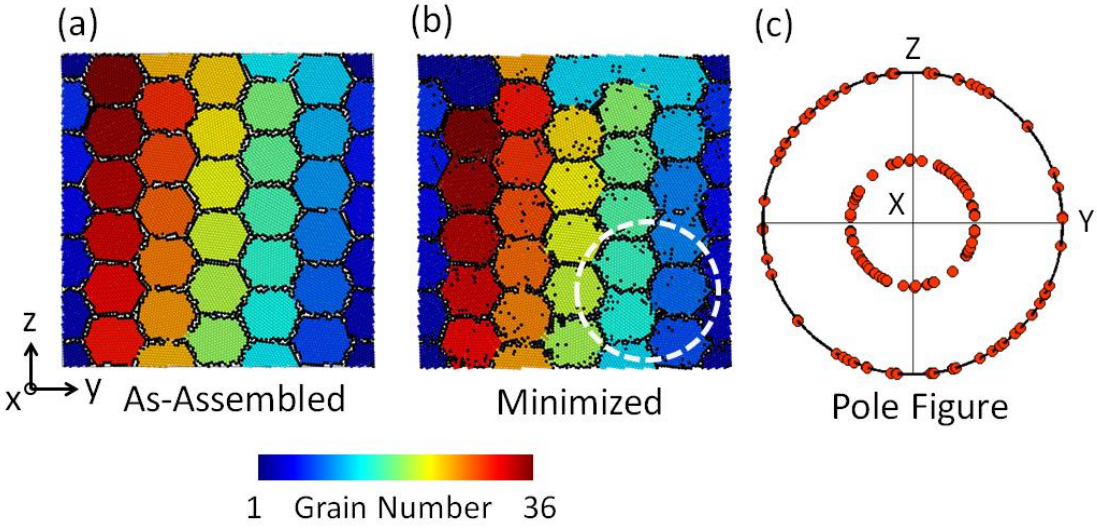

Figure 2-4 A columnar grained Al sample consisting of 36 grains, all with their {110} crystal planes oriented in the X direction. Atoms are labeled by grain number for (a) the as-assembled sample and (b) after energy minimization. (c) A {100} pole figure along the X-axis of the simulation cell reveals the sample texture.

Many unique grains are still identified after minimization, and their orientations are used to create the {100} pole figure shown in Figure 2-4(c). The inner circle on the pole figure is from the (100) and (010) planes of each grain, which are 45° away from the X-axis, while the outer circle comes from the (001) plawhich are perpendicular to the X-axis. This same data is also presented in inverse pole figures for each of the simulation axes in Figure 2-5. It is clear that only {110} planes are pointing in the X-direction, and the zoomed image of the bottom right corner shows that minimization only leads to a very small deviation from the as-assembled condition where grains are exactly columnar. A maximum out-of-plane rotation of 0.1° is observed for the minimized sample, and most grains are altered much less than this. Figure 2-5(b) and (c) show the inverse pole figures for the Y and Z simulation axes, and the orientations are restricted to the top borders of the stereographic triangle due to the columnar nature of the grains. These plots

confirm that we can recreate the type of orientation datasets that a researcher would take away from experimental investigations.

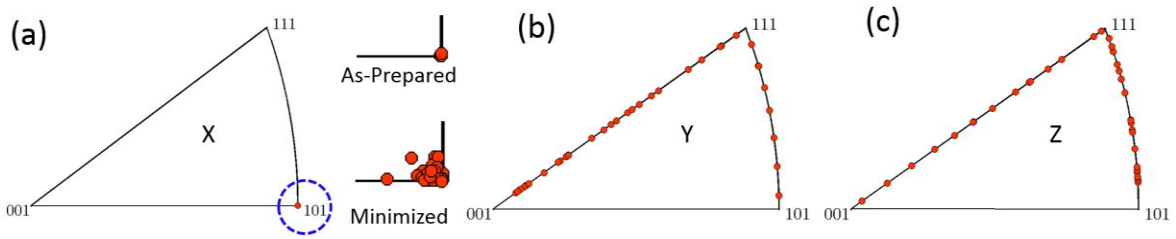

Figure 2-5 Inverse pole figures taken from the columnar grained Al sample, with each point on the triangle corresponding to a different grain. Along the X-axis of the sample, all grains have a {100} texture, while the other directions show a distribution of orientations. Energy minimization changes the out-of-plane orientation by a maximum of 0.1° and much less for most grains.

To show the effects of different choices for the orientation-cutoff angle more clearly, we focus on the collection of three grains marked with a dashed circle in Figure 2-4(b). These grains are shown in Figure 2-6 for orientation-cutoff angles of 1°, 1.5°, and 2°, with atoms colored according to their grain number. With the original choice of a 1° cutoff angle, three distinct grains are found, even though the red and orange grains do not have a discrete plane of non-crystalline atoms between them. As the cutoff angle for analysis is increased to 2°, these two grains are now identified as one by the new measurement standard. We make no judgment about which is correct, since the decision to exclude low angle boundaries may be application dependent.

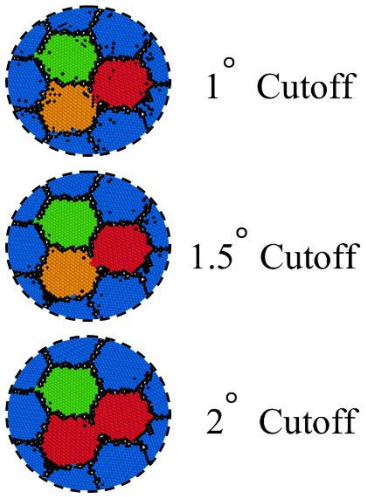

Figure 2-6 A collection of three grains within the columnar grained sample. As orientation-cutoff angle is increased, the number of unindexed atoms (black atoms) is reduced significantly. However, increasing the orientation-cutoff can also lead to two grains being identified as one, as shown in the case of a 2° cutoff angle.

We next move our attention to GTA analysis of the random polycrystalline sample in Figure 2-7. With no restrictions on the Euler angles that defined the orientation of each grain, we expect to have a random texture. Figure 2-7(a) shows the random polycrystalline sample with the atoms colored according to grain number while Figure 2-7(b) and (c) present a {100} pole figure and an inverse pole figure down the X-axis, respectively. Neither Figure 2-7(b) nor (c) shows any discernible pattern, confirming the sample's random texture. As a final comparison between columnar grained and random polycrystalline atomistic samples, Figure 2-8 shows orientation maps for the X-axis of the simulation cells. While the columnar grained sample (Figure 2-8(a)) is entirely green and has only {110} planes pointing in the X-direction, the random polycrystalline sample (Figure 2-8(b)) shows a mixture of colors and orientations. Note that the black region on the front face of the random polycrystalline sample is simply a region where a grain boundary is located at the cell boundary. It is clear that the GTA can provide quantitative measurements of sample texture, while also presenting the data in a way that is intuitive.

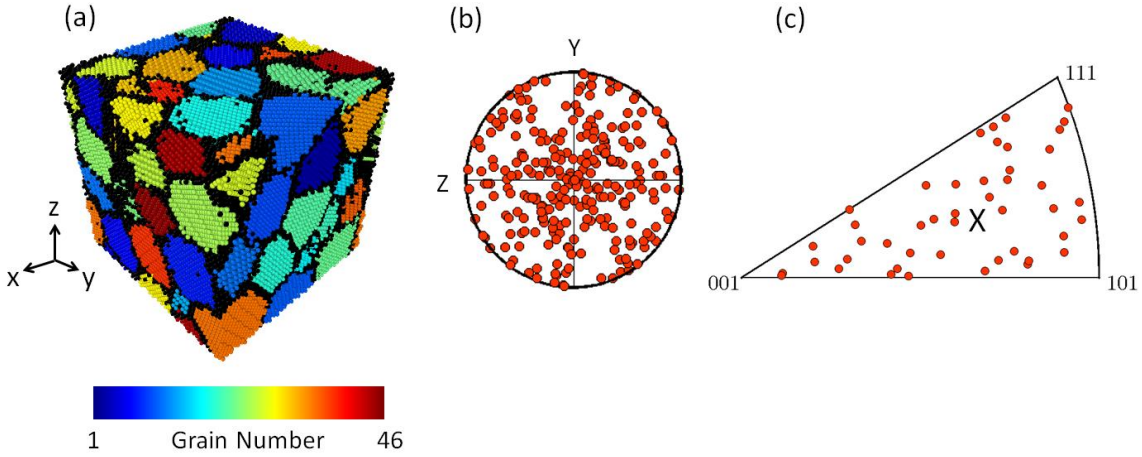

Figure 2-7 (a) A polycrystalline Al sample, with 46 randomly oriented grains. Atoms are colored according to their grain number. The random orientation is expressed in both (b) a {100} pole figure and (c) an inverse pole figure along the X-axis of the sample coordinates.

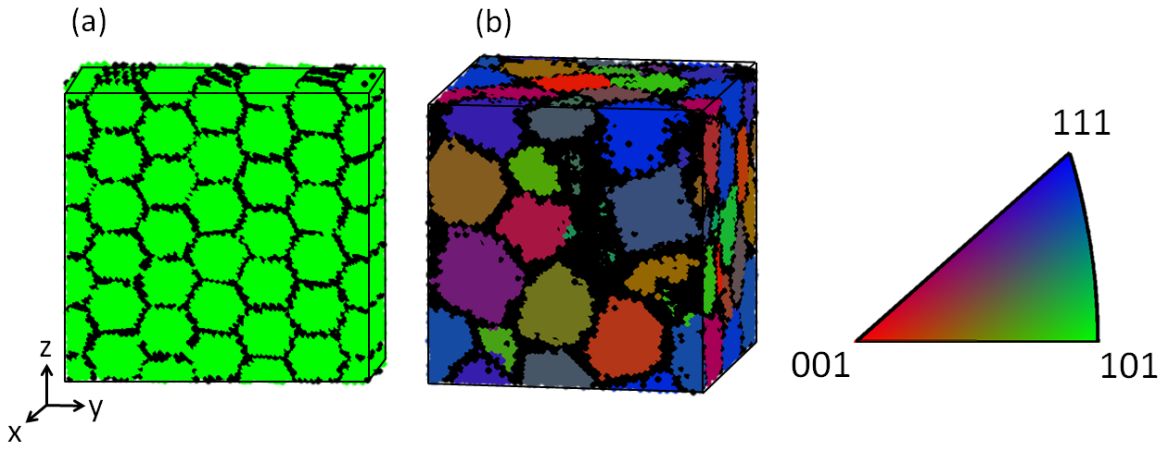

Figure 2-8 (a) Orientation map from the X-axis of the columnar sample, showing the expected {110} texture. (b) Orientation map from the X-axis of the random polycrystalline sample, showing the expected random texture.

2.3.3 Strained Polycrystalline Sample

The real value of the GTA arises when the starting microstructure is unknown or when structural changes must be tracked over time. We finish our analysis of example problems by investigating grain rotation during the deformation of nanocrystalline Al at different testing

temperatures. The random polycrystalline sample introduced above was first equilibrated at 600 K and zero pressure for 100 ps using a Nose-Hoover thermo/barostat. One sample was deformed at 600 K, while two others were cooled to 450 K and 300 K and then deformed. A constant cooling rate of 30 K/ps was used to lower the temperature of the system. Deformation was simulated by applying a uniaxial tensile strain (ε) along the Z-axis at a constant true strain rate of 5×10^8 s^{-1} while keeping zero stress on the other axes using an NPT ensemble.

Figure 2-9(a) presents the true stress-strain curves from the nanocrystalline Al samples tested at different temperatures. As temperature is increased, both yield strength and flow stress decrease. Such behavior has been reported previously (see, e.g., [25, 60]), but here we can quantify the temperature dependence of an important deformation mechanism: grain rotation. While a handful of previous reports have tracked the rotation of a few select grains during MD deformation of nanocrystalline metals, these always represented a fraction of the total grains in the sample [25, 61, 62]. Here, we track all grains in the sample and track changes to their orientation as a function of strain for different temperatures. We examine this structural evolution in 2% strain intervals up to 10% applied true strain. For the limited number of grains that rotate and coalesce to form larger grains or shrink and disappear, we track orientation for as long as possible. Figure 2-9(b) presents the average rotation of grains towards the tensile axis to provide a measurement of rotation as a function of strain. Perhaps not surprisingly because of the increase diffusion at higher temperatures, there is significantly more grain rotation on average for the sample tested at 600 K than for the sample tested at 300 K. At 10% applied strain, grains in the 600 K sample have rotated ~50% more than grains in the 300 K sample.

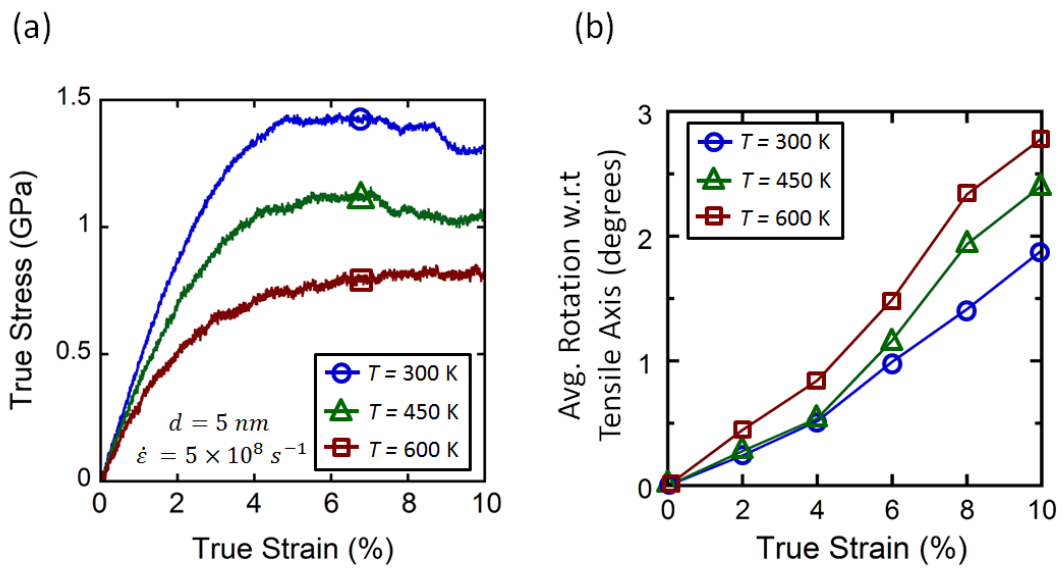

Figure 2-9 (a) Tensile stress-strain curves for nanocrystalline Al samples with a mean grain size of 5 nm, tested at different temperatures. (b) Average grain rotation from starting configuration, measured as the angle with respect to the tensile axis. Increasing temperature from 300 K to 600 K leads to a ~50% increase in average grain rotation.

Because we track individual orientations as well, we can focus on interesting grains. Figure 2-10 presents inverse pole figures from the tensile axis for the three testing temperatures, with orientations shown at different strains. We only plot five grains here to simplify visualization. Some grains experience a slow but steady rotation, while others experience large changes in orientation within one 2% strain interval. In general, while the grains rotate more at elevated temperatures, each grain rotates in roughly the same direction at every temperature. For example, G5 moves up and to the left in all frames of Figure 2-10. This suggests that the rotation direction is likely limited by the compatibility with surrounding grains and only the magnitude of rotation is strongly affected by temperature. In addition to a quantitative understanding of textural changes, the algorithm also keeps track of grain shape and center of mass. As such, individual grain tracking can be carried out in a much simpler fashion. Traditionally, in order to document the merging of two adjacent grains one might search manually through the atomistic sample for such a case and

then track the movement and rotation using visual alignment of atomic planes. Since grain sizes and orientations are calculated automatically with the GTA, it is easy to identify which grains will merge and visualization of these deformation mechanisms can be conducted quickly. To illustrate, Figure 2-11 shows magnified images of the tracking of 3 grains. The red grain slides into the page during the tensile test (disappearing from view), while the gold and blue grains rotate toward each other and coalesce when 6% true strain is applied.

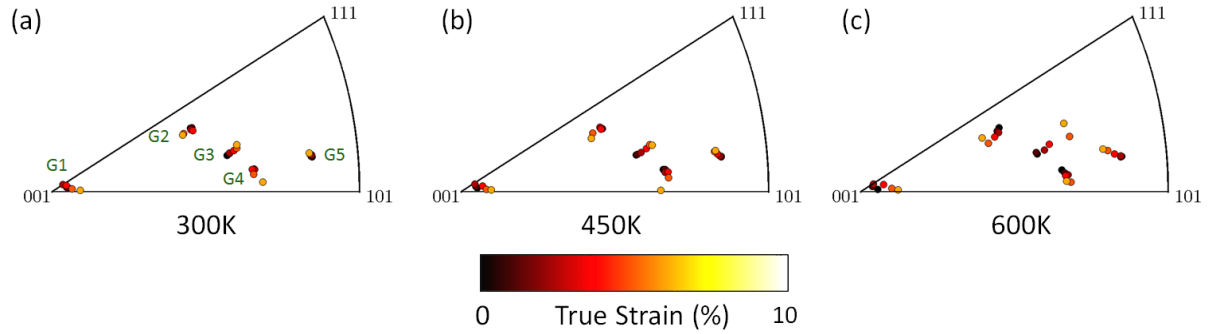

Figure 2-10 Inverse pole figures for a nanocrystalline Al sample deformed at three different temperatures, showing 5 different grains and tracking their orientation evolution as a function of time. While the direction of rotation stays the same, the amount of rotation increases with increasing temperature.

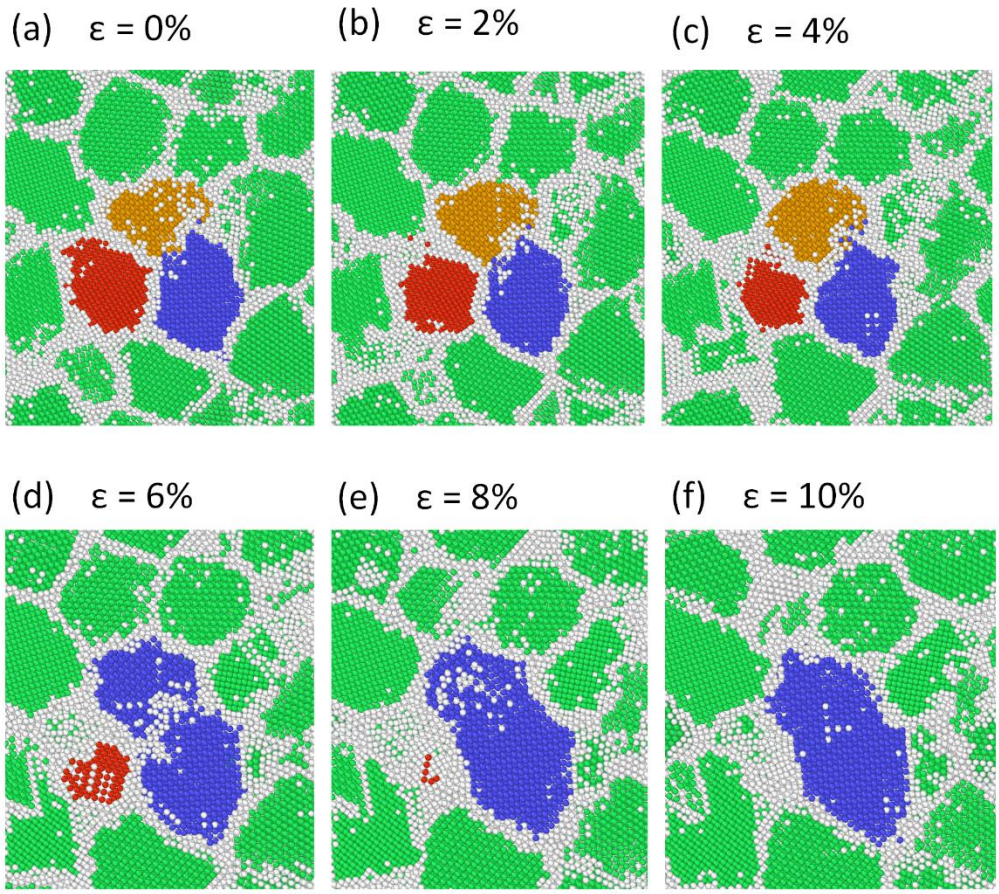

Figure 2-11 Tracking of grain coalescence during tensile loading of nanocrystalline Al. Three grains are identified in (a). As strain is applied, the gold and blue grains rotate toward each other and merge, while the red grain slides into the page.

2.4 Conclusions

Atomistic modeling tools can potentially provide the enormous datasets of 3-D microstructural features that are essential for ICME efforts, but only if characterization of these simulations evolves from anecdotal observations to quantitative metrics. In this chapter, we have introduced a new post-processing algorithm that can be used to identify and track microstructural changes in crystalline materials during computational studies on the atomic scale. The GTA enables the quantitative characterization of grain size, grain orientation, and sample texture while

also tracking these features as a function of time during simulations of dynamic behavior. This data is also presented in ways that are commonplace within the experimental community, such as pole figures, inverse pole figures, and orientation maps, in order to further connect computational and experimental research. In order to clearly illustrate the capabilities of the GTA, a number of common MD simulation cells were also analyzed. These examples show that:

- Atomistic orientation measurements on the atomic scale can be made by applying simple crystallographic analysis techniques to an atom's local environment. This local orientation can enable the identification of even notoriously difficult to extract low-angle grain boundaries. By taking average orientations from all atoms, the crystallographic texture of known test samples was confirmed, showing that the extremes of strong out-of-plane texture and completely random texture could be identified.
- The thermal vibrations in high temperature simulations may make it difficult to index certain crystalline atoms to the correct grain if a restrictive orientation-cutoff angle is used. While this does not affect the measured orientation in any meaningful way, it should be important for tracking grain size and can be addressed by a larger cutoff angle or energy minimization techniques. Care must be taken that any energy minimization damps out these vibrations but does not dramatically alter larger microstructural features.
- Grain rotation was measured in nanocrystalline Al as a function of applied strain for three different testing temperatures. Higher temperatures lead to more grain rotation during plastic deformation, with ~50% more grain rotation toward the tensile axis at 600 K than at 300 K.

As a whole, it is the author's hope that this modest contribution of the GTA analysis tool can have an impact by encouraging dialogue and data-sharing between the computational and experimental materials characterization communities. This analysis code will be provided to any interested researchers who would like to quantify microstructure in atomistic data files. It is our hope that any improvements will in turn be made available to the ICME community.

CHAPTER 3. Quantitative Tracking of Grain Structure Evolution in a Nanocrystalline Metal During Cyclic Loading[2]

3.1 Introduction

As previously mentioned in Chapter 1, the reduction in average grain size (d) to the nanometer range results in the suppression of traditional intragranular dislocation mechanisms [1, 63]. The higher stress levels which can be accessed and the increased grain boundary (GB) volume fraction in nanocrystalline materials exaggerates the importance of interfaces as plasticity mechanisms begin to depend heavily on the grain boundary network. As average grain size is reduced to the smallest possible nanocrystalline regime (d < 15-20 nm), plasticity becomes dominated by phenomena such as GB sliding [13, 25, 28, 64], grain rotation [18, 19, 65], and GB migration [22, 23, 66]. A common feature of these new mechanisms is that they all represent collective motion of groups of atoms and should alter the internal grain structure of the material. For example, rotation of two neighboring grains would alter the misorientation between the grains and the character of the GB which separates them.

Prior investigations of nanocrystalline plasticity have shown that strain accommodation mechanisms can occur cooperatively throughout the microstructure, leading to evolution of the interfacial network through large scale sliding and rotation processes. For example, Hasnaoui et al. [67] used molecular dynamics simulations to observe the emergence of shear planes in

[2] The contents of this chapter have been previously published as Panzarino JF, Ramos JJ, Rupert TJ. Modell. Simul. Mater. Sci. Eng. 23(2): 025005.

nanocrystalline Ni through the alignment of grain boundary planes via grain rotation, GB sliding, and GB migration, which then resulted in localized shear deformation as well as grain coalescence and growth. These observations were supported by the model of Hahn and Padmanabhan [68], which explains that substantial sliding on the mesoscale can only be accomplished by long range interconnection of interfaces. A recent MD study by Rupert [69] also showed that strain localization in nanocrystalline metals is highly dependent on the connectivity of the interfacial network. For the finest nanocrystalline grain sizes, the high strain path was formed through only grain rotation and GB sliding, with no significant evidence of dislocation motion. Once neighboring grains align to form a percolating GB network, catastrophic shear deformation occurs suddenly. In contrast to coarse grained metals whose plastic deformation is governed by intragranular interactions between dislocations, nanocrystalline metals have exhibited structural evolution such as mechanically-induced grain growth [70] during loading.

The importance of grain structure evolution should be exaggerated during low cycle fatigue loading, where multiple cycles of plastic strain are applied. It has been suggested that cyclic softening or strengthening processes during fatigue are highly dependent on the initial microstructure of the nanocrystalline metal [6]. Nanocrystalline Ni with minimal initial defect densities exhibited cyclic hardening during fatigue tests [71, 72]. Moser and colleagues were also able to identify a shift in plasticity from dislocation based to GB mediated during the initial fatigue cycles of nanocrystalline Ni [72]. Rupert and Schuh [59] observed a strengthening effect during MD simulations of cyclic loading in nanocrystalline Ni, which they ascribed to boundary relaxation and the formation of low energy boundaries. Grain growth has also been found to occur during mechanical cycling, as shown by tensile load-unload fatigue tests of nanocrystalline Cu by Witney et al. [73]. Schiotz also observed grain coarsening using molecular dynamics of Cu

subjected to large tension-compression strain cycles [74]. While these studies show that nanocrystalline grain structures are dynamic, most characterization has been relatively qualitative and an opportunity exists for the quantification of grain structure evolution.

With previous work providing evidence that collective GB processes are taking place, quantification of structural evolution during plasticity is the next logical step in furthering our understanding of nanocrystalline deformation physics. In this chapter, we use MD to simulate the cyclic deformation of nanocrystalline aluminum, with an emphasis on understanding how grain structure evolves during loading. During cycling at three different temperatures, we quantify the amounts of grain rotation, grain growth, and grain sliding using the Grain Tracking Algorithm. These mechanisms are found to be very temperature-dependent, with higher testing temperatures leading to more collective reorganization of the grain structure. Significant structural changes are observed, with the most notable being the formation of many twin boundaries in the material.

3.2 Computational Methods

Computational nanocrystalline Al samples were made using the Voronoi tessellation construction, a well-established method for simulating nanocrystalline specimens and studying their properties [75-78]. Euler angles were randomly generated for each grain nucleation site in order to obtain a random texture distribution throughout the sample and any overlapping atoms were removed once grains were grown. MD simulations were performed with the open-source Large-scale Atomic/Molecular Massively Parallel Simulator (LAMMPS) [49] code with an integration time step of 2 fs and an embedded atom method (EAM) potential for Al developed by Mishin et al. [51]. MD time steps must be lower than the shortest vibrational period of the atoms in the solid (typically ~1 ps) [79] and commonly used time steps vary from 1-5 fs. The

validity of a 2 fs time step was verified by comparing with an identical mechanical cycling simulation at 300 K using a smaller time step of 1 fs. The cyclic stress-strain curves were virtually identical, but the longer time step allowed for faster simulation. The Al structure was first relaxed using a conjugate gradient minimization in LAMMPS with an energy tolerance of 10^{-6} eV and force tolerance of 10^{-6} eV/Å. This approach resulted in a fully dense nanocrystalline Al sample with d = 5 nm and starting grains free of stored dislocations. Nanocrystalline thin films have similarly been shown to be dislocation-free in their as-deposited condition [80]. The initial configuration contained 44 grains and periodic boundary conditions were imposed in all directions to simulate a repeating volume element of nanocrystalline Al. Previous work has shown that local GB structure can be in a non-equilibrium state, one which contains excess boundary dislocations or free volume [81]. This non-equilibrium structure can be "relaxed" during annealing or deformation [59, 82], and the boundary can reach a lower energy state. While non-equilibrium boundary structures are present in as-prepared nanocrystalline MD samples, we want to focus on more obvious changes to the grain structure here. Therefore, we anneal our samples at 600 K before testing in order to remove those non-equilibrium boundaries that may be a byproduct of our sample construction technique. The samples were equilibrated at 600 K for 100 ps to relax GB structure, and then cooled at a rate of 30 K/ps until the desired testing temperature was reached. Cyclic loading simulations were run at 600 K, 450 K, and 300 K, to investigate the effect of temperature on deformation physics and structural evolution.

Monotonic tension and tensile load-unload cyclic loading was applied along the Z-axis of the samples. A constant true strain rate of 5×10^{8} s^{-1} was used and an isothermal-isobaric (NPT) ensemble was employed to keep zero stress in the lateral sample directions. Monotonic loading was conducted by straining the nanocrystalline Al to 10% true strain. Low cycle fatigue was

simulated by first loading to 5% strain to induce plasticity, and then unloading and reloading in 2% strain increments. The cycling began after the yield point of the sample, so that microstructural changes due to plastic strain accommodation could be observed. In other words, the sample was unloaded to 3% and then reloaded to 5% to complete one fatigue cycle. Up to 10 cycles were performed, with full loading to 10% true strain after 5 and 10 cycles to investigate the effects of cycling on subsequent mechanical behavior. Atomic positions were analyzed to measure important structural features after the initial 5% strain (cycle 0) as well as at the conclusion of each unloading-loading cycle (also 5% strain). This provided several data sets for each temperature from which evolution trends could be extracted.

The strain rate of 5×10^8 s^{-1} was chosen to balance simulation time with sample size, with this value lying within the range of strain rates reported to be acceptable in the MD literature. Previous computational work [25, 36, 83] and experimental work [84-86] has reported that the mechanical response of nanocrystalline metals can be very rate sensitive, so care must be taken not to directly compare property values measured from MD with values from experiments. However, MD simulations with strain rates similar to ours have been shown to capture the important physical processes which govern nanocrystalline plasticity. Schiotz et al. [25] uncovered correlated grain boundary events which produce GB sliding by running MD simulations at a strain rate of 5×10^8 s^{-1}. In addition, Schiotz et al. probed the effect of MD strain rates explicitly and found that pronounced rate sensitivity is only observed for strain rates above 1×10^9 s^{-1}. To explain such observations, Brandl et al. [83] were able to identify a delay in the onset of dislocation propagation as well as reduced levels of cross slip in nanocrystalline Al when strain rates were above 1×10^9 s^{-1}. These authors also observed a noticeable stress overshoot during the early stages of plasticity when such mechanisms were suppressed. Their work revealed that the

movement and lifetime of dislocations was highly dependent on the strain rate used to simulate deformation. Since our initial Al sample is dislocation free and we observe very minimal dislocation activity during and after cycling, the propagation or cross slip of pre-existing dislocations is not a key issue. Our simulations mainly report the occurrence of grain boundary accommodated mechanisms (which are expected at such a small average grain size [87]). Moreover, we do not observe a stress overshoot during loading.

A recently developed post-processing algorithm called the Grain Tracking Algorithm (GTA) was used to convert the positions of the atoms in the simulation into structural measurements [88]. This algorithm identifies all crystallites in the system using atomic positions and centrosymmetry parameter (CSP) as required inputs. CSP quantifies the local distortion from a perfectly symmetric crystal lattice at a given atomic position [45] and was used here to distinguish crystalline atoms from those in the GBs. For Al, atoms exhibiting a CSP ≥ 2.83 Å^2 were designated non-crystalline, based on the Gilvarry relation [50] which places an upper limit on the thermal vibrations a crystal can experience without melting. CSP was deemed an appropriate metric for classifying crystallinity during analysis since it is commonly used to identify plastic defects in cubic materials [33]. However, CNA [46] was occasionally used to visualize the grain structure and identify features such as twin boundaries. All visualization of atomic data in this work is performed by the open source particle visualization tool OVITO [52].

Using the face centered cubic (FCC) unit cell as a reference configuration, the nearest neighbor atoms of each crystalline atom are used by the GTA to determine the local crystallographic orientation at each atomic position [88]. Neighboring crystalline atoms are added to grain lists as long as the misorientation measured between their locations is within a designated cut-off angle, θ. If the misorientation angle between crystalline points is above this threshold, the

atoms are deemed to belong to a different grain. To capture any low-angle GBs, a strict misorientation cut-off angle of $\theta < 3°$ was used. Once all atoms within a grain are identified, the overall orientation of the grain is found by averaging the calculated local orientations of all atomic points within the grain. This process is continuously repeated until all crystallites within the sample are identified. Figure 3-1(a) shows the starting microstructure of the 600 K Al sample with all grains identified by color according to the legend below the figure. The black atoms represent boundary or defect atoms which do not belong to any grain. Use of the GTA also allows us to visualize the grain structure in ways that are analogous to the outputs from common experimental characterization techniques. Figure 3-1(b) projects the {100} poles of each crystallite in the starting configuration onto a plane with a normal along the Z-axis, showing a random texture. Figure 3-1(c) is a three dimensional crystallographic orientation map of the same sample, with colors corresponding to inverse poles of the grains which are parallel to the Z-axis. Similar to orientation imaging microscopy, which is commonly used to portray data from electron backscattering diffraction (EBSD), the small triangular color-key below Figure 3-1(c) can be used to identify the orientation of each grain.

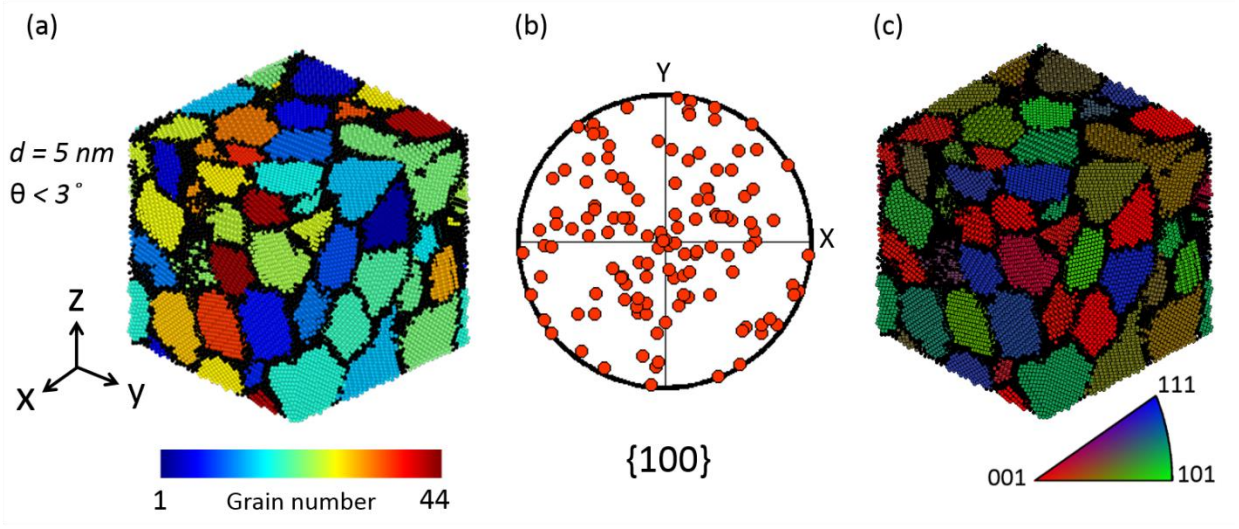

Figure 3-1 (a) Starting configuration of the polycrystalline Al sample with 44 grains, each identified by color. Automation of grain identification was done using the Grain Tracking Algorithm with a specified

misorientation cutoff of $\theta < 3^{\circ}$ between crystalline nearest neighbors. Black atoms are those which were identified as GB or "other" atoms. (b) Pole figure representation of overall random texture distribution of all grains. (c) {001} Orientation map showing distribution of all grain normals with respect to the simulation Z-direction.

With all crystallites and their attributes identified for every simulation time step, evolution of the grain structure was tracked through time. This was accomplished through a mapping of the grain numbers between simulation time steps. In order to map a grain to its past state in a preceding MD output, an atom which lies deep within the interior of the grain is found and its grain number is updated to that of an atom residing near the same coordinates in the preceding time step. All atoms within the grain of interest are then also updated to reflect the proper grain number. This process is repeated for all grains and carried through all MD outputs so that grains are properly tracked for the entirety of deformation.

3.3 Results and Discussion

3.3.1 Mechanical Behavior and Cycling Phenomenology

Overall mechanical behavior was first analyzed by investigating stress-strain curves for the three testing temperatures, as shown in Figure 3-2(a). Stress was calculated from the system pressure tensor output by LAMMPS, with the Z-component giving the reported uniaxial stresses during cycling. Compared with the monotonic loading behavior, cycled samples demonstrate higher ultimate (peak) strengths, as shown in Figure 3-2(b). The samples which were mechanically-cycled 10 times were all found to have ultimate strengths at least 10% higher than those of their monotonic counterparts. However, the strengthening from cycling is apparently temporary at the lowest temperature as can be noted by the decrease in flow stress, the stress required to continue plastically deforming the material, at the highest strains. The sample cycled

at 300 K exhibits the largest increase in ultimate strength (13.4%), but the flow stress decreases at the highest applied strains to values similar to those of the monotonically strained sample. A combination of elevated temperature and multiple loading cycles seems to ensure that strengthening is more permanent. The black arrows on the right side of Figure 3-2(a) help illustrate how the flow strength does not return to its initial values at temperatures of 450 K and 600 K.

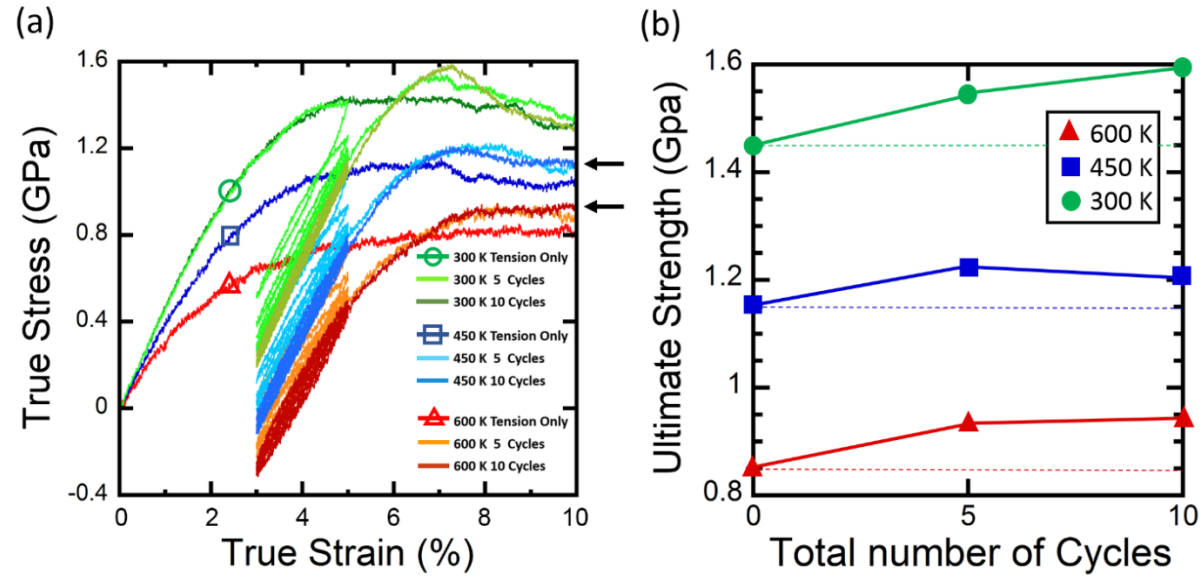

Figure 3-2 (a) Results of monotonic tension and tensile load-unload fatigue simulations. All tests were strain controlled with the same initial starting configuration. (b) Ultimate (peak) strength as a function of cycle number for all three fatigue conditions (0, 5, or 10 cycles). Dotted lines are drawn to help illustrate the level of strengthening observed.

Further inspection of the mechanical response indicates the presence of hysteresis during cyclic deformation. Because the evolution of hysteresis loops can be a signature of large-scale underlying plastic rearrangement, these loops were analyzed to measure any trends with cycle number. First, the area in each hysteresis loop was measured. Before areas of these loops were calculated, a least squares approximation was applied to the data in order to best fit the small fluctuations in the stress measurements. A Savitzky-Golay filter which fits a series of low-degree polynomials to adjacent data points was used and is a common smoothing technique for decreasing

data noise without significant signal distortion. A polynomial order of 3 was used with a frame size of 71, meaning that the data only needed very minimal smoothing [89]. Figure 3-3(a) is a plot of the 300 K stress-strain response with an overlay of the smoothing function for the first tensile load-unload fatigue cycle. The integrated hysteresis loop area is shown in red for a single cycle to clarify our definition. The hysteresis loop areas are plotted as a function of cycle in Figure 3-3(b). There seems to be no apparent trend and the areas are relatively constant as a function of cycle.

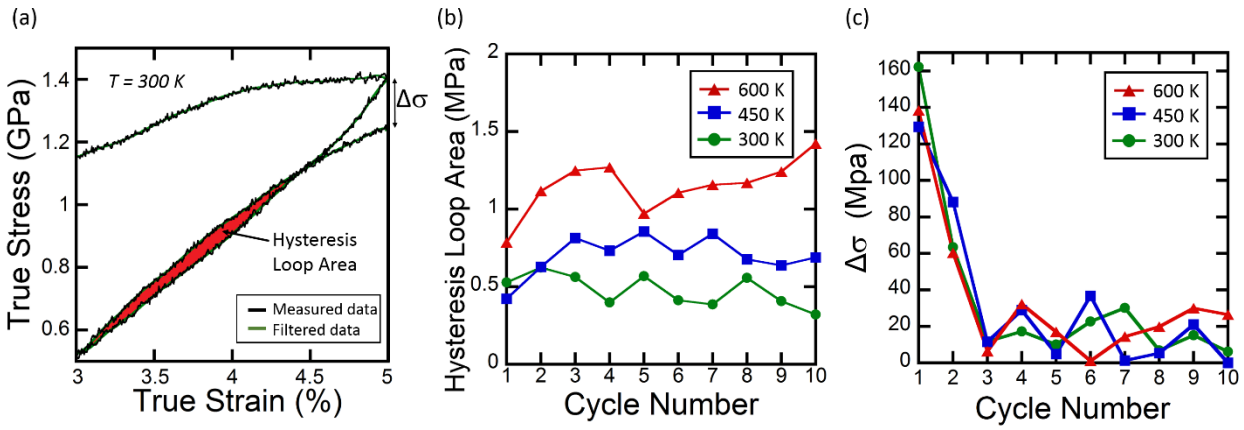

Figure 3-3 (a) A smoothed portion of the 300 K stress strain response illustrating a hysteresis loop area as well as the peak stress difference (Δσ) measurement for one complete loading cycle. (b) Enclosed hysteresis loop areas for all temperatures as a function of cycle number. (c) Peak stress difference (Δσ) measurements as a function of cycle number.

In a previous high cycle fatigue experiment by Moser et al. [72] regarding the hardening response of nanocrystalline Ni (d = 23 nm), the measured mid loop width strains were found to follow two different hardening regimes. The majority of the change they observed in the hysteresis loop size occurred during the first 10 cycles, when GB dislocation sources were active in their material. After exhaustion of these dislocation sources, the mode of deformation shifts to boundary mediated mechanisms and the rate of change of the hysteresis loops decreases significantly. In addition, Moser et al. also discovered that at higher cyclic frequencies the first (dislocation based) plasticity regime can be skipped altogether. Due to the extremely small grain size, lack of dislocations in our samples, and inherently high strain rates of MD simulations it

follows that the cyclic plastic deformation of our nanocrystalline Al is taking place in the latter regime, or by collective grain boundary mechanisms, an observation in line with Figure 3-3(b).

Although the area enclosed by the hysteresis loops does not change, the loops shift down to lower stress values as more cycles are applied. To quantify this change, we measure the change in maximum stress (stress measured at 5% strain) between consecutive cycles and have designated this measure the peak stress difference, $\Delta\sigma$. The reader is again referred to Figure 3-3(a) in order to clarify our measurement of $\Delta\sigma$. There is an apparent shift in the peak stress difference measured in the first 3 cycles for all temperatures, followed by fluctuation at small values at the higher cycle numbers. The concept that the largest change occurs during the early plastic cycles is consistent with the trends we observe in structural evolution later in this chapter. Nevertheless, microstructural rearrangement is taking place as to minimize the overall strain energy, thus reducing the maximum stress attained at 5% as the hysteresis loops shift downward and the metal exhibits hardening. Such cyclic strengthening was also reported by Moser et al. [72] during fatigue experiments of nanocrystalline nickel.

3.3.2 Evolution of the Overall Grain Structure

Having documented obvious changes in mechanical properties, we next investigate the origins of the recorded strengthening through examination of the underlying microstructural evolution. Figure 3-4(a) through (c) show inverse pole figures with grains labelled according to the number of fatigue cycles. These plots clearly show more grain rotation at the higher temperatures. Some grains were found to merge and/or disappear, leading to an inability to map these grains through the entirety of the simulation. This can be observed in the pole figures as disappearing points (poles that cease to exist).

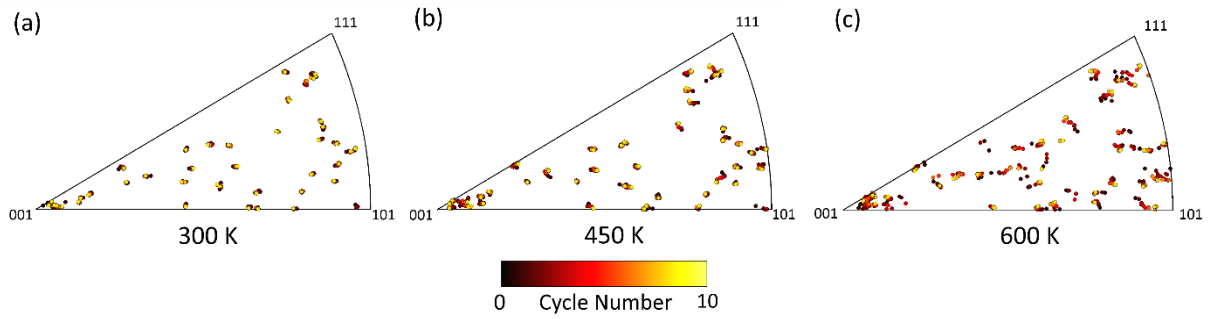

Figure 3-4 Z-Direction inverse pole stereographic projections show the evolution of the orientations of all grains at each temperature. Displacement of each point gives a visual representation of grain rotation caused by each cycle.

An increase in grain rotation at elevated temperatures is consistent with the theories for GB plasticity mechanisms that are available in the literature. As theorized by Ashby and Verrall [90], atomic rearrangement through GB sinks and sources allow GBs to act like viscous barriers to the sliding of neighboring crystalline interfaces. A model developed by Harris et al. [91] describes grain rotational rate as a function of net torque and GB diffusivity, implying that the magnitude of grain rotation will have an Arrhenius-type temperature dependence. Moldovan et al. [92] developed an extended model to include arbitrary grain shapes and ended up with an analytic expression involving grain size and temperature dependence that replicates the results of Harris et al. for the specific case of hexagonal grains. Although the driver for net torque acting on a grain can vary between models, all of these theories and others in the literature [93-95] agree that such rotation is assisted by atomic shuffling within the GBs, implying that increases in temperature should lead to more rotation.

This temperature dependence on grain rotation was analyzed in a quantitative manner using the grain structure information provided by the GTA. Figure 3-5(a) shows the average rotation for all grains as a function of cycle by comparing the measured orientation after each cycle with the original orientation at cycle 0. It is clear that the higher temperatures allowed for significant increase in average grain rotation. In fact, the average rotation after 10 cycles for the 600 K sample

was measured to be 3.7 times that which took place in the 300 K simulation. It is important to note that there were multiple grains which experienced much larger overall rotations than the average. Several grains rotated more than 5° at the highest temperature, especially those grains which shrank throughout the cyclic deformation process.

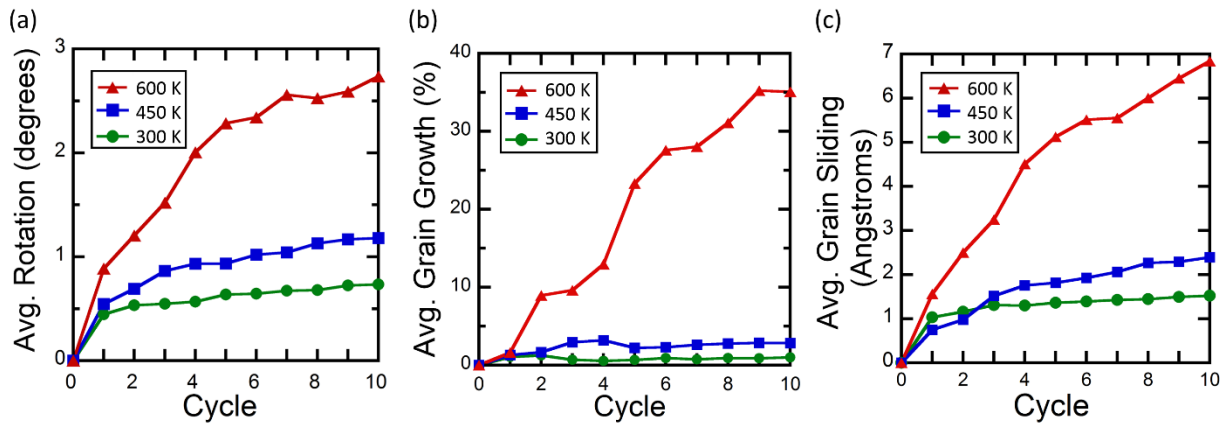

Figure 3-5 (a) Average rotation of all grains with respect to their original configuration at cycle 0. Rotation was measured by calculating the misorientation angle between the original orientation and the new orientation found after each load cycle. (b) Grain growth as a function of cycle for all three temperatures. Average grain size calculated after each cycle was compared to that which was found at cycle 0. (c) Average grain sliding as a function of cycle number. The displacement of the center of mass of each grain was found and compared with the original location at cycle 0.

The GTA data allowed us to measure and track the rotation axis of each grain between cycles as well. It was found that the rotation caused by additional cycles was not occurring about a consistent axis of rotation. As an example, Figure 3-6 shows the rotation axis as a function of cycle number through the use of an inverse pole figure. This figure tracks the evolution of the rotation axis for a single grain which shrank significantly throughout deformation at 600 K. This sporadic change in axis was found to be characteristic of all grains within the same sample, as well as those in the 450 K and 300 K samples. This observation shows that grains are not rotating in the same direction during each cycle. Rather, they are shifting in different directions through a "ratcheting" type of motion. The monotonically loaded sample was also analyzed in a similar fashion, by tracking rotation axis as a function of strain. Again, the rotation axis changed as a

function of strain. Schiotz et al. [25] previously postulated that large rotations about a single axis take place to accommodate and reduce stress, whereas smaller rotations about varying axes help to provide subtle boundary rearrangement. In our analysis, we find no evidence of a common rotation axis for cycled or monotonically loaded samples which suggests that the direction of rotation is determined by reduction in interfacial energy between grains, with applied strain the driver for this mechanism. As a point of caution, we note that the measurement of misorientation axis when rotations are small could be affected by thermal noise as well as an approaching mathematical singularity at the zero point associated with small relative misorientations [96].

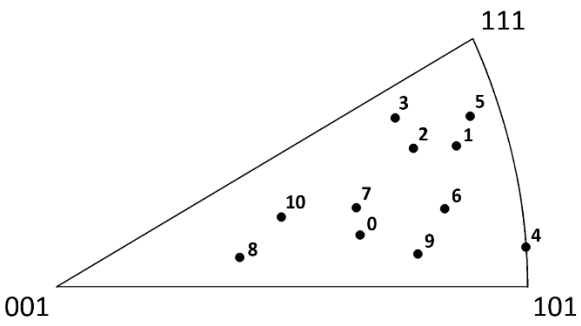

Figure 3-6 Stereographic triangle showing the random evolution of the misorientation axis for a single rotating grain as a function of cycle number.

The grains with largest measured rotations were the smallest grains in the sample and tended to shrink during the simulation, some of which completely disappeared before the 10th cycle. An example of this is shown in Figure 3-7(a), which isolates a collection of 5 grains at 600 K and displays their change in orientation from cycle 0. GB atoms are removed from these images which allows for easy three dimensional visualization of grain shape. The red grain in the center rotates significantly during cycling and several boundaries migrate inward as atoms are transferred to neighboring grains. Figure 3-7(b) shows the relative change in grain size of the 5 grains as compared to their original size measured at cycle 0. There is significant transfer of atoms to the

green, purple, and orange grains as the boundaries separating these grains from the central red grain migrate inwards. Cooperative behavior of large rotation with simultaneous GB migration has been simulated by Upmanyu et al. [93] for embedded circular grains with various misorientations. Their results showed that GB migration occurs almost always during rotation except for those boundaries which are highly symmetric. Modeling of the crossover between curvature driven migration and grain rotation induced coalescence was conducted by Moldovan et al. [97], where relative contributions from each mechanism were found to be dependent on the average grain size. Cahn and Taylor [66] also modeled grain shrinking with simultaneous rotation and explained that either coarsening or shrinking could result as long as the total surface free energy is reduced. One of their physical explanations suggest that a migrating boundary allows for the rotation of small groups of atoms from one grain into another. The unit cell becomes distorted by the passing GB and collapses into the neighboring crystal configuration, assuming there is no special symmetry between grains preventing such GB movement. The majority of these models assume simplified microstructures which makes the emergence of these mechanisms even more interesting in our randomly oriented, three dimensional polycrystalline samples.

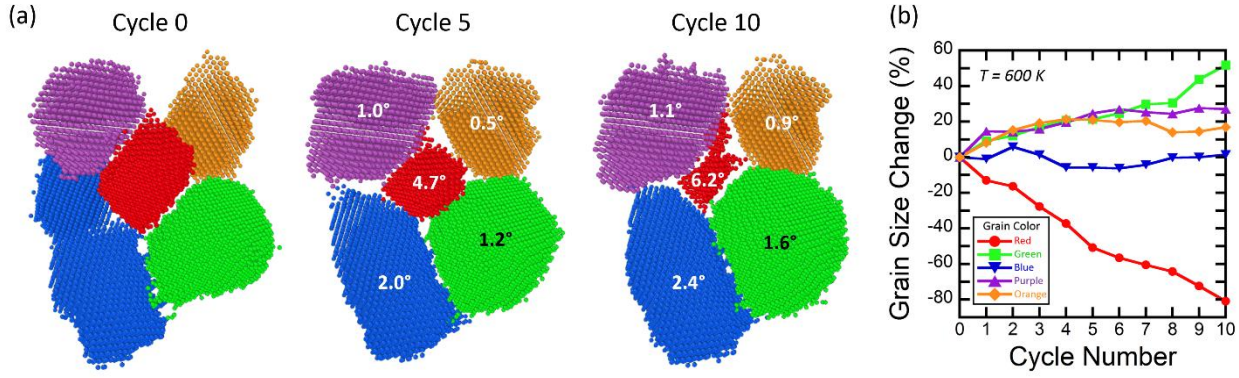

Figure 3-7 (a) Tracking of 5 different grains during 600 K cycling. Images show final arrangement of grains at the end of each cycle along with magnitude of rotation from original configuration at cycle 0. (b) Grain size evolution measured as percent difference from size measured at cycle 0 for the same 5 grains.

Deformation-induced grain growth is a common type of structural evolution in nanocrystalline metals. In our simulations, we find coarsening to occur primarily through the process of grain boundary migration and occasionally through coalescence of rotating grains. This resulting coarsening effect is highly temperature dependent and is captured in Figure 3-5(b), where average grain growth is plotted as a function of cycle. While a very small grain size increase does occur at 300 K (< 1%) and 450 K (< 3%), there is a dramatic increase in average grain size at the highest temperature of 600 K. It is important to note that no significant coarsening occurred during the initial equilibration at 600 K. Hence, the observed grain growth is driven by the mechanical cycling and plastic deformation, albeit aided by the elevated temperature. It is also important to reiterate that while these trends show an increase in average grain size there were in fact many grains which decreased in size throughout the simulation. We again refer to Figure 3-7 which shows a specific example of the discontinuous grain growth found throughout the Al sample as select grains coarsen or shrink while others keep a relatively constant volume. Discontinuous grain growth of nanocrystalline Al was observed experimentally by Gianola et al. [80] during tensile experiments on nanocrystalline Al thin films (d = 40-90 nm). These authors noted changes in the mechanical properties of the films, namely increased ductility but decreased strength. A previous study by Rupert and Schuh [98] involving repeated frictional wear of Ni-W also provided evidence of discontinuous grain growth, where the grain size distribution broadened with respect to the mean grain size. Similar findings are documented in our 600 K analysis. Of 44 initial grains, 10 showed significant decreases in size during deformation despite the drastic increase in average grain size. This equates to nearly 23% of the grains, several of which disappear completely before the end of the simulation. Because our samples had a very small starting grain size, the increases in strength and required flow stress that we are observing are in part due to inverse Hall-Petch

effect [25, 99, 100]. However, the 300 K sample exhibits minimal change in average grain size during cycling and still reaches a higher ultimate stress during the final tensile loading segment. This leads us to believe that there are other microstructural changes taking place which are contributing to the observed changes in mechanical properties.

Grain sliding was also tracked and quantified during cycling. To quantify sliding, we identified the center of mass of each grain and tracked how it moved with respect to each cycle. Figure 3-5(c) compares the average sliding for all grains within the sample at each of the three testing temperatures. Because the magnitude of this sliding motion is only on the order of angstroms, it is difficult to say that GB sliding lead to significant structural evolution. It is important to reiterate that our definition of grain sliding incorporates the movement of a crystallite's mass center. The trends in Figure 3-5(c) are similar to those found in Figure 3-5(a) and (b), with elevated temperature leading to more evolution. These metrics are likely related, as grain coalescence and coarsening can also shift the mass center. For example, GB migration moves the center of mass of a grain in one direction. Regardless, the magnitude of average sliding is relatively low, even with some contribution from the other mechanisms altering the grain center.

Since grain rotation was significant in the cycled samples, we next investigated to see if there was a trend toward a final texture. Figure 3-8 presents the final pole figure distribution of grain orientations for {100}, {110} and {111} type poles for all three temperatures at the completion of cycle 10. Comparing the three different testing temperatures, the total number of poles projected decreases at higher temperatures due to the increase in coalescence and disappearance of shrinking grains with increased thermal energy. Grain coalescence allows for a slight shift in the overall projections due to merging of low angle boundaries. However, this coalescence is not drastic enough to extract any conclusive final preferential texture. Any overall

changes in the projected poles were seemingly random and sporadic in distribution. This suggests that rotations are occurring in whichever direction is most energetically favorable during each strain cycle, depending on many complex features like compatibility with neighboring grains, and that these rotations lower the energy of the final grain boundary state. Grain rotation as a mechanism of energy reduction is a likely explanation and has been verified in early particle rotation studies [101-103] as well as recent computational work [93], which explains that nano-sized polycrystals will rotate towards local minima in grain boundary energy. Cahn and Taylor [66] have even postulated that coupling between grain rotation and boundary motion can sometimes increase the local interface energy of a grain as long as the configuration results in a decrease in overall system energy.

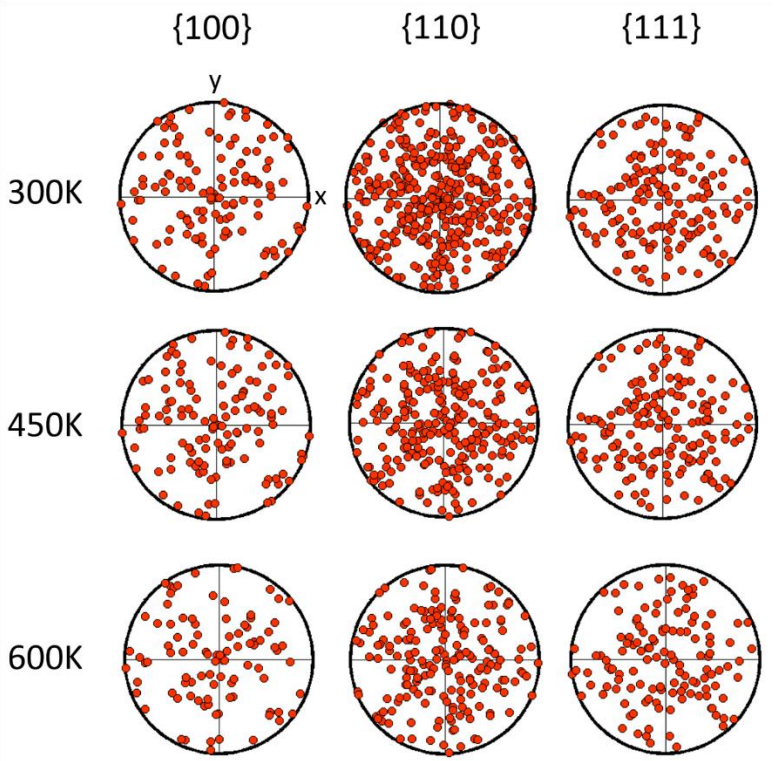

Figure 3-8 Final pole figures for all three samples taken after the completion of cycle 10. There is no discernable evolution toward a global texture.

In an effort to relate these structural changes to the mechanical response of our samples, we compare the trends of Figure 3-5 with our analysis of the peak stress difference in Figure 3-3(c). The majority of change in the peak stress difference occurs during the first three fatigue cycles. Additionally, the majority of average rotation and grain sliding has occurred by or before the 4th cycle, with the slopes of the trends dampening out even earlier at the two lower temperatures. The remaining grain restructuring that takes place at the higher cycles allows for additional reordering of the GB state through GB migration and changes in the faceting profile between grains. Specific examples of these changes to the grain boundary network will be introduced in the following section.

3.3.3 Local Changes to the GB Network

Local changes to the GB network were next identified and documented. Figure 3-9 shows cross sections of the final configurations (cycle 10) for each of the three testing temperatures. These cross sections were generated by cutting each sample at the same location and then coloring atoms according to their CNA value. Green atoms are those which have been identified as FCC, white are boundary or defect, and red are those exhibiting the HCP stacking sequence. The final disorientations (minimum misorientations) measured across several grain boundaries are presented in overlaid boxes. The numbers presented are not found by comparing the average orientations of the two grains, but instead by the local disorientation across each boundary. The color of each box corresponds to the absolute magnitude of total disorientation change (denoted $\Delta\Phi$) measured throughout the cycling process. In other words, the total amount of disorientation change measured at the end of cycle 10 with respect to cycle 0.

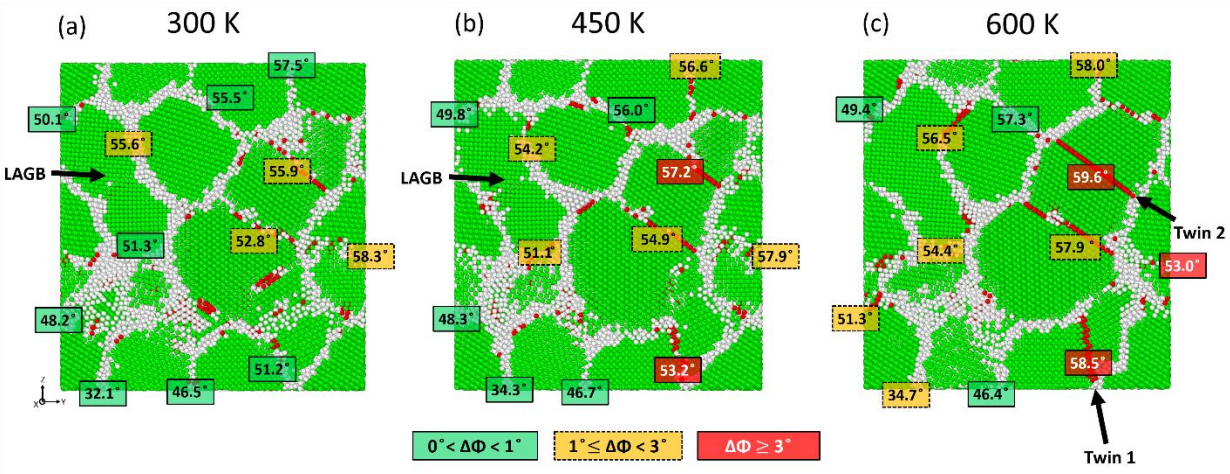

Figure 3-9 Cross sections showing the final microstructures of the (a) 300 K, (b) 450 K, and (c) 600 K Al samples after 10 fatigue cycles. Final disorientations measured across several boundaries are given in the small boxes with the color of the box representing the magnitude of the overall disorientation change (ΔΦ) accumulated since cycle 0.

To begin, it can be visually noted that the GB network has reached a more ordered state at the higher temperatures of 450 K and 600 K. Many GBs have evolved into twin boundaries, or single planes with HCP stacking sequence. To see how the magnitudes of relative grain rotation affect this transition, we look toward the values of ΔΦ. For the 300 K sample in Figure 3-9(a), the majority of disorientation changes during cycling were less than one degree, although a few grains exhibit relative rotation between one and three degrees. With such limited reorganization, dramatic structural evolution cannot occur and any changes to the GB structure should be subtle. Previous work has shown that high energy configurations can be relaxed through low temperature annealing or mechanical cycling [104, 105]. Such boundary relaxation can explain the improved mechanical response of the material post cycling and may be occurring in our samples during the first few cycles. Instead of a saturation in dislocation activity taking place like was seen in the previously mentioned fatigue study by Moser et al. [72], it is possible that we are instead observing boundary relaxation of energetic structural regions. Due to our reduced grain size, this boundary

relaxation is enhanced through GB plasticity and evidence of this enhanced strengthening response can be noted in Figure 3-3(c) during the initial cycles.

At the elevated temperatures, the overall relative rotation of grains was found to increase and we see more ordered GBs in Figure 3-9(b) and (c). In addition, several examples of boundary migration as well as faceted boundaries have helped reorganize the GB network. It is obvious that the most overall change in disorientations occurs in the 600 K sample, where many yellow and red boxes can be found. The red twin boundary at the bottom right of Figure 3-9(c) labeled "Twin 1" had a disorientation change greater than nine degrees during the simulation. The red box (53˚ disorientation) above and to the right of this boundary also exhibited a high level of grain rotation in order to accommodate the twinning process that took place in the neighboring grains below. Another twin is identified as "Twin 2." Whether or not these grain pairs reach the twin configuration appears to be highly dependent on temperature and connected to the increasing levels of rotation as temperature is increased. We also make note of the disappearance of a low angle boundary which is identified in Figure 3-9(a) and (b) but not found in Figure 3-9(c).

In order to quantify the evolution of the grain boundary state more clearly, we calculated the atomic percent of GB atoms as well as the relative atomic energies of these atoms. Figure 3-10(a) shows a decrease in grain boundary atomic percent with increasing number of cycles. Twin boundaries were included in this calculation since they separate two different crystal orientations and thus contribute to the grain boundary network. This decrease is partially due to fatigue induced coarsening and coalescence of grains, but there is also an effect of moving from random GBs to twin boundaries in some cases. Twins have very few GB atoms per unit area, because the interface is represented by a single plane of HCP atoms. Figure 3-10(b) shows the evolution of GB energy with cycling, measured by the excess potential energy as compared to the

atoms in the grain interior. Since there is very little dislocation activity present in our samples, their contribution to this calculation is minor. Figure 3-10(b) shows that the grain boundary network moves to a lower energy state during cycling.

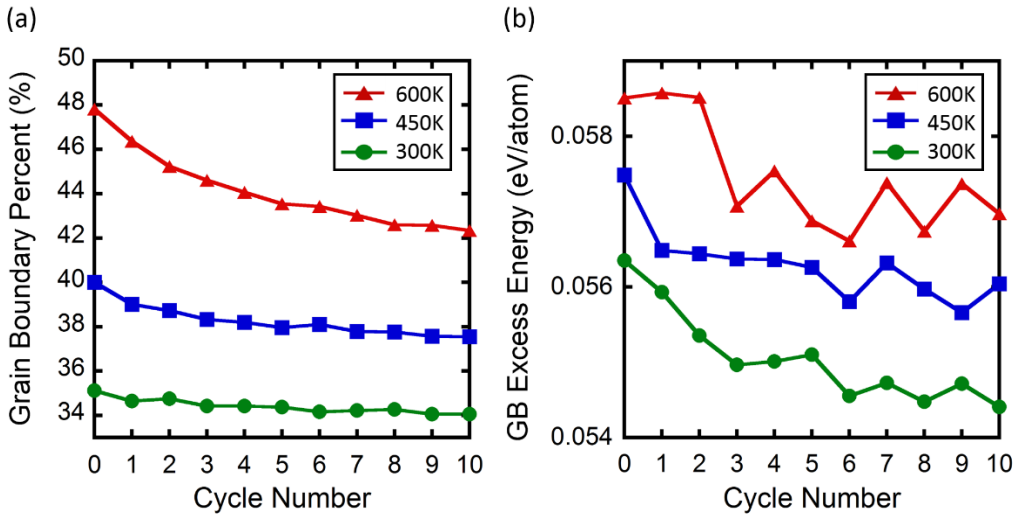

Figure 3-10 (a) Percentage of grain boundary atoms as a function of load-unload cycle. (b) Grain boundary excess energy as a function of load-unload cycle.

To further illustrate the process of twin formation, Figure 3-11 highlights eight neighboring grains within the 600 K sample. Several grains of interest have been color coded to help point out the collective microstructural rearrangement that took place during cycling, while the rest of the atoms are colored according to CNA. The random cross section in Figure 3-11(a) shows the starting configuration of the sample before any cyclic deformation has taken place. Figure 3-11(b)-(f) show how the microstructure evolves during mechanical cycling, where it is clear that many boundaries have reorganized into low energy configurations. Figure 3-11(g) presents the calculated misorientation angles between these highlighted grains as a function of cycle number. Multiple GBs converge to a Σ3 twin misorientation nearing 60° about a <111> type vector, while another (G4-G5) suggests that this trend will continue with an increased number of load cycles. We reiterate that all twins obtained their final configuration through a variety of axes of rotation.

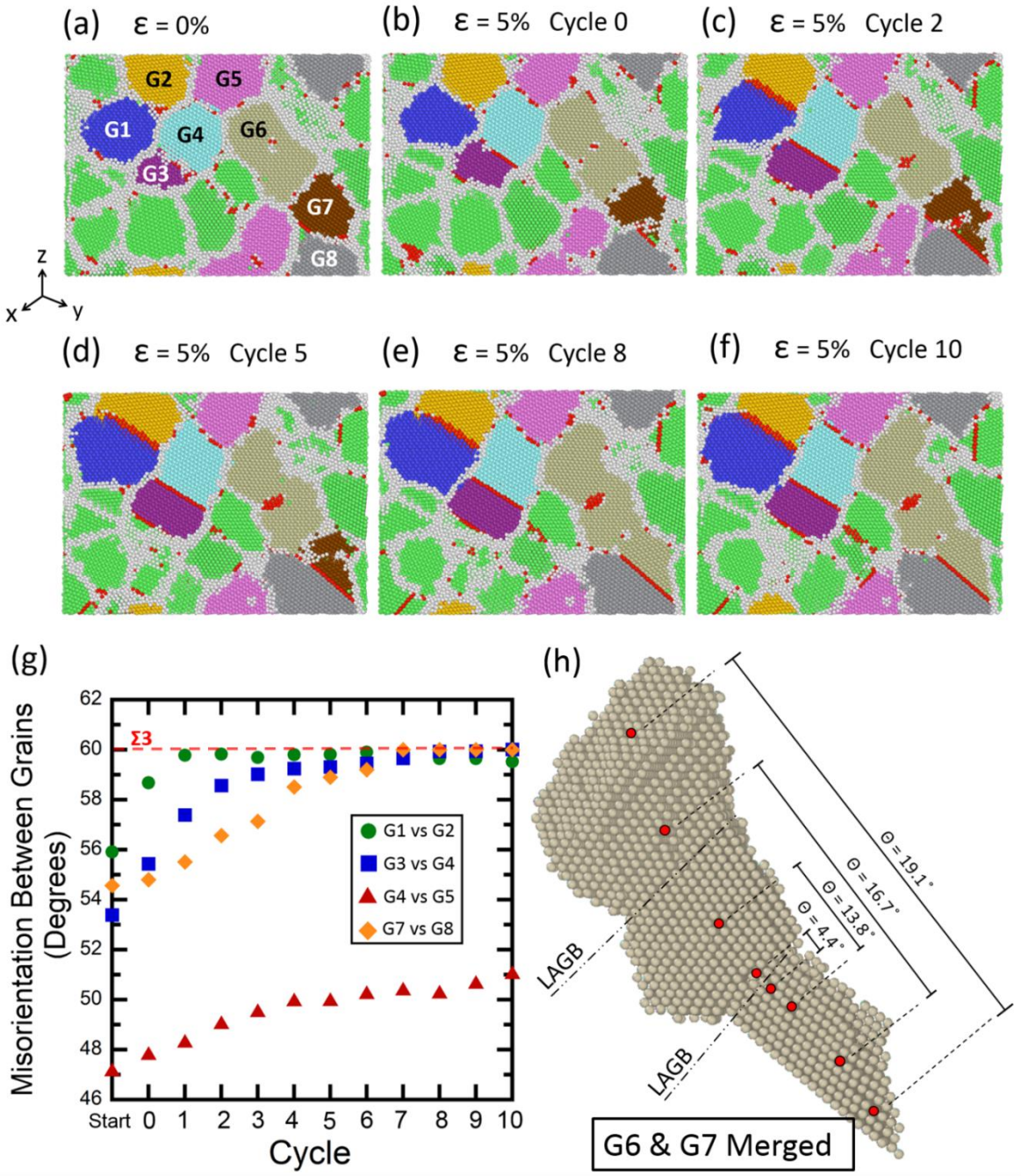

Figure 3-11 **(a) Snapshot of a cross section of the starting configuration for the 600 K cycled Al sample with grains numbered and colored for clarity. (b)-(f) The final configuration after select cycles, showing the evolution of microstructure of several grains. Rotation of grains allows for formation of several deformation twins. (g) Plots the misorientation between certain grains and shows that many of the grain pairs are converging to a 60° misorientation of a Σ3 twin boundary. (h) A three dimensional view of G6 and G7 after merging during cyclic loading. Misorientation between several points along this grain illustrates the bent configuration of this new crystallite.**

The twin formation between G7 and G8 eventually allows for a reduced misorientation across the original boundary separating G7 and G6. This twinning process, caused by grain rotation as well as the migration of the original separating boundary, ultimately leads to the coalescence of G7 and G6. Further analysis showed that although this grain was indeed identified by the GTA as one grain, the misorientation measured between several points in the grain varies significantly. This is not an error by the algorithm, but instead an example of a bent grain containing low angle grain boundaries. A three dimensional view of this grain post cycling can be seen more clearly in Figure 3-11(h), where the misorientations between several points along the grain have been identified. CSP identifies all atoms as being crystalline, and the GTA will only find two grains if the local misorientation (misorientation between an atom and its nearest neighbors) is > 3°. A similar phenomenon would be difficult to observe in conventional orientation imaging microscopy since these fine grain sizes are near the threshold of such experimental techniques. This is one of a few cases within the sample where two grains merge through a low angle grain boundary. Inspection of this grain shape revealed that the starting Voronoi configuration resulted in a low angle boundary already present within G6 and cycling enlarged this grain through another low angle boundary which initially separated it from G7. Hence, we are left two low angle boundaries within this grain, their approximate locations denoted in Figure 3-11(h). Analysis of this same grain at the lower temperatures showed considerably less grain rotation and no grain coalescence.

GB faceting as well as the development of coherence across certain twin boundaries was also found to occur more readily with increased temperature. Figure 3-12 shows an example of twin formation at 600 K, where the grain boundary plane is dynamic. The two grains are segregated by color and all boundary atoms have been removed from the images. In the starting configuration,

the boundary between these two grains would already be classified as Σ3 according to the well-established Brandon Criteria [106], but the GB is not coherent and the misorientation angle is not exactly 60°. After the first fatigue cycle, the misorientation is increased to almost exactly 60°. Figure 3-12(b) shows how, at the termination of the first cycle, two different boundary planes exist between these two grains. The interface on the right side is a coherent twin boundary (CTB) with a {111} boundary plane belonging to both crystals. The lower left half is incoherent and thus less energetically favorable. The increased mobility of such an interface facilitates GB migration [107]. When additional fatigue cycles are imposed, the incoherent boundary migrates in a direction parallel to the coherent boundary plane until the entire GB becomes a CTB. This process is highlighted in Figure 3-12(b) and (c) with black arrows signifying the direction of migration. The remaining cycles allowed for rearrangement of the faceting profile between the twinned grain pair as can be seen in Figure 3-12(d) and (e). The number of facet steps decreased with additional cycles, suggesting that the faceted structure is only an intermediate GB state that facilitates the transition to a perfect twin between the grains.

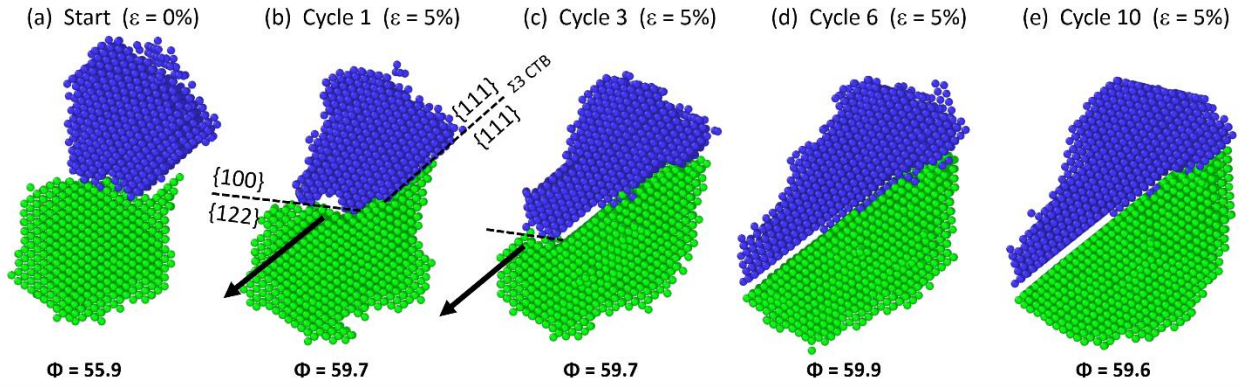

Figure 3-12 (a) Starting configuration of a select grain pair at 600 K with average misorientation listed below the image. (b) GB character of the twin boundary interfaces at the completion of Cycle 1 and start of incoherent boundary migration. (c) Continued migration of the incoherent twin boundary across the grain. (d) – (e) subtle changes in interface structure and GB faceting profile.

Based on these observations, we attribute the permanent increase in mechanical flow strength after high temperature cycling (as shown in Figure 3-2(a)) to the higher levels of structural evolution. The formation of low energy twin boundaries as a result of grain rotation is likely a major contributor to this effect. It is not uncommon in larger grained nanocrystalline metals for twins to have a significant impact on strength and ductility with many researchers striving to grain boundary engineer (GBE) metals by increasing twin densities [108, 109]. However, in nanocrystalline metals with fine grain sizes close to what was explored here, traditional deformation twins are rare and an inverse grain-size effect on twinning accounts for the higher levels of generalized planar fault energy needed to emit twinning partials [110]. The formation of special boundaries observed here could have important implications regarding GBE of nanocrystalline materials. Direct twinning by rotation, GB migration, and sliding may provide a path for increasing the fraction of special boundaries in a nanocrystalline grain structure, without the traditional GBE processes of dislocation network formation and recrystallization.

3.4 Conclusions

Quantitative characterization of nanocrystalline structural evolution due to novel GB deformation mechanisms is important for designing against fatigue and for grain boundary engineering. Because these plastic processes can be extremely difficult to observe even with costly in-situ experiments, we have used molecular dynamics simulations to observe and document trends in structural evolution during low cycle fatigue. The results shown here provide a quantitative analysis of several deformation mechanisms pertaining to nanocrystalline metals with extremely small average grain size. The following conclusions can be drawn from this study:

- Cyclic strengthening is observed and the magnitude of ultimate strength increase is dependent on the number of cycles. We attribute this strength change to the structural evolution which is driven by plasticity. Increased testing temperature ensures that this strength increase is permanent and persists to larger applied strains, by causing more obvious changes to the GB network.
- Both grain rotation and grain boundary migration were observed for all samples and can contribute to discontinuous grain growth as atoms are transferred between grains. Another byproduct of such growth is the shrinking and disappearance of many grains, with these grains often exhibiting the largest overall rotations.
- Grain growth was also found to occur through the coalescence of neighboring grains as misorientation between grains was reduced with more cycles and elevated testing temperature. This mechanism for energy reduction allowed for the formation of elongated grains consisting of several low angle GBs leading to the formation of bent grains.
- Grain sliding was tracked quantitatively and found to be temperature dependent, but ridged body translation of grains was not identified as being a dominant deformation mechanism. The overall magnitudes of grain sliding were found to be relatively small, on the order of a few angstroms.
- A significant number of twin boundaries were formed in the specimen cycled at 600 K as a result of collective deformation physics. Elevated temperature allows more rotation to occur by aiding GB diffusion, with rotation continuing until misorientation approaches the 60° misorientation angle of a Σ3 twin.
- The majority of evolution caused by grain rotation occurs in the first few cycles with additional cycles leading to a more ordered final GB state with fewer defect atoms.

Boundaries continue to migrate and begin to reorganize as twin boundary planes become more coherent with cycling.

This study has provided insight into the collective nature of GB-dominated deformation mechanisms which take place in nanocrystalline metals, with a specific focus on adding quantitative understanding. The ability to quantify relative contributions of each mechanism is necessary in order to identify any emerging trends in structural evolution during nanocrystalline plasticity. Since all grain structure attributes are available in an atomistic simulation, interesting and important individual examples of plasticity can be easily identified within the sample and explored in depth. These capabilities are what make this type of analysis a powerful tool for understanding the underlying physical processes that take place in nanocrystalline metals.

CHAPTER 4. Plasticity-induced Restructuring of a Nanocrystalline Grain Boundary Network[3]

4.1 Introduction

The results of Chapter 3 provided clear evidence that nanocrystalline deformation physics such as sliding [28, 64], grain rotation [18, 19, 25, 111], and grain boundary migration [112] can act collectively to alter grain boundary state. Because the grains themselves participate, these mechanisms evolve not only the grain shape but also interfacial structure during plasticity, and suggest that long-range evolution of the grain boundary network is likely for extremely fine grain sizes.

Evolution of grain boundary networks would open the door for grain boundary engineering of nanocrystalline materials, where the fraction of boundaries with "special" properties can be altered with thermomechanical processing [113]. One approach for identifying special boundaries is to characterize interfaces using the coincident site lattice (CSL) model [114], which assigns a value (Σ) to each interface corresponding to the inverse of the maximum theoretical number of lattice sites which are shared between neighboring crystals, deeming those with $\Sigma \leq 29$ as special. A recent example of grain boundary engineering extended to nanocrystalline metals was presented by Bober et al. [115], who utilized transmission Kikuchi diffraction (TKD) inside of a scanning electron microscope to conclude that nanocrystalline Ni thin films (d = 23 nm) subjected to thermomechanical cycling treatments will increase their $\Sigma 3$ boundary content as well as

[3] The contents of this chapter have recently been accepted for publication as Panzarino JF, Pan Z, Rupert TJ. Acta. Mater. 2016 *(in press)*

continually refine existing Σ3 boundaries to a more perfect misorientation. This study confirmed the potential for altering grain boundaries through nanocrystalline deformation physics, but these authors focused on statistical boundary metrics rather than micro-mechanisms of evolution due to the inherent lack of temporal resolution provided by ex situ characterization.

Kobler et al. [24] began to access time-resolved measurements by using automated crystal orientation mapping in the transmission electron microscope (ACOM-TEM) in combination with in situ straining. These authors found evidence of deformation-induced grain growth, grain rotation, and twinning/detwinning in nanocrystalline Pd films with d = 37 nm. However, because of the two-dimensional nature of data gathered by both TKD and ACOM-TEM, the orientation maps and boundary character distributions provided by such experimental techniques cannot confidently identify the grain boundary plane orientations (CSL only requires lattice misorientation between grains). In order to fully describe a grain boundary, the boundary surface normal (two parameters) in addition to the lattice misorientation relationship between grains (three parameters) must be determined [116]. Fortunately, all of the data required to calculate these features are readily available during atomistic simulations.

In this Chapter we update the GTA to include algorithms which are capable of segmenting interfacial regions and then extracting features like grain boundary surface normals, grain orientation/disorientation relationships, and triple junction structure, while simultaneously tracking these features as they evolve throughout a simulation. Such analysis tools provide fully characterized five parameter grain boundary data with spatial and temporal resolution that is currently inaccessible with experimental techniques. We then employ MD simulations in order to understand how plasticity at the nanoscale evolves grain boundary networks, subjecting nanocrystalline Al to both monotonic tension as well as mechanical cycling. Two grain sizes, 5

nm and 10 nm, were examined so that differences in grain boundary network evolution associated with different plasticity mechanisms can be observed. In addition, the effect of temperature on boundary evolution during plasticity is also studied.

4.2 Simulation methods

Samples with average grain sizes of 5 nm and 10 nm were constructed using the Voronoi method with random Euler angles assigned to each grain nucleation site [64, 75]. In addition, a minimum separation distance between grain nucleation sites was employed which allows for more equiaxed grains and a tight grain size distribution to more efficiently analyze the response of each specific grain size. For each sample, the same set of Euler angles was used to ensure that the starting texture and grain boundary structure would be identical despite the difference in grain size. The Large-scale Atomic/Molecular Massively Parallel Simulator (LAMMPS) [49] was used and all atomic interactions were described by an embedded atom method (EAM) potential for Al developed by Mishin et al. [117]. This many-body potential was developed using a combination of *ab initio* and experimental data with the intention of simulating internal defects and plasticity in Aluminum and was found to accurately describe point defects, planar faults, grain boundaries, and experimental values of stacking fault energy. A 2 fs time step was used for time integration during the simulation with periodic boundary conditions applied in all directions. Any overlapping atoms which were separated by less than 2 atomic radii were removed and the final structures were then relaxed using a conjugate gradient minimization with an energy tolerance of 10^{-6} eV and a force tolerance of 10^{-6} eV/Å. The resulting structures were fully dense and free of stored dislocations, containing 48 grains. The d = 5 nm sample contained 180,982 atoms with a cubic simulation cell side length of 146.5 Å and the d = 10 nm sample contained 1,480,503 atoms

with a side length of 294.4 Å. The samples were then annealed at 600 K for 100 ps to remove excess grain boundary dislocations and free volume [59, 81, 118]. This step ensures that any observed structural evolution is not merely a byproduct of unstable high-energy interfaces caused by the construction technique used to create the samples. After equilibration, samples were cooled at a rate of 30 K/ps until the desired testing temperature was reached. Although these Voronoi samples are the main focus of this work, we also compare with nanocrystalline atomistic models created using two other construction techniques that give slightly different starting microstructures. Further details of this additional analysis is provided in Section 4.3.

For mechanical testing, monotonic tension to 10% true strain and mechanical cycling were performed. Cycling was achieved through tension load-unload cycles. Specimens that had been loaded past the yield point to 5% true strain were first unloaded to 3% strain and then pulled back to 5% strain, with each unloading-loading pair representing a single cycle. This process of mechanical cycling was repeated for a total of 10 cycles. Both sets of mechanical testing simulations were run at temperatures of 300 K, 450 K, and 600 K, using a true strain rate of 5×10^8 s^{-1} while employing a Nose-Hoover isothermal-isobaric ensemble in order to keep zero stress in the lateral sample directions. A recent study by Zhang et al. [119] showed that, for nanocrystalline Cu, the grain boundary mediated modes of plastic deformation are not strain rate dependent in the range of 1×10^7 s^{-1} - 1×10^{10} s^{-1}. Figure 4-1 illustrates the deformation methodology and typical results for monotonic tension (black curve) and mechanical cycling (red curve) of the d = 5 nm sample at 300 K. For monotonic tension, atomic snapshots were output at the starting configuration and at each strain increment of 1%. For the tension unload-load cycling, simulation snapshots were recorded before deformation (0% strain) and each time the sample reached 5% strain. These snapshots were subsequently analyzed using the Grain Tracking

Algorithm (GTA) [88], after incorporating the improvements detailed in Section 3, and visualization of the resulting data was performed by the open source particle visualization tool OVITO [52]. The updated GTA is freely available through the corresponding author's research website or can be obtained by contacting the corresponding author.

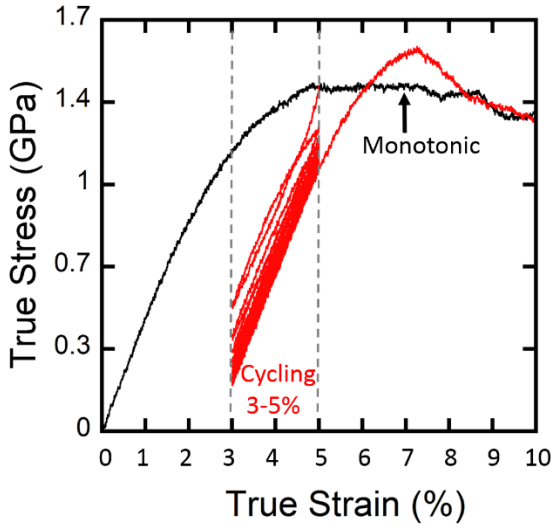

Figure 4-1 Mechanical response of d = 5 nm sample loaded monotonically (black line) and cyclically (red line) at 300 K. Dotted grey lines illustrate the mechanical cycling procedure. Identical loading procedures were performed at 450 K and 600 K.

4.3 New analysis methods

- The GTA was recently developed to provide grain identification, texture analysis, and grain structure evolution for atomistic simulation outputs. As outlined in the previous chapter that summarizes the initial development of the tool [88], spatial coordinates of the atoms along with a crystallinity description (e.g., centrosymmetry parameter (CSP) [45] or common neighbor analysis (CNA) [120]) are all that is required to identify and track crystallites and their orientations during the simulation. CSP is a measure of the local lattice disorder surrounding an atom and was chosen here to distinguish between crystalline and non-crystalline/defect atoms within our samples. A threshold of CSP $\geq$ 2.83 Å^2 was

chosen to signify non-crystalline atoms in this study based on the Lindemann-Gilvarry rule [50], which establishes the maximum bond length allowable for an atom contained in a crystalline environment before melting occurs. Once atoms have been separated into crystalline and non-crystalline, the GTA calculates the lattice orientation at each crystalline position within the sample and uses this information to segment the sample into individual grains. The grain segmentation technique compares the disorientation angle (smallest symmetrically equivalent misorientation angle) between lattice orientations measured at each atomic position and compares these disorientations with an allowable cut-off angle. Any neighboring atoms which fall within this cut-off are deemed part of the same crystal. To improve grain segmentation during high temperature, all nearest neighbor vector combinations which determine a set of axis at each crystalline point are averaged to allow for more robust orientation determination. Using fcc as an example, the orientation determination procedure outlined by Panzarino et al. [88] is repeated for all 12 nearest neighbor position vectors providing 12 sets of axis which are then averaged. In addition to grain segmentation, the GTA algorithm also provides a mapping between time steps, allowing for the tracking of features such as grain size, grain rotation, and grain sliding. Figure 4-2(a) shows the d = 10 nm microstructure with atoms colored according to grain number, as well as an accompanying pole figure indicating a randomly oriented starting texture of the grains.

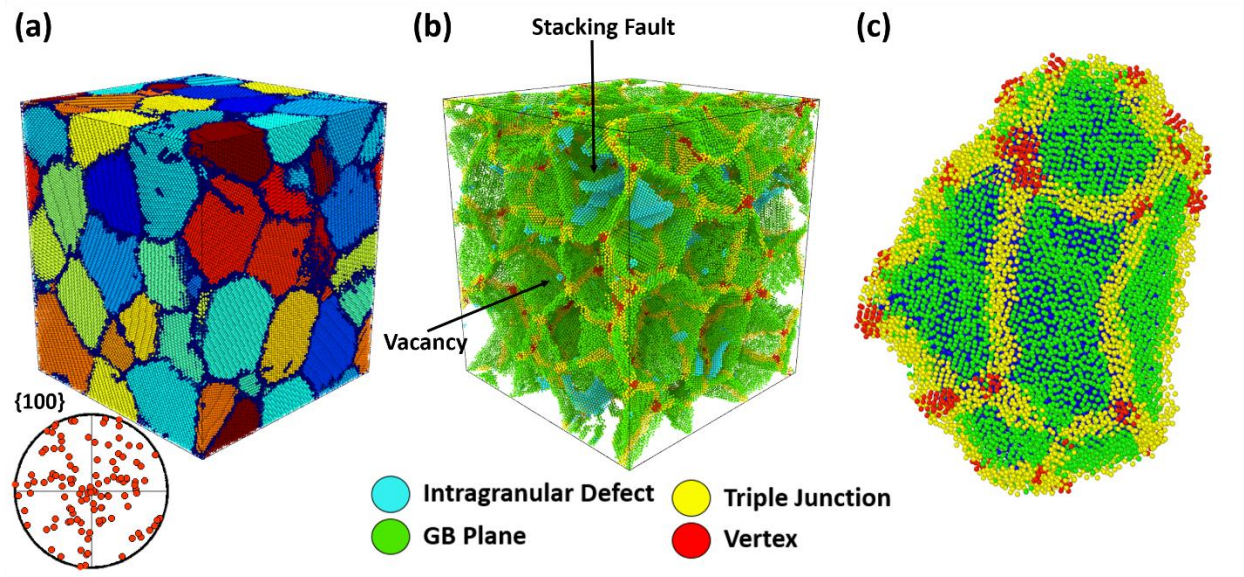

Figure 4-2 (a) The d = 10 nm sample at 10% true strain and 600 K with all grain identified. The {100} pole figure indicates random texture throughout the sample, even after tensile deformation. (b) The grain boundary and intragranular defect network of the same sample with atoms colored according to defect type. Blue atoms are intragranular defects (stacking fault, void, or interstitial) while green, yellow, and red atoms are grain boundary plane, triple junction, and vertex points, respectively. (c) A single grain surrounded by the various grain boundary network atom types.

To allow for quantitative analysis and tracking of important features of the grain boundary networks, the GTA was updated in several important ways. Having calculated grain structure and orientation information, the algorithm now proceeds to distinguish between the several types of interfacial atoms within the microstructure. Boundary atoms which reside between two grain neighbors are deemed grain boundary plane atoms, while those with three neighbors belong to triple junctions and four or more neighbors are classified as vertex point atoms. Remaining non-crystalline atoms which have only one grain neighbor (meaning they reside within the grains themselves) are deemed intragranular defect atoms can be associated with a dislocation, stacking fault, vacancy, or interstitial. An example of this classification can be seen in Figure 4-2(b), where all crystalline atoms have been removed. Intragranular defect, grain boundary plane, triple junction, and vertex atoms are colored light blue, green, yellow, and red, respectively. Examples of a stacking fault and a vacancy are labeled. Figure 4-2(c) displays an example of an isolated

grain extracted from the computational model using the same atom classification scheme. A similar boundary atom classification was used by Xu and Li [39], but their approach obtained grain numbers and crystal orientations from the initial Voronoi construction. An outward layering method was then used to identify the different boundary atom types. Our method is similar in its classification scheme but also allows for the indexing of microstructures with no a priori knowledge of grain locations or orientations. Such a feature is essential for tracking boundary features during a simulation, as the material evolves.

After indexing atom types, the updated GTA then calculates the disorientation angle and axis of rotation between all neighboring grain pairs so that features such as Σ type in the CSL framework can be calculated. It is important to note that the CSL framework is simply one choice for describing grain boundary character distributions and there are others such as grain boundary plane distribution [121] and disorientation axis distribution [122]. Since the GTA calculates all five degrees of freedom for a boundary, any of these methods is an option. We choose to use Σ type here to describe boundary character so that our findings can be readily compared to experimental reports. The Brandon criteria [123, 124] defines the maximum allowable mis-misorientation offset, $\Delta\theta$, of an interface from a perfect Σ misorientation relationship and is typically defined as $\Delta\theta_{max} = 15°/\Sigma^{1/2}$. Here we use the Brandon criteria, but again a simple modification the GTA script would allow for the use of other metrics. Figure 4-3(a) shows a nanocrystalline sample with all grain boundary plane atoms colored according to their disorientation angle. The lighter colors indicate higher angle grain boundaries and the boundaries highlighted in blue are special boundaries, or interfaces with $\Sigma \leq 29$ in the CSL notation.

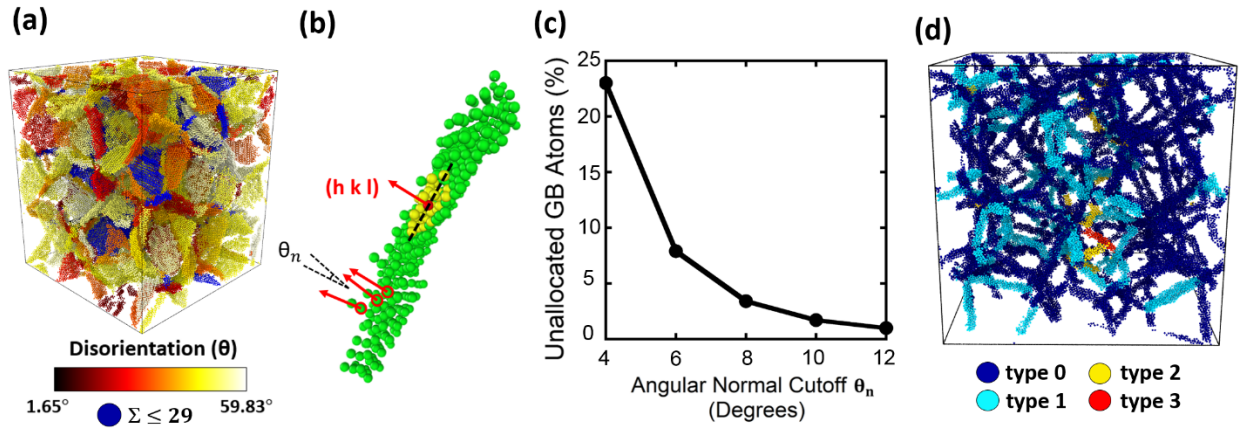

Figure 4-3 (a) Grain boundary plane atoms colored according to disorientation angle. Special boundaries are highlighted in blue. (b) Example of a cluster of grain boundary plane atoms where a specific atom (red) and 50 of its neighbors (yellow) were used to calculate a local plane normal. This process is repeated until all grain boundary interface atoms are assigned a normal vector. Neighboring normal vectors must deviate by less than a specified angular cutoff value in order to be considered part of the same boundary plane. (c) The effect of varying the angular cutoff on the number of grain boundary interface atoms which are allocated to planar sections. (d) The triple junction network colored according to junction type.

In order to fully characterize a grain boundary and its structure, the grain boundary normal must also be determined. Since the CSL model is only related to the angle and axis which describe misorientation, each Σ type can actually exhibit infinitely many variations depending on the dividing plane which separates the two crystals. A recent study by Homer et al. [125] illustrates the importance of boundary plane-property relationships in Ni and Al bicrystals using a technique developed by Patala and Schuh [126] to rewrite grain boundary normals in terms of a symmetry-capturing fundamental zone. Their results showed that for various special boundaries, grain boundary energy and excess free volume can vary dramatically depending on the grain boundary plane orientation, with only specific boundary normals exhibiting energy minimums. This additional boundary data is essential for understanding the role of interface planes in grain boundary network evolution and several other emerging studies also highlight the importance of a complete grain boundary character analysis which includes such information [127-129].

To obtain the grain boundary normal, the updated GTA segments the grain boundary plane atoms into planar sections based on whether or not each atom and its neighbors constitute a relatively flat section, which allows for the identification of faceted boundaries. First, local surface normals are calculated at each grain boundary atom using a singular value decomposition to find a best-fit plane for each atom and a surrounding cluster of its nearest neighbors. Singular value decomposition determines a plane which minimizes the square sum of the orthogonal distances between the points and the best-fit plane. For nanocrystalline microstructures, a cluster of 50 grain boundary neighbor atoms appropriately captures accurate interface normals at each atom, with an example shown in Figure 4-3(b). This process is repeated for all of the atoms in the boundary and a normal is assigned to every atomic position. When building up a grain boundary section, a grain boundary normal variation angle, θ_n, must be selected which provides a maximum allowable normal variation between neighboring atoms. Figure 4-3(b) illustrates this concept by showing three neighboring atoms with their normal vectors assigned and how their orientations can vary by θ_n. A convergence study was performed to find an adequate grain boundary cutoff angle. The grain boundary network of the 10 nm average grain size sample (T = 450 K) was analyzed at 10% strain while varying θ_n from $4 - 12^{\circ}$ and recording the amount of grain boundary atoms which were unable to be allocated to grain boundary sections. The results of the convergence study can be seen in Figure 4-3(c). A value of 8° allows for reasonable accuracy and the ability to segment flat sections of grain boundary, while also ensuring that there are only a small number of non-allocated interface atoms. For stricter cutoff angles, many atoms within grain boundary planes would be unallocated. Alternatively, larger cutoff angles would not adequately segment curved interfaces into planar sections. Proper selection of this normal cutoff angle is important for nanocrystalline systems with very small grain sizes, where planar grain boundary sections tend to

be very small and grain boundaries can be highly curved. With boundary plane normal identified, all five grain boundary parameters in an atomistic sample can be fully characterized.

With boundaries completely described, higher level topological features such as triple junctions can also be quantified. Depending upon how many of the connecting interfaces exhibit special character, triple junctions can be assigned a designation number or triple junction type. Since connectivity of high energy interfaces also has implications regarding percolation of fracture-susceptible boundaries [130, 131], several past studies have focused efforts on characterizing triple junction type distribution and cluster connectivity using two-dimensional computational models or orientation imaging microscopy scans [132-135], with a three-dimensional numerical study utilizing a tetrakaidecahedra model for the grain shapes [136]. In order to be consistent with this previous work, triple junction types are assigned here as follows: junctions with no attached special boundaries are deemed type 0, junctions with one special boundary are called type 1, and so on. Figure 4-3(d) shows the triple junction network in the d = 10 nm sample where the atoms are color coded by type number. Analyzing the density as well as connectivity of these special interface types can help illuminate the role of triple junction topology during microstructural evolution.

4.4 Microstructural evolution during plastic deformation

4.4.1 Monotonic loading

First, the effect of simple monotonic plasticity on the grain boundary network is studied. During deformation, evolution of the grain boundary character distribution was analyzed and special boundary fractions are reported. The fraction of boundary atoms which are detected as having $\Sigma \leq 29$ is plotted as a fraction of the total number of grain boundary plane atoms. Since

this metric is an atomic fraction, our calculation will be similar to length fraction, but with an added grain boundary thickness component which we expect to have minimal effect. Grain boundary special fractions are presented in Figure 4-4(a) and 4(b), as a function of applied strain, for the d = 5 nm and d = 10 nm samples, respectively. As the 5 nm grain size samples are deformed, the fraction of special boundaries shows some fluctuations, with the general trend that the special fraction increases during the majority of the plastic deformation range. These increases in special fraction occurred through both an increase in the length of existing special boundaries as well as the development of new special boundaries that were not present before deformation. Occasional jumps in the data are a result of large boundaries which evolve into or out of special character as additional grain rotation occurs, so it is most instructive to look at general trends. Most obvious is the fact that, tension at higher temperatures led to faster increases to the special boundary fraction. Further inspection showed that boundaries with low potential energy were more likely to cease rotation and hold a consistent disorientation relationship after their formation. For example, Σ3 boundaries became sessile if {111} boundary planes were formed. However, other Σ3 boundaries with randomly oriented boundary planes were not guaranteed to keep their character through the rest of the deformation process and occasionally moved away from a special configuration. Similar behavior was observed for other special boundaries as well. This importance of grain boundary plane on boundary stability highlights the power of being able to extract such information from atomistic datasets, a capability enabled by the updated GTA.

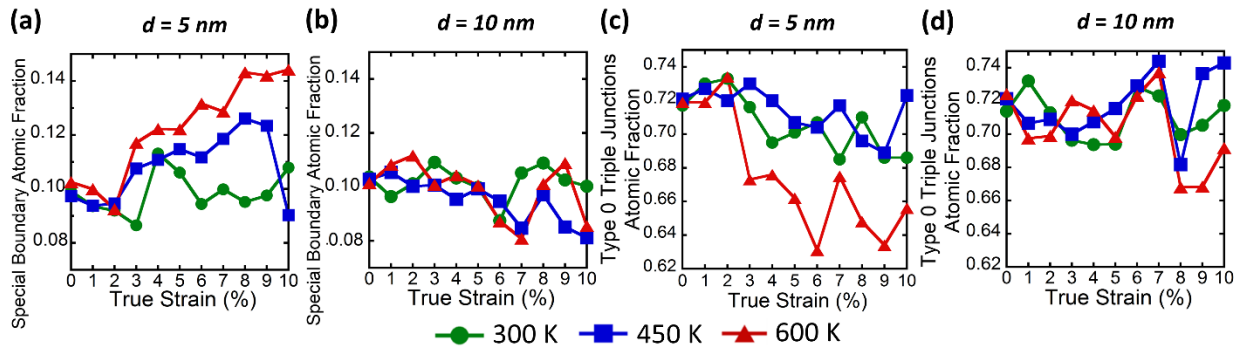

Figure 4-4 The evolution of special boundary fraction for (a) d = 5 nm and (b) d = 10 nm monotonic tension tests at all testing temperatures. (c) Type 0 triple junction analysis for d = 5 nm sample, showing evolution which was inversely proportional to the special boundary fraction evolution. (d) Type 0 triple junction fraction for the d = 10 nm grain size exhibits fluctuations, but no discernable upward or downward trend.

For the 10 nm samples, the grain boundary special fraction remained relatively constant with some fluctuations around the starting value. This difference can be attributed to the larger grain size, where dislocation-based mechanisms start to dominate. Schiotz and coworkers [26, 27] noted an inverse Hall-Petch relationship in the flow stress of simulated Cu when average grain size fell below 10 nm and further inspection showed that plastic strain was highly concentrated at the grain boundaries in the finest grained samples. Kadau et al. [137] also showed that a transition in plasticity mechanisms occurs near this grain size for Voronoi-created Al samples tested by MD. In our analysis, grain rotation is found to be significantly restricted for the larger grain size and an increase in the density of residual stacking faults left in the microstructure was observed for the 10 nm sample, which are both consistent with a shift toward dislocation-based plasticity mechanisms. In addition, no significant reduction in the potential energy of special boundaries was measured during deformation of the larger grain size sample.

The accompanying triple junction network was also tracked, with Figure 4-4(c) and (d) showing the evolution of type 0 triple junctions as a function of applied strain. The measurement

of triple junction fraction was carried out in a fashion similar to special boundary fraction, with the total number of atoms residing in each triple junction type divided by the total number of triple junction atoms present. The decrease in type 0 triple junction fraction for the d = 5 nm sample is a direct consequence of the increase in special boundary fraction with applied plastic strain. With more and more special boundaries, it becomes less likely that a triple junction will not have a special boundary attached to it. Because of the limited change in special fraction for the d = 10 nm sample, there was no clear trend in type 0 evolution. The remaining triple junction types were also analyzed, but no obvious trends were found and no additional insight was obtained through the metric that could not otherwise be portrayed in the special fraction data.

Connectivity and topology of the boundary network was also analyzed to understand if any long-range evolution is occurring. Since it is known that connectivity of the grain boundary network relates to intergranular failure such as fracture and corrosion [131, 138-142], the size of connected "random boundary clusters" of non-special boundary atoms was measured. Figure 4-5 compares a two-dimensional slice of the d = 5 nm sample at strains of 1% and 10% at 600 K. Special boundaries, triple junction types greater than zero, and vertex points which adjoin these special features were removed from the slices, since special interfaces tend to be less susceptible to intergranular failure. The remaining grain boundary atoms are segmented into clusters and colored using the cluster analysis tool developed by Stukowski [52] which groups clusters of particles using a user-specified cutoff radius, with a cluster radius of 6 Å used for Figure 4-5. A comparison of Figure 4-5(a) and (b) shows that there is significant break-up in the random boundary cluster size with increased plastic strain. This means that, for example, a crack moving from left to right through the microstructure would not be able to find a path which only propagates along random, non-special boundaries. The connectivity of random boundary clusters in two-

dimensions is commonly reported in the experimental literature for grain boundary engineering (see, e.g., [113, 143]). However, extension to three-dimensional analysis, available in our simulation method but not generally available from experiments, shows no large changes in cluster number or average size. Even though the network is broken up locally along a two-dimensional slice, the additional dimensionality allows for more percolation pathways and any breakups can be potentially bypassed through another route present in the grain boundary network. In fact, Figure 4-5(c) is the same sample at 10% strain with blue atoms illustrating the single three dimensional cluster that exists despite the fact that the special boundaries (green), triple junctions of type greater than zero (yellow), and vertex points (red) were removed from the cluster analysis. Again, this observation highlights the utility of atomistic modeling for analysis of boundary network features with additional detail.

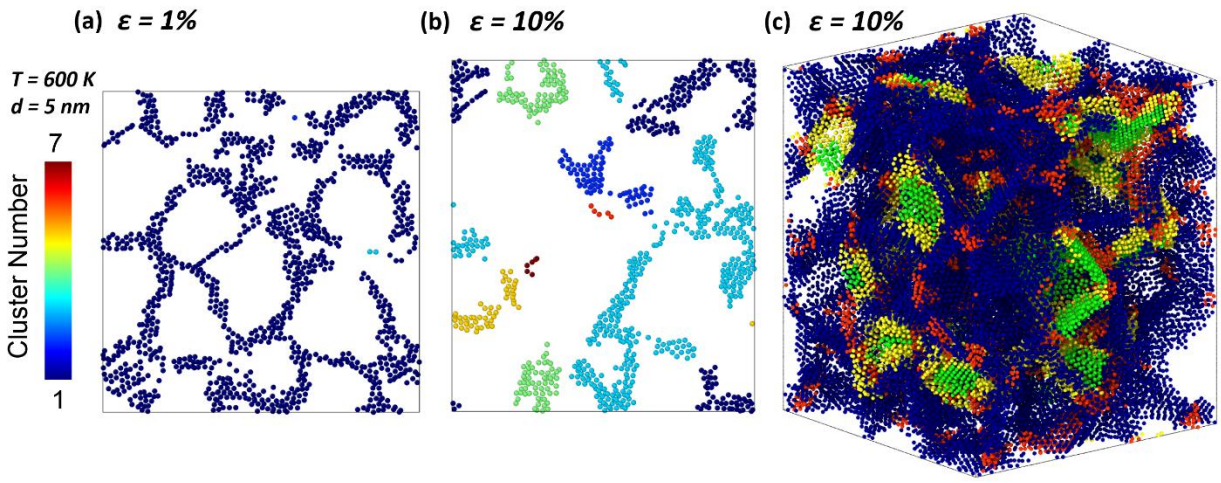

Figure 4-5 Two-dimension cluster analysis of the d = 5 nm grain boundary network. For both (a) and (b) only those atoms which are not special nor are part of a special junction type are analyzed, with the colors associated with different boundary clusters. After being pulled to 10% strain, a clear breakup in the random network is observed. (c) The same sample with special boundaries (green), triple junctions (yellow) and vertex points (red) which were removed from the cluster analysis. The remaining atoms (blue) make up a single cluster which maintains connectivity throughout the sample.

4.4.2 Cyclic loading

According to Figure 4-4(a), the majority of special fraction increase occurred within the intermediate 3-8% strain range and higher temperatures magnify this effect. In an attempt to drive further reconstruction of the grain boundary network, mechanical cycling in the range of 3-5% true strain was simulated. Figure 4-6(a) and (b) plot the special boundary atomic fractions, with the X-axis beginning at the starting configuration of 0% strain (labelled "Start") and then showing data from the end of each cycle (Cycle 0 is the initial loading to 5% strain). It is clear from Figure 4-6(a) that cycling at higher temperature gives a faster increase in special boundary fraction for the d = 5 nm sample. In fact, cycling at 300 K does not clearly alter the special fraction in an obvious manner. Like monotonic loading, the observed evolution is due to both an increase in the length of existing special boundaries as well as the emergence of new special boundaries. Figure 4-6(b) shows the special boundary fraction evolution for the d = 10 nm grain size as a function of cycle number. There is a noticeable decrease in the special boundary fraction during the 600 K cycling, as well as a small decrease for cycling at 300 K and 450 K. Generally, there is significantly less evolution for the larger grain size. For the 5 nm grain size, it is instructive to compare the special boundary fraction achieved through mechanical cycling to that obtained with monotonic tension. By the 10th cycle, the d = 5 nm sample tested at 600 K contains a 0.175 fraction of special boundaries (or an increase of ~75% from the starting value) whereas simple tension only resulted in a fraction of 0.12 or less for all strains at or below 5%. Even considering all possible strains up to 10%, monotonic tension only results in a 0.14 special boundary fraction. While monotonic tension and mechanical cycling both increase the special boundary fraction in these samples, cyclic loading allows for extra boundary rearrangement to occur.

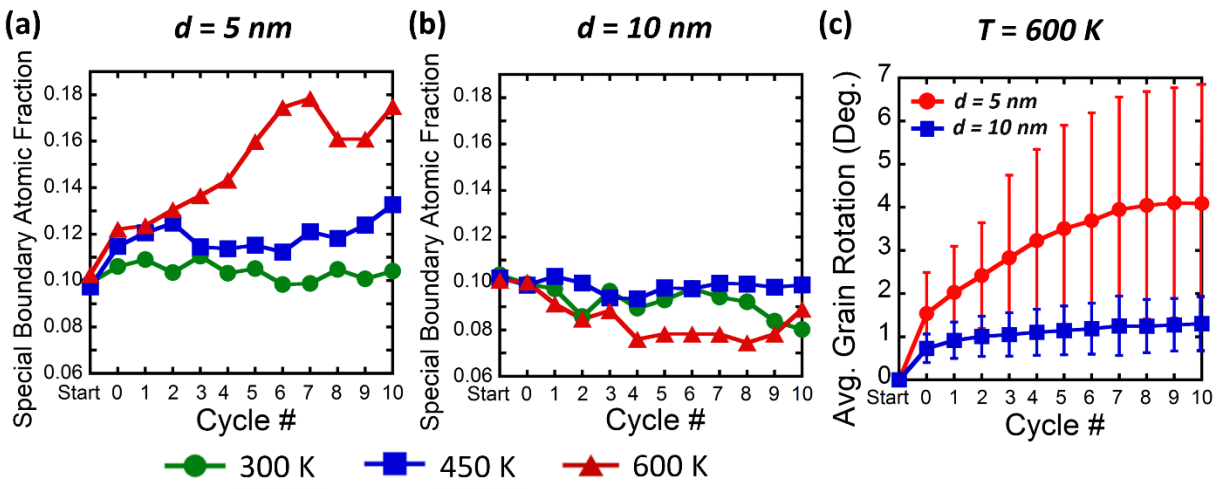

Figure 4-6 Special boundary fraction of mechanically cycled samples for (a) d = 5 nm and (b) d = 10 nm for all testing temperatures. (c) Average grain rotation, measured as the disorientation from a grain's starting configuration, for 5 nm and 10 nm average grain sizes cyclically loaded at 600 K.

The main difference in grain boundary network evolution between these two grain sizes can be attributed to increased activation of grain rotation in the smaller grain size sample, as shown in Figure 4-6(c) where average grain rotation is plotted as a function of cycle number for the 600 K simulations. Here, grain rotation is measured as the angular disorientation of a grain from its starting configuration (Start), before any deformation was imposed. As a whole, the d = 5 nm sample experienced roughly three times as much grain rotation as the 10 nm grain size sample. It is also important to note that these values are averaged over all grains in the sample. For example, there were several grains in the d = 5 nm sample which rotated more than 5 degrees, but none in the d = 10 nm sample. The error bars in Figure 4-6(c) show the standard deviation of the grain rotation angles. This grain rotation was often accompanied by simultaneous grain boundary migration of known high-energy interfaces. For example, non-coherent sections of Σ3 boundaries migrated to allow for lengthening of coherent Σ3 sections. This type of evolution was found to occur for other types of special boundaries as well. Figure 4-7 displays a more detailed picture of the resulting evolution for all special boundaries in the d = 5 nm and d = 10 nm samples that were

mechanically cycled at 600 K. Σ13, Σ17, Σ19, Σ21, Σ25, Σ27, and Σ29 boundaries each have "a" and "b" variations that were tabulated but these are reported here in a combined fashion using their respective Σ value. Variations in CSL types are a result of specific Σ boundaries which have multiple disorientation angle/axis pairs which result in the same reciprocal coincident site density [106]. Figure 4-7(a) indicates a distinct increase in Σ3 and Σ11 boundaries, while other Σ types show no clear trend or even slight decreases (see the Σ15 population). In contrast, Figure 4-7(b) illustrates noticeably lower special fraction evolution within the d = 10 nm microstructure during cycling and lack of a clear trend.

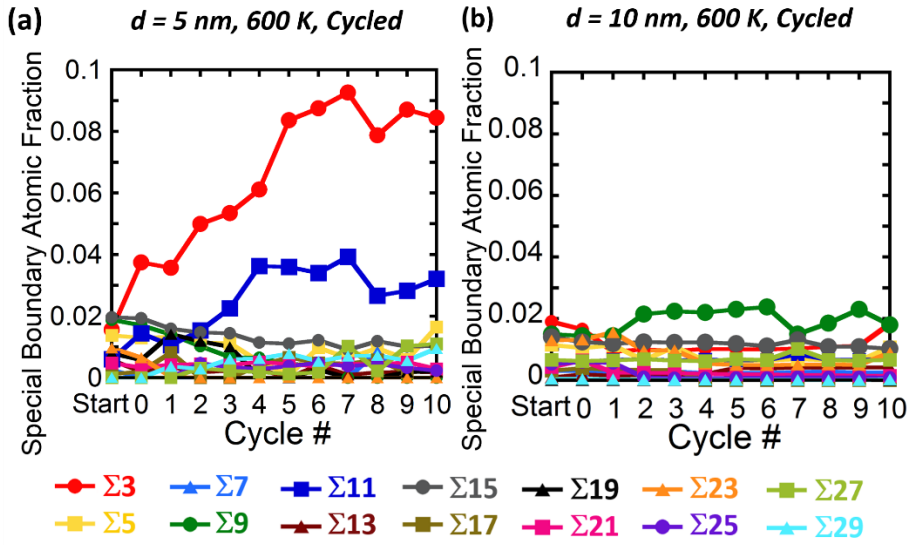

Figure 4-7 Special boundary fraction for the (a) d = 5 nm at 600 K sample shows an increase in Σ3 and Σ5 boundary content. (b) The d = 10 nm samples experience very little evolution of the special boundary fraction during cycling.

It is widely reported that special boundaries can exhibit low energy, but this is really only rigorously true for certain interface plane normal values [144, 145]. Additionally, several computational works [66, 93, 146] and experimental studies [147, 148] provide evidence that grain rotation is a mechanism by which interfacial energy can be reduced. Therefore, one explanation

for the increase in Σ3 and Σ11 boundaries is that rotation-mediated boundary rearrangement allows for the emergence of these special boundary types once favorable grain boundary planes are achieved. Early experimental works studied rotation-induced formation of special boundaries through the use of single crystal particles sintered to flat plates [102, 148]. Since the particles were sitting freely on top of the substrate, they were unconstrained by any neighboring crystals and thus free to rotate during sintering. Herrmann et al. [148] discovered the strong emergence of Σ3 as well as Σ11 boundaries during the sintering of both Cu and Ag particles in this type of experiment. Because our present study shows high levels of grain rotation for d = 5 nm, this suggests that nano-grains are able to rotate to low-energy cusps in the boundary energy landscape in a similar fashion.

Analysis of several specific special boundary types is presented in Figure 4-8(a), where the average atomic potential energy is plotted versus cycle number. The remaining special boundary types that are not shown follow roughly the same trend as the Σ5 boundaries. The average potential energies of crystalline atoms as well as random boundary atoms are also presented as grey and black data points, respectively. Even before loading of any kind, the pre-existing Σ3 and Σ11 boundary atoms have lower energy than other grain boundary atoms, foreshadowing the restructuring to come that will increase their fraction within the microstructure. The Σ3 boundary atoms approach a lower energy state with added cycles, especially after the initial pull and first cycle. Additional analysis of the Σ3 boundaries shows that the average mis-misorientation, or angular deviation from the perfect CSL disorientation, decreases with cycling, meaning that they are becoming closer to a perfect Σ3 misorientation. This mis-misorientation evolution of Σ3 boundaries for the d = 5 nm samples is shown in Figure 4-8(b). The majority of the Σ3 boundary planes evolve to coherent {111} planes by the 10^{th} cycle, while those that did not were the facets that enabled {111} plane formation elsewhere. Visual evidence of this is shown in Figure 4-8(c),

which displays all Σ3 boundaries at Cycle 10 for the d = 5 nm, 600 K sample. In contrast, the average energy of all Σ11 boundaries was relatively low in the original configuration and only fluctuated slightly with cycling. The Σ5, Σ9, Σ27 boundaries did not undergo significant evolution, with their energies roughly matching the average atomic energy of the remaining random boundaries. Data for the Σ9 and Σ27 boundaries does not appear across all cycles because they were not always present in the sample. Finally there is even some slight reduction in the average energy of crystalline atoms which can probably be attributed to structural relaxation of the system during early loading.

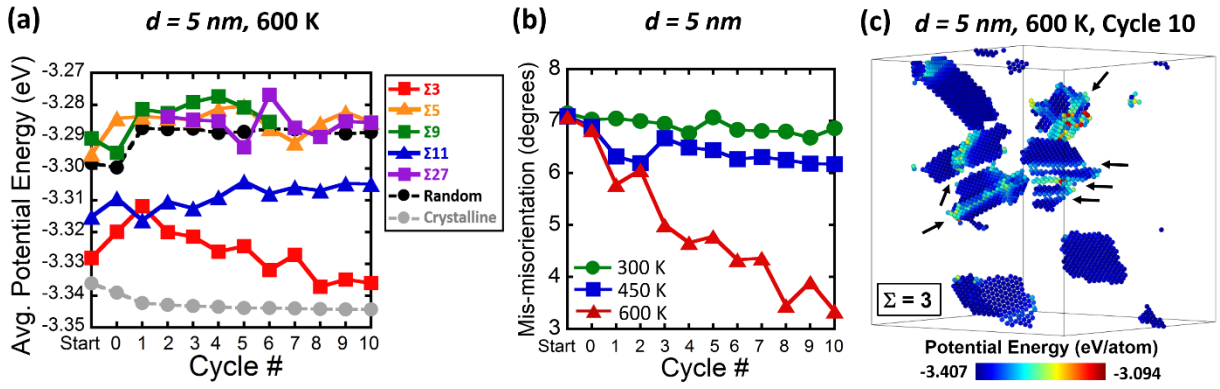

Figure 4-8 (a) Average potential energies of select special boundary atoms, random boundary atoms, and crystalline atoms during cycling. (b) Mis-misorientation of Σ3 boundaries as a function of cycle number. (c) Σ3 boundaries at Cycle 10, with black arrows indicating facet steps which allowed coherent segments to form.

Knowing that Σ3 and Σ11 boundaries were evolving to reduce interfacial energy, site specific occurrences of the formation of these boundary types were then studied to obtain more insight into the underlying restructuring mechanisms. As an example, Figure 4-9(a)-(c) follows the structural rearrangement and formation of four special boundaries which all border a common grain. For clarity, the crystalline atoms as well as triple junction and vertex point atoms have been removed. By Cycle 4, three of the interfaces have become special, having evolved from previously random boundary types. The details of each misorientation relationship are listed below each

snapshot and color coded according to the respective boundary. After first listing the Σ value, the disorientation angle between grains and the mis-misorientation angle are provided. Next, the rotation axis is listed, followed by the grain boundary normal vector that is written in terms of the crystal orientations of the two neighboring grains. For those boundaries which are highly curved, the normal vectors are not listed until an adequately planar interface or faceted structure develops. Continued cycling results in the formation of a Σ27b boundary and additional structural rearrangement of the interfaces. First, the Σ3 boundary reduces its mis-misorientation from 5.5° to 1.89° by the last cycle. Cycling also allowed for an increase in the surface area of the Σ3 interface. The Σ25b, which did not have an ordered boundary plane, shrinks during cycling. The Σ27b forms at the end of cycle 7, but there is little change in mis-misorientation with continued cycling. The most interesting evolution is observed for the Σ11 boundary. This boundary begins to facet during cycling, to reduce the boundary energy at the cost of increased surface area. Facets are denoted in Figure 4-9(b) and (c) using dashed lines. Further inspection of the grain boundary energy and facet structure evolution is shown in Figure 4-9(d)-(f), which is a slightly rotated view of the Σ11 boundary colored by potential energy. Three facets at the end of Cycle 8 are denoted by black arrows and have low relative potential energy, especially at the innermost atomic layer. The facet steps continue to restructure during the next two cycles, resulting in additional length of the low energy segments. Figure 4-9(g) shows the detection of the facet planes as computed by the GTA with character information listed below the image. These low energy planes are Σ11 {113} grain boundary sections, which are known to be a minimum energy cusp for symmetric tilt boundaries [125].

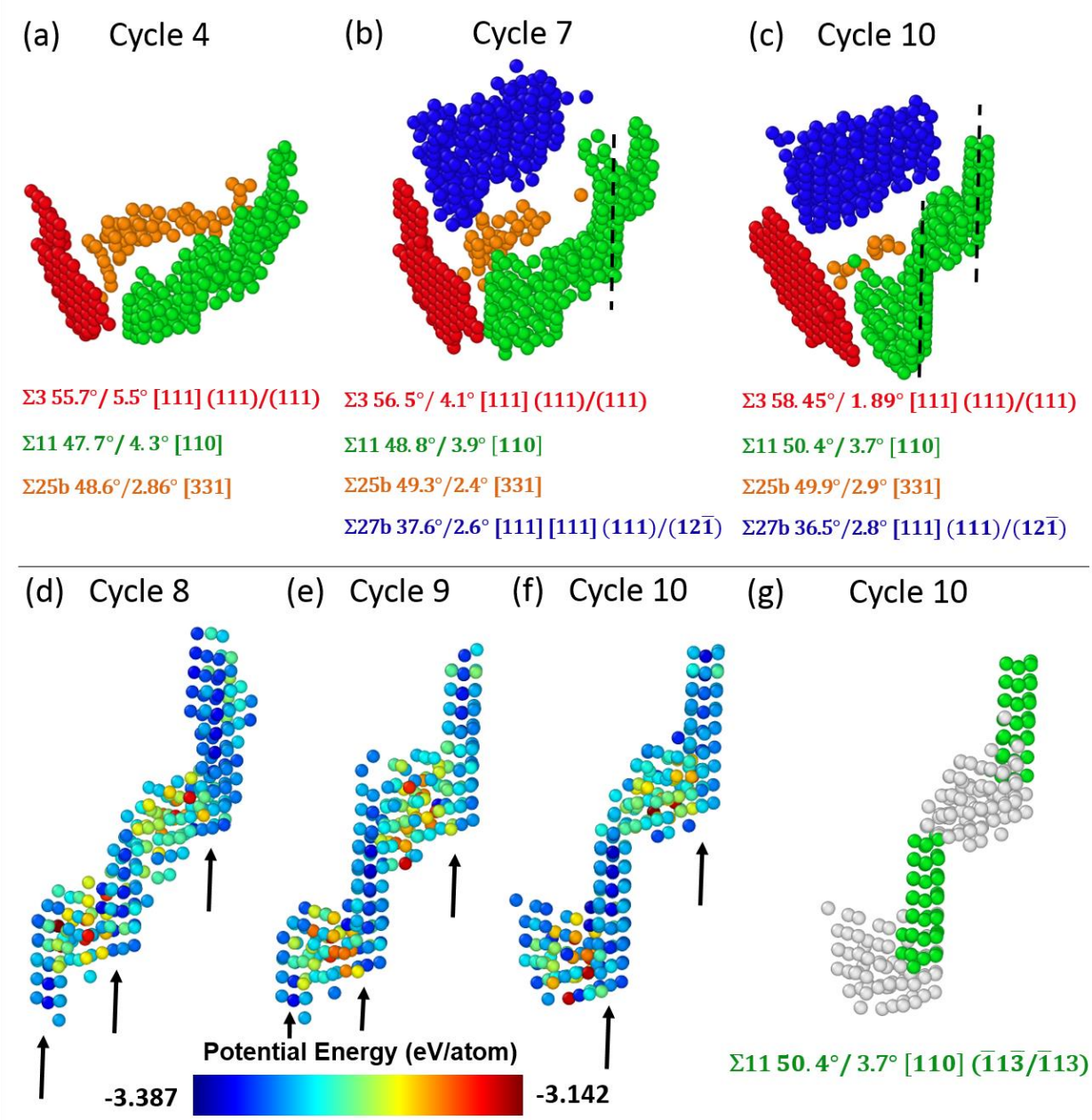

Figure 4-9 **(a)-(c) The formation and evolution of selected special boundaries, with their Σ type, disorientation, mis-misorientation, and boundary plane information listed below each image where applicable, during mechanical cycling of a d = 5 nm sample at 600 K. (d)-(f) Cyclic loading drives a reduction in the energy the Σ11 boundary through grain boundary faceting. (e) The individual facet planes along the Σ11 boundary with low energy are identified as having a {113} boundary plane normal.**

4.4.3 Effect of starting configuration

As some recent studies have questioned whether a Voronoi grain structure is a realistic representation of real polycrystalline microstructure [149-153], it is nature to ask whether the results reported above are general findings or related specifically to the evolution of a Voronoi grain structure. To rule out any artifacts due to any specific sample generation technique, our original Voronoi samples were compared to two additional samples generated from separate three-dimensional isotropic grain growth models developed by Lazar et al. [154] and Syha and Weygand [155], with a focus on cycling of the d = 5 nm structures at 600 K since this was the condition that showed the most evolution. These models allow for different, potentially more realistic, distributions of grain size as well as grain boundary topological features and boundary curvatures that may not be present within an as-assembled Voronoi construction. The Front-Tracking implementation of Lazar et al. [154] is known to reproduce interesting geometrical features such as two-sided faces and three-faced bodies, which occur as the transitioning microstructure coarsens to a steady state. The Vertex Dynamics model of Syha and Weygand [155] includes an additional force term which incorporates the effects of inclination and misorientation dependent grain boundary energy. Both models satisfy the MacPherson-Srolovitz relation for grain growth rates in three dimensions [156]. Lazar et al. [154] and Syha and Weygand [155] developed coarsened microstructures by starting with grains that were initially generated using the Voronoi construction and then grown using their Front-Tracking and Vertex Dynamics algorithms, respectively. In the present study, we have taken the grain and boundary locations from these two studies and filled them with atoms corresponding to randomly oriented crystals using the open source code NanoSCULPT developed by Prakash et al. [157]. The overall sample size was scaled to microstructures that are comparable to our as-assembled d = 5 nm grain size, before then subjecting

both of these samples to the 600 K anneal for 100 ps. These two samples were then cycled at 600 K in order to observe and compare the resulting grain boundary network evolution. For the remainder of this section our three different starting configurations will be referred to as Voronoi, Vertex Dynamics, and Front-Tracking to facilitate comparison between the different sample generation methods.

Visual comparisons of all three starting configurations can be seen in Figure 4-10(a)–(c) which are sliced along a (111) sample plane and color coded according to grain identification by the GTA. The Vertex Dynamics and Front-Tracking samples contain larger numbers of grains, which allows for improved evolution statistics as well as some insight into whether our previous results are affected by the selected sample size. The Vertex Dynamics sample contained 573,690 atoms with a cubic simulation cell measuring 146.5 Å in length and the Front-Tracking sample contained 632,469 atoms with a cubic simulation cell measuring 222.0 Å. The grain size distribution for all three samples is presented in Figure 4-10(d), where there is a clear contrast between the sharp distribution in the Voronoi sample as compared to the broader distributions found within the grain growth models. The exact average grain sizes for all three models after the 600 K anneal were computed to be 5.4 nm, 6.7 nm, and 6.4 nm for the Voronoi, Vertex Dynamics, and Front-Tracking samples, respectively, based on an equivalent spherical diameter calculated from the atomic volume of each GTA identified grain.

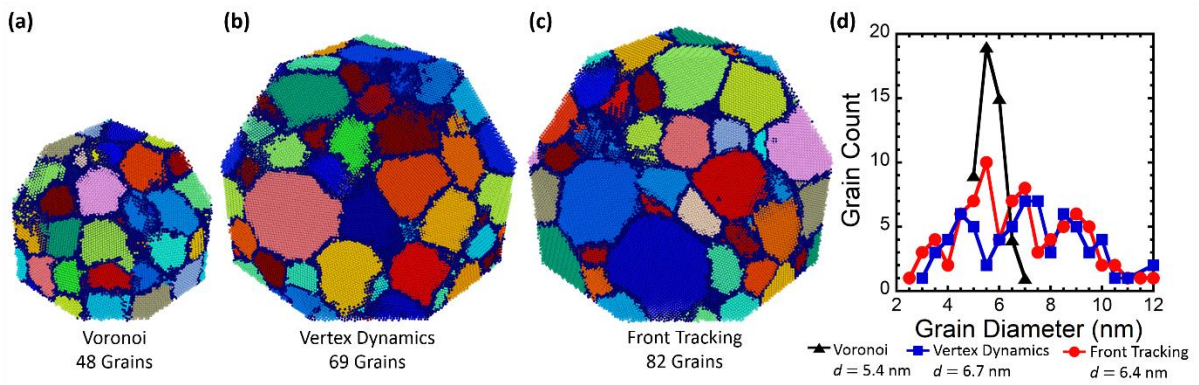

Figure 4-10 (a)-(c) Visual comparison of the three different starting configurations post annealing at 600 K with grains colored according to GTA identification. (d) The grain size distribution for all three samples before cycling was performed showing a much narrower distribution for the Voronoi sample. Calculated average grain size for each sample are also listed below the figure.

Special boundary and Σ3 fraction evolution is shown in Figure 4-11(a) for all three sample generation methods as a function of cycle number. Even with a varying initial distribution of special boundary content there is a consistent increase in special boundary fraction during cycling for all $\Sigma \leq 29$. The Σ3 content evolves slightly faster in the Voronoi samples, which could in part be attributed to the slightly smaller average grain size and an increased contribution from grain rotation. The slight reduction in Σ3 evolution may be connected to the fact that the wider grain size distribution of the Vertex Dynamics and Front Tracking contain a few grains in the 10 nm range, where we previously reported less Σ fraction evolution in Figure 4-7(b). In the end though, significant evolution of both special boundary and Σ3 fractions are observed with cycling, demonstrating that the observations made in this chapter are applicable to a general nanocrystalline grain structure. The complete evolution of each special boundary type is presented in Figure 4-11(b) and (c) for the Vertex Dynamics and Front-Tracking, respectively. An interesting trend across the two new samples is the increase in Σ3 and Σ11 boundary fractions, similar to the Voronoi observations. The three models produce differing initial Σ fractions, meaning that some details of the grain boundary character evolution are different. For example, the Front-Tracking sample has

the largest fraction of Σ5 boundaries. Since these are relatively high energy boundaries and the system evolves to a lower energy state during cycling, the Σ5 fraction rapidly decreases during cycling. As another example, the Vertex Dynamics sample has an increasing Σ13 fraction, while maintaining the relatively large initial fraction of Σ29 and Σ21 boundaries. As a whole though, the comparison of the three different samples allows general conclusions to be drawn. Mechanical cycling at elevated temperature allows the grain structure to rearrange, with an increase in low energy Σ3 and Σ11 fractions in all cases.

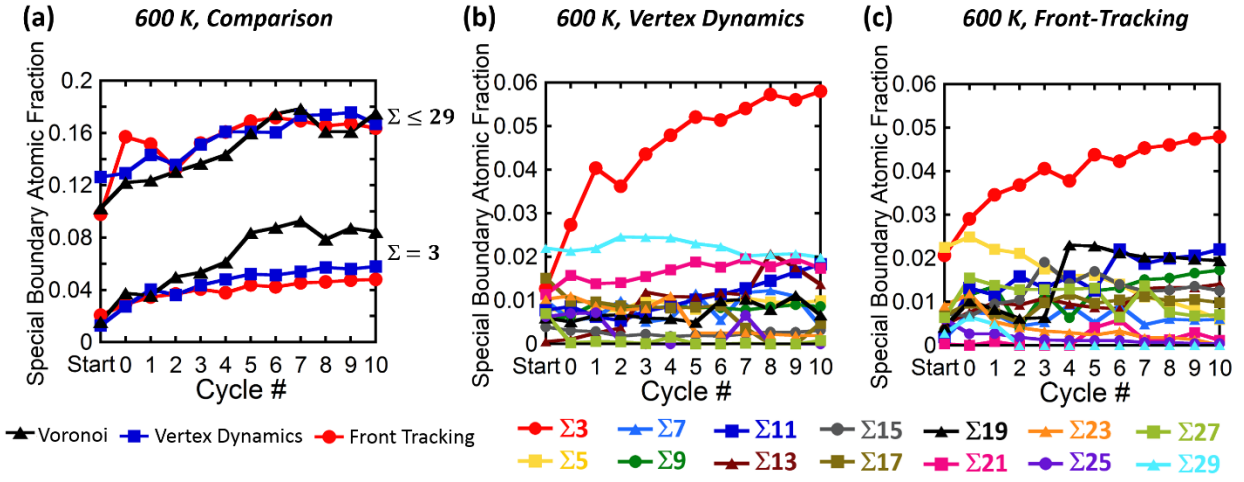

Figure 4-11 (a) The upper curves show the special boundary fraction evolution for all boundaries with Σ ≤ 29 as a function of cycle number. The lower curves compare the difference in Σ3 evolution for all three starting configurations. Detailed evolution of special boundary fraction for all special Σ types is shown as a function of cycle number for the (b) Vertex Dynamics and (c) Front-Tracking samples, respectively.

4.4.4 Comparison with evolution during annealing

The results shown in the prior two sections clearly show that plasticity is capable of restructuring nanocrystalline grain boundary networks so that lower energy configurations can be found. Thermal annealing is another common way to drive microstructural evolution toward a lower energy state, and can serve as a comparison point for the mechanically-induced restructuring already described. To facilitate such a comparison, the d = 5 and 10 nm samples were also subjected to thermal treatments at 800 K. The 600 K equilibration samples were heated in a linear

fashion to 800 K over the course of 100 ps, then held at this temperature for 1 ns with atomistic snapshots analyzed in 100 ps time intervals. The grain boundary special fractions during this annealing are presented in Figure 4-12(a). There was a dramatic increase in special boundary fraction for the 5 nm grain size, but no increase for the d = 10 nm sample. An in-depth analysis of boundary evolution in the 5 nm sample is shown in Figure 4-12(b). Most noticeable is the rapid increase in Σ3 boundary fraction during annealing. After reaching 800 K (0 ps), partial dislocation emission along successive {111} planes allows for pre-existing stacking faults to form into small annealing twins. These twinned regions remain fixed as the remaining grain boundaries within the sample migrate rapidly in directions parallel to the {111} planes, to lengthen the coherent twin interfaces. The majority of the Σ3 content was observed to develop in this manner with minor evolution occurring to the preexisting non-coherent Σ3 boundaries, the majority of which disappeared from the microstructure soon after heating. Bringa et al. [158] discovered five-fold twinning in simulated Cu (d = 5 nm) annealed at 800 K, explaining that high local stresses within the grain boundaries combined with elevated temperature can allow for emission of twinning partials during annealing. Although lengthening of Σ3 boundaries dominates network evolution during annealing, some small increase to the Σ5, Σ7, and Σ11 population also occurs. Unlike the mechanical loading case where Σ11 boundaries are the second most frequent special boundary, Σ5 content increases most quickly during annealing. However, after ~500 ps the average grain size becomes very coarse and several grains approach the length of our simulation cell.

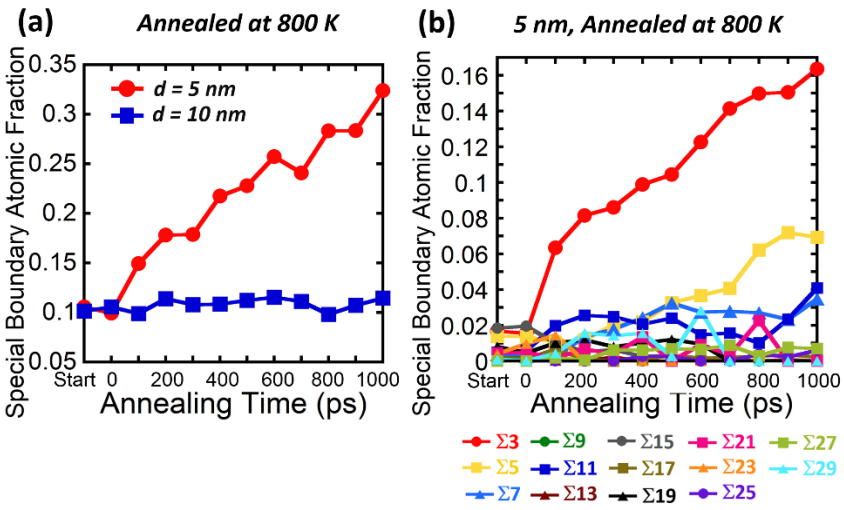

Figure 4-12 (a) Special boundary fraction for both grain sizes as a function of annealing time at 800 K. (b) A detailed breakdown of each special Σ type for the d = 5 nm sample, showing that Σ3 boundaries exhibit the fastest increase while Σ5, Σ7, and Σ11 interfaces also become more common.

In order to show the typical physics of network restructuring during annealing, a representative example of Σ3 boundary lengthening is shown in Figure 4-13(a)-(c). As the annealing simulation begins, the highly curved, random boundaries start to migrate toward their centers of curvature (black arrows). This migration allows a coherent (111) interface to increase its length dramatically and obvious grain growth has occurred by 200 ps. Further inspection shows that this is not the only special boundary which formed along this grain pair during the annealing process. Figure 4-13(d) presents a side view showing the formation of a second twin boundary and a Σ7 boundary. A facet step present in Twin 1 is also observed. Additional annealing allowed for the continued migration of adjacent random boundary segments, which lengthens the Σ3 boundaries and Σ7 boundary until they meet and lock in position at 500 ps, as shown in Figure 4-13(e). The Σ7 boundary obtains a distinct (111) orientation normal by this time, which is a minimum energy configuration for the Σ7 boundary type [125]. Network rearrangement during annealing therefore leads to different special boundaries (Σ5 and Σ7 are common) and different mechanisms of evolution (curvature-driven grain growth).

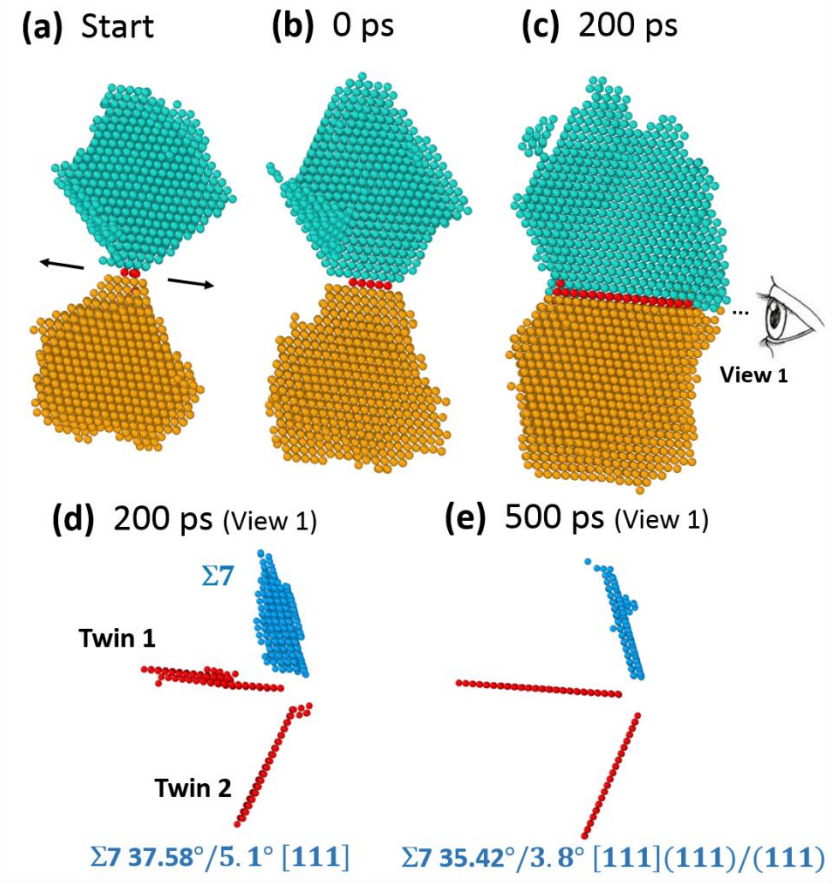

Figure 4-13 (a)-(c) Curvature-driven grain boundary migration leads to Σ3 boundary lengthening in the d = 5 nm sample during annealing. Additional evidence of grain boundary facet removal is shown in (d) and (f), where a well-defined (111) plane forms along the Σ7 boundary after 500 ps of annealing.

4.5 Conclusions

In this work, a quantitative analysis of the grain boundary network and its evolution during monotonic and cyclic plastic deformation was presented. Since experimental techniques lack the temporal and spatial resolution for such measurements, molecular dynamics were used to simulate deformation while new analytical tools are created to quantify important grain boundary features. By investigating two grain sizes that span the Hall-Petch breakdown, we find that finer nanocrystalline grain sizes experience more evolution of their grain boundary network during

plasticity. In addition, the magnitude of network restructuring is highly temperature dependent. Several important conclusions can be drawn from this work:

- Analysis tools were developed that allow for quantification of the grain boundary network in atomistic models. The five degrees of freedom associated with any grain boundary section can be measured, as well as features associated with triple junctions and vertex points. With this information, grain boundary character distributions and network topology/connectivity can be characterized with nanometer and femtosecond resolution.
- Both monotonic and cyclic plasticity drive an increase in the special boundary fraction for d = 5 nm. The majority of the increase was associated with higher Σ3 and Σ11 boundary fractions, through both the lengthening of existing boundaries and the creation of new boundary sections. For the Σ3 boundaries specifically, mis-misorientation decreases during cycling and low-energy (111) boundary planes are often found. Similar faceting to create low-energy Σ11 interfaces is also observed. The preference for these low-energy grain boundary types suggests that the grain structure is rearranging to reduce system energy and find a more stable configuration.
- Negligible restructuring was found for the d = 10 nm sample. This lack of evolution can be linked to the reduced activation of collective plastic mechanisms such as grain rotation and the increase in dislocation activity.
- Despite varying the starting microstructure, which also alters the initial distribution of special boundary content, a consistent increase in $\Sigma \leq 29$ evolves during mechanical cycling at elevated temperature. The formation of low energy Σ3 and Σ11 boundaries is common to all samples.

- Annealing also leads to a reduction in system energy, but there are important differences in the special boundary types which form and in the mechanisms for formation. Σ3 boundaries lengthen by curvature-driven grain growth, where fast migration of random boundaries parallel to the (111) twin planes drastically increases Σ3 content.

This study shows that the collective deformation physics associated with nanocrystalline metals can lead to evolution and restructuring of the grain boundary network. Grain boundary networks are therefore very dynamic at the finest nanoscale grain sizes and grain boundary engineering through new mechanisms is an intriguing possibility for these materials.

CHAPTER 5. Wear Induced Microstructural Evolution of Nanocrystalline Ni-W

5.1 Introduction

Having learned in the previous chapters that smaller grain sizes and increased cycling leads to elevated evolution, we then attempt to use these insights to guide an experimental validation of our simulation results. Since nanocrystalline metals are known to exhibit high strength [4, 5] and fatigue resistance [6, 7], their usage lends promise to applications involving improved wear resistance. Additionally, abrasive wear is essentially one of the more rigorous methods by which we can induce structural evolution through repetitive stress application. It is for these reasons that we choose to track microstructural evolution in extremely fine nanocrystalline grains using wear as the driver for plasticity.

Analysis of nanocrystalline wear response can be found in previous literature, with a number of works analyzing the tribology of nanocrystalline materials [9, 159-162]. However, tribology is mainly concerned with friction and wear behavior, linking mechanical properties to wear resistance without understanding the near-surface microstructural changes taking place in these materials during surface contact. Due to the complex nature by which nanocrystalline materials deform, resolving this issue will lead to significant understanding of the dynamic nature of nanocrystalline microstructures during wear.

Unlike ultrafine nanocrystalline materials, the study of wear-induced microstructural evolution in microcrystalline materials is well documented, with concrete evidence of the formation of cellular dislocation sub-structures [163, 164] and nanocrystalline tribolayers [165-171]. Because nanocrystalline metals are known to deform through unique grain boundary

mediated mechanisms instead of dislocation dominated processes, their sub-surface microstructures could in fact evolve in manners completely different to their coarse-grained counterparts. Fortunately, new research is surfacing, however limited, in regards to the direct probing of worn surface microstructures which initially contain nanocrystalline grains. For example, Hanlon et al. [172] discovered a coarsened grain structure of nanocrystalline Ni (d = 30 nm) after performing post-wear focused ion beam (FIB) image analysis of the scratch surface. Qi et al. also observed coarsening as well as structural elongation and texturing in Ni with a 10-12 nm grain size [173]. Layered substructures have also been discovered beneath nanocrystalline wear surfaces. Prasad et al. [174] were able to confirm the formation of a nanocrystalline surface layer atop a coarsened microstructure when wear tests exhibited low steady-state friction coefficients on Ni films with grains ranging 20-100 nm in size. Padilla et al. [175] extrapolated upon this finding and discovered that the permanence of the topmost nanocrystalline tribolayer is dependent on the friction coefficient which will dictate micro-cracking and delamination of the layer.

Unfortunately, the majority of these studies exclude the analysis of average grain sizes which approach the amorphous limit, where grain boundary mediated deformation physics should dominate plasticity. A systematic study by Rupert et al. [98] analyzed Ni-W films of grain sizes varying from 3 – 47 nm to understand sliding wear as it pertains to the Hall-Petch breakdown. They discovered discrepancies in Archard scaling law which can be explained by the novel deformation and strengthening mechanisms inherent to ultra-fine nanocrystalline materials. Their pin-on-disk experiments of d =3 nm Ni-W resulted in post-deformed surface structures containing a well-defined layer of grain growth while the tests involving larger starting grain sizes revealed little to no surface structure evolution. Argibay et al. [176] analyzed similar Ni-W coatings with

a grain size of ~5.2 nm and suggested the thickness and average grain size within the layer is a function of applied stress and correlated to the friction behavior. These studies clearly highlight the fact that it is essentially the dynamic deformation behaviors of ultra-fine nanocrystalline materials which allow for the formation of these growth layers; however, insight into the specific nature of how these layers develop is still not fully understood since microstructural characterization was only performed pre and post deformation.

In this chapter, we analyze grain structure evolution of Ni-W with an extremely small starting grain size (d = 2.3 nm) during abrasive wear using the nanoscratch method. A relatively low contact load and sliding speed are defined in order to analyze the development of the subsurface microstructural evolution which results as the material undergoes repeated cyclic stress from the scratch experiment. Wear volume evolution is tracked and the resulting trends are used to dictate cycling levels which may be of particular interest for microstructural characterization through the use of TEM. Due to the micrometer sized geometry of the nanoscratch test, the full wear track is able to be incorporated into our TEM samples, providing further insight into the evolution process of the near-surface tribolayer. Finally, we are able to find synergy between the evolution that is occurring below the indenter tip and that which we observed in our earlier investigations involving simulated cyclic plasticity.

5.2 Methods

A nanocrystalline Ni-W alloy was deposited using the pulsed electrodeposition technique developed by Detor and Schuh [177] atop a Ni 200 99% pure substrate which was mechanically polished to below 1 um using diamond suspension. After deposition, the surface was again polished to below 1 um in order to achieve a smooth and level wear surface. X-ray diffraction

(XRD) analysis of the final film was performed inside of a Rigaku SmartLab X-Ray diffractometer with a Cu Kα radiation source operated at 40 kV and 44 mA . The resulting film contained an XRD verified average grain size of d = 2.3 nm obtained using the Scherrer equation and corrected for instrumental broadening of the (111) peak. The subsurface average grain size was also verified extensively using Transmission Electron Microscopy (TEM).

Nanoscratch testing of the films was performed using an Agilent G200 Nano Indenter fitted with a 60 degree diamond conical tip with a 5 μm radius, essentially exhibiting the geometry of a round end cone. Wear scars were induced through multi-cycle wear tests with scar trench profiling performed periodically in order to track tribological evolution of material wear. Figure 5-1(a) illustrates the process of a 1000 cycle wear experiment with the probe starting location on the left side of the wear scar. Each wear cycle involves a constant load of 10 mN while traversing the surface of the material in both the pass and return directions. Repeating this process (both pass and return) for 10 cycles is denoted as a wear set. Between wear sets, the wear probe performs a cross-profile of the scratch trench by performing a profiling pass perpendicular to the direction of the wear scar at a much lighter load. The profiling track in Figure 5-1(a) is indicated by the vertical line that passes through the wear track. For the purposes of illustration, the profiling load in the test shown was increased to improve visibility. For the remainder of this study, however, the profiling load was 0.05 μN. This load attempts to minimize any additional deformation of the track which may take place due to the repetitive profiling between wear sets. 0.05 μN was deemed a minimum allowable profiling load since it nearly maximizes the capabilities of the G200 system while also providing reliable profiling data. After the cross-profile, the scratch probe then returns to the beginning of the wear scar to perform an additional wear set. For the scar illustrated in Figure 5-1(a) 100 wear sets were carried out, resulting in 1000

total cycles. Scanning electron microscopy (SEM) was used to provide insight into the surface morphology of the wear tracks by visually inspecting the wear scars.

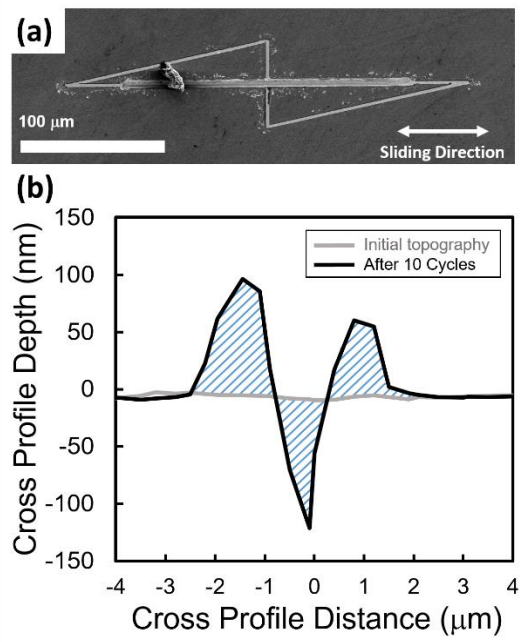

Figure 5-1 (a) 1000 cycle scratch test which illustrates the mechanics of a wear test experiment. (b) Calculation of the wear area which is the integral of both the pileup and removed material above and below the initial film surface.

Because trench profiling is performed at regular intervals during the experiment, material removal and pileup morphology is able to be tracked as a function of cycle number. Figure 5-1(b) shows the two-dimensional cross section of a wear track after only 10 cycles. Total wear volume can then be determined by integrating the area both below and above the initial surface topography and then multiply this area by the length of the scratch. Integration of the worn area in the two-dimensional cross profile is illustrated in Figure 5-1(b) by the blue hatched area above and below the un-deformed film surface. Any emerging trends in the evolution of worn material volume were used to influence future testing and pinpoint areas of interest regarding subsurface microstructural evolution. Future wear tests can then be truncated after certain cycle numbers so that TEM lamella from the wear track can be extracted and imaged. FIB lift-out technique [178]

combined with transmission electron microscopy was extensively relied on for characterizing near-surface microstructural evolution below the wear track during the different stages of wear evolution. The sample surface was protected from the high energy ion beam using platinum before initial thinning and lift-out was performed. The initial Pt layer is illustrated in Figure 5-2(a) atop the wear track, and the TEM sample pre lift-out is shown in Figure 5-2(b) attached to the OmniProbe nanomanipulator. Samples were mounted at the top of V-shaped TEM posts in order to help prevent bending or snapping which can occur when the samples are thinned to 50 nm or below. During the sample thinning the current of the Ga ion beam was iteratively decreased to a final setting $\leq$ 5 kV which ensures removal of the damage layer left by the earlier steps in the sample thinning process. A mounted TEM specimen which is midway through the thinning procedure can be seen in Figure 5-2(c) with the cross-profile topography of the wear trench clearly visible below the semi-translucent protective platinum layer.

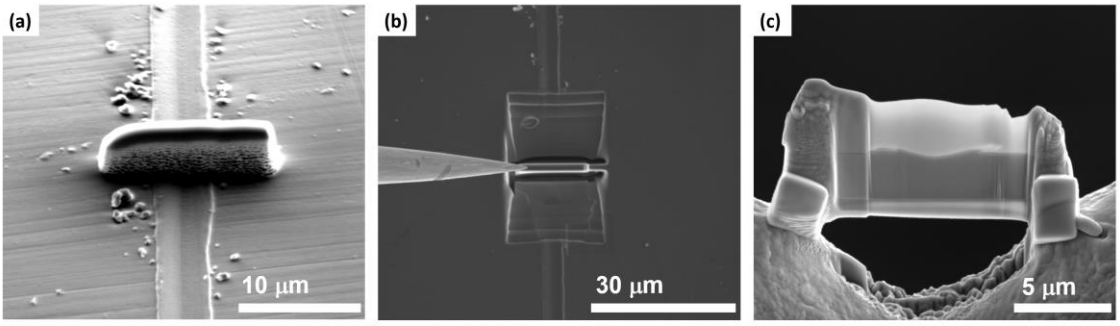

Figure 5-2 (a) Wear scar with platinum deposited to protect the cross-sectional area of interest from FIB induced damage. (b) Lift out technique to remove the lamella from the wear track. (c) Cross-sectional TEM lamella midway through the FIB thinning process with the topography of the wear trench visible below the platinum layer.

5.3 Results and Discussion

5.3.1 Nanoscratch Testing

To begin, multi-cycle nanoscratch tests were performed which consisted of 1000 wear cycles with trench cross-profiling performed every 10 cycles. Figure 5-3 displays the cross-profiles which were measured for a single 1000 cycle experiment. The profiles have been colored from blue to red using a jet color scheme in order to observe the topographical evolution of the trench profile. The y-axis has been adjusted to scale to nanometers in order to more clearly observe the pileup evolution, which distorts the true scratch geometry since in reality the scratch tip is actually quite blunt with a radius of ~5 μm. It is initially apparent that the first few wear sets act to quickly displace material before any steady state material displacement rate is achieved. Near the end of the test there seems to be a very slight decrease in the overall height of the pileup regions which is most likely attributed to the removal of material from the sides of the trench, a phenomenon which is discussed in more detail in the next section. The non-symmety associated with the pileup heights was systematic throughout our experiments and we attribute this to several factors including the plowing mechanics of the probe, difficulties in insuring a uniformly level sample, as well imperfections in tip geometry. Additionally, even with a low profiling load of 0.05 μN, there is still some unavoidable wear which will take place during the cross-profiling segments of the test, especially after performing a maximum of 100 profiles. It is noted that this post-deformed surface geometry is representative of all five 1000 cycle tests.

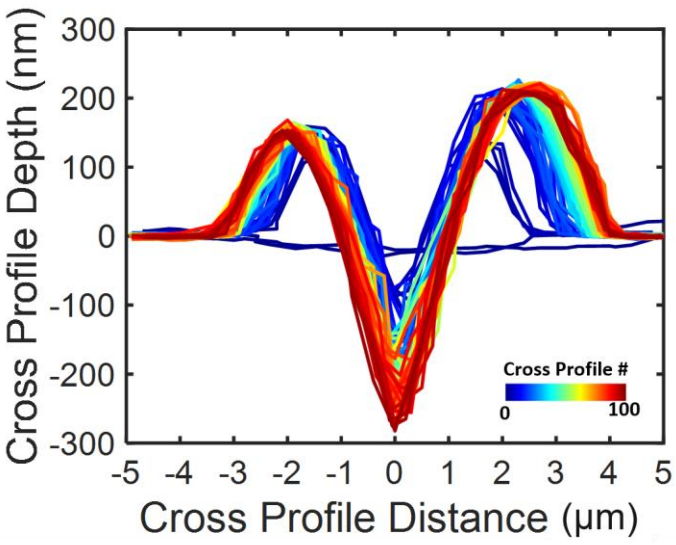

Figure 5-3 Cross profiles for a typical 1000 cycle scratch experiment illustrating the topographical evolution of the surface as a function of wear set.

The volume of material displaced between each wear set was integrated and tracked and the results are shown in Figure 5-4(a). Since it seems that the wear removal rates change during the course of the test, an averaging of the tests was conducted for a clearer analysis of any potential wear regimes that may unfold during the nanoscratch experiment. Figure 5-4(b) is an average of all five tests with the data broken up into three possible wear regimes which have been colored accordingly and subsequently approximated using linear regressions of the data in each segment. The equations for each of the trend lines is also displayed next to each data segment. During the beginning of the test, the wear removal rate is high as indicated by the steep slope of the red trend line. The rate then sharply decreases by an order of magnitude after about 20 cycles and then another order by approximately 200 cycles as indicated by the blue and green regressions, respectively. In order to uncover any connections between these wear regimes and the underlying microstructural evolution that takes place below the scratch tip, future scratch experiments were stopped at cycle numbers slightly past the shifts in the wear evolution trends of Figure 5-4(b) in

order to characterize the microstructure at these points of interest. FIB prepared TEM lamella were made perpendicular to the scratch direction for experiments containing 1, 30, 250, and 1000 cycles as indicated by the gold stars in Figure 5-4(b)

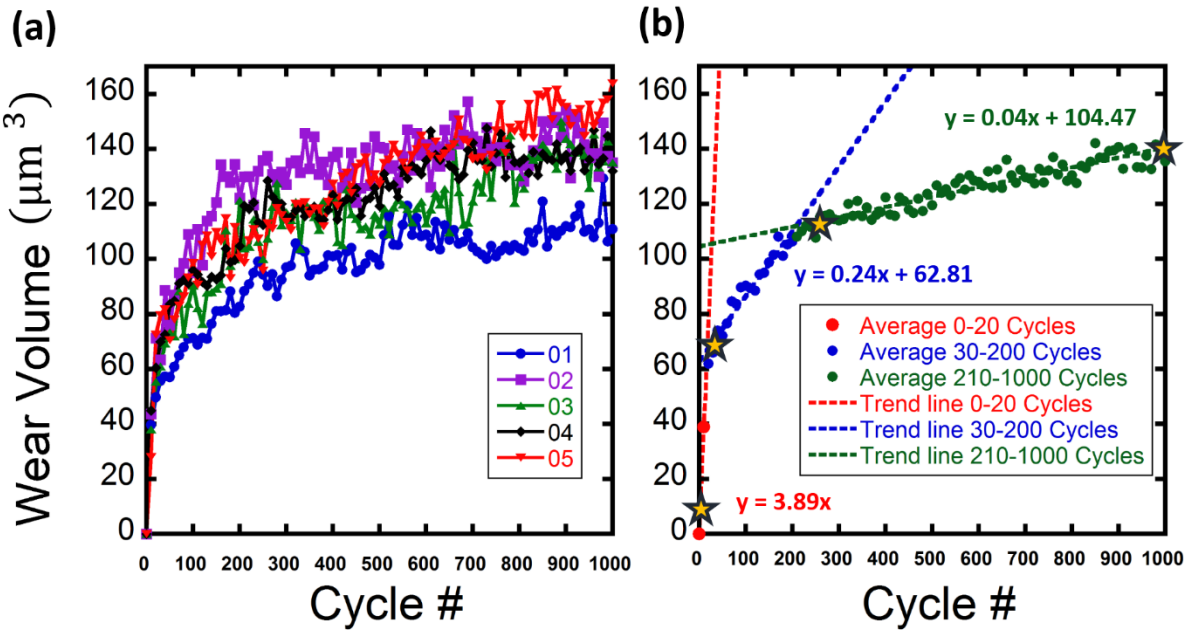

Figure 5-4 (a) Wear volume evolution as a function of cycle number for five separate 1000 cycle scratch experiments. (b) Average of the 5 tests with linear regressions fit to the three different regimes which take place during the deformation process.

5.3.2 Wear Scar Surface Morphology

Before characterizing the subsurface microstructure, the surface morphology of the wear scars was analyzed using SEM for evidence of the wear mechanisms taking place during the nanoscratch experiments. Figure 5-5(a)–(d) displays the morphology of 1, 30, 250, and 1000 cycle wear tests, respectively. In Figure 5-5(a) the inset image is a magnified view of the upper half of the trench and points out several locations of flow localization which is caused by inhomogeneous plasticity at the base of the pileup during the single scratch cycle, a phenomenon which is common for this nanocrystalline Ni-W system [104, 179]. This localized plasticity allows for the material displacement necessary in order for the surface to match geometry with the probe tip. Another

important observation is that there is no evidence of debris, meaning all of the worn volume is conserved as it is displaced during the initial plowing by the conical tip. Schuh et al. [180]. suggest that such a blunt tip geometry should impose high hydrostatic pressures on the surface and also reported no evidence of debris for their single cycle scratch experiments which ramped the tip load from 0 – 10 mN. Similar to the smooth trench resulting after 1 cycle, the 30 cycle trench of Figure 5-5(b) also shows a smooth surface, albeit with a wider wear scar and no visible flow localization at the edges of the track. There is also no identifiable wear debris present anywhere near this wear scar.

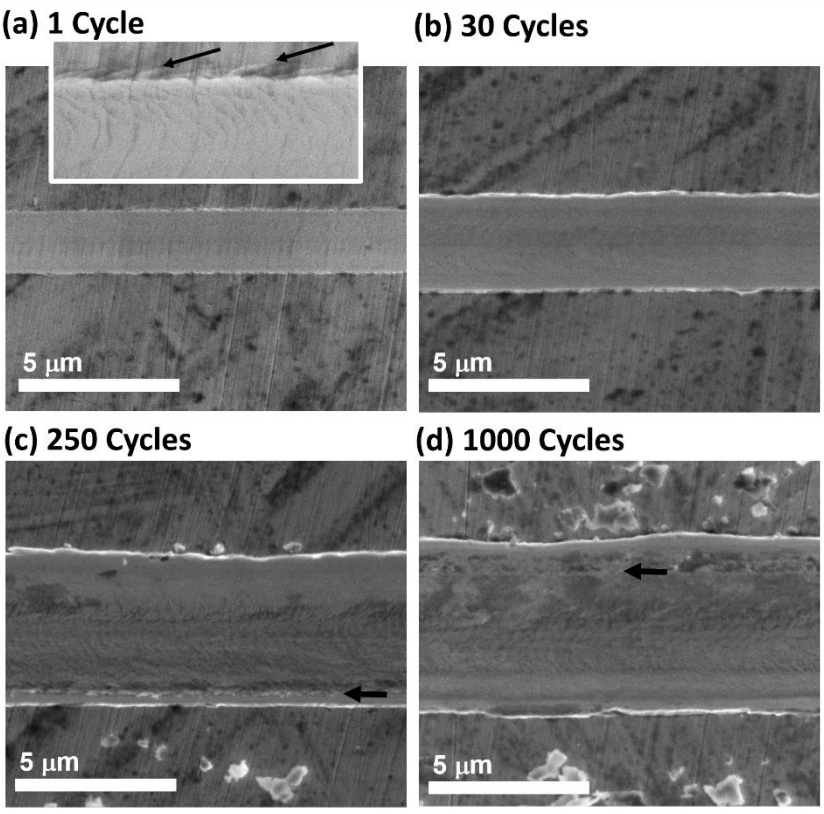

Figure 5-5 Scratch trench morphology after (a) 1 cycle, (b) 30 cycles, (c) 250 cycles, and (d) 1000 cycles

Figure 5-5(c) and (d) show a morphology which is visibly different than that in either the 1 or 30 cycle images. While the center of the track is still relatively smooth, there does seem to

be visible surface texture which has developed toward the outside of the wear scar. There is also evidence of an additional pileup layer in Figure 5-5(c) and (d) as indicated by the black arrows, with surface texture visible at specific locations where this layer seems to have been removed by the probe. Additionally, there is no apparent evidence which suggest cutting or chipping due to surface asperities and no visibly identifiable buildup of a transfer layer which is likely due to the mechanics of our back-and forth scratch method. Wear debris, however, is clearly visible outside of the wear track for these more rigorous wear experiments. It is interesting to note that wear debris is only observed for the 250 and 1000 cycle tests which indicates that perhaps our wear volume measurements are not conservative at these higher levels of deformation. Including this material in our integrated wear volume calculations would thus alter the trend line of our data for the green regime in Figure 5-4(b), if our method was able to include this debris material. Since the purpose of this study concerns microstructural evolution during wear, we are mainly interested in the worn material, or that materials which has undergone plastic deformation without fracture from the surface. We also make note that the trend lines in Figure 5-4(b) are not intended to be strict models of the wear volume behavior in this material, but rather are displayed in order to help emphasize the changes in magnitude of the wear rate during cycling. That being said, material removal may be influenced by the underlying microstructural evolution taking place beneath the probe. Evolution of the grain structure during wear will be discussed in the following section.

5.3.3 Subsurface Grain Structure Evolution

Cross sectional TEM lamella cut perpendicular to the scratch direction were extracted from tests containing 1, 30, 250, and 1000 cycles and the results are displayed in Figure 5-6. Figure 5-6 shows the results of the TEM analysis which captures the grain structure evolution surrounding the scratch tip as it develops during cycling. This image shows the entire scratch width of a 1

cycle experiment with both pileups visible at the corners of the image. A selected area electron diffraction (SAED) pattern identifies the nanocrystalline structure below the scratch tip as solid rings. The grain structure below the wear surface is found to be relatively unchanged from that of the as-deposited microstructure other than a few slightly enlarged grains which appear right at the surface as indicated by the white arrows in Figure 5-6(b). As the number of cycles is increased to 30, significantly more grain structural evolution is observed as is shown in Figure 5-6(c). While it is obvious that grain growth has occurred, it is also interesting to note that there is a gradient in the average grain size which changes as a function of both depth and distance from the center of the scratch tip. The magnified image in (d) more clearly shows this gradient as it progresses away from the surface.

Rupert et al. [98] concluded that stresses during wear should be the highest just beneath a traversing spherical probe through their use of the explicit equations of Hamilton [181]. Even though these equations assume perfectly spherical probe, our geometry is not much different considering our conical scratch tip which is applied at fairly shallow indentation depths. Additionally, it is known that nanocrystalline materials can coarsen through stress driven grain boundary migration [23, 182, 183] and that such migration results in discontinuous grain growth [80]. Recent molecular dynamics simulations by Panzarino et al. [146] also verify that grain rotation and coalescence can contribute to discontinuous grain growth during cyclic stressing and that the magnitude of such plasticity is proportional to the number of applied cycles. It is logical then that this gradient structure has developed since the subsurface stresses should decrease with depth.

Analysis of the 250 cycle sample shows that the gradient has essentially disappeared by this point and the evolution layer has saturated to a well-defined state shown in Figure 5-6(e) and

(f). This layer extends 270 nm deep when measured at the center of the conical scratch tip. An SAED pattern taken from within the evolved region shows no clearly defined texture development and any bright spots are likely due to the diffraction of a few large grains when considering the limited number of grains present in this area where considerable grain growth has occurred. The white arrow in Figure 5-6(e) shows where additional pileup of material has begun to separate from the bulk surface which aligns with our previous observations of debris removal for the tests consisting of 250 or more cycles. As the number of cycles is increased to 1000 (Figure 5-6(g) and (h)) the subsurface microstructure seems relatively similar to that which was observed after 250. The evolution depth below the tip apex was measured to be 304 nm which isn't drastically larger than what was measured before and the overall shape of the layer is geometrically similar. The SAED pattern also indicates a polycrystalline material exhibiting no preferential texture and Figure 5-6(h) shows a grain structure which is visibly similar to that in image (f). Evidence that the grain growth is discontinuous or abnormal can be seen as small grains characteristic of the as-deposited sample which remain in the microstructures of both the 250 and 1000 cycle tests. Regarding material removal during the elevated tests, the white arrow in image (g) points out an area where a second pileup region has formed and is experiencing some removal from the bulk surface.

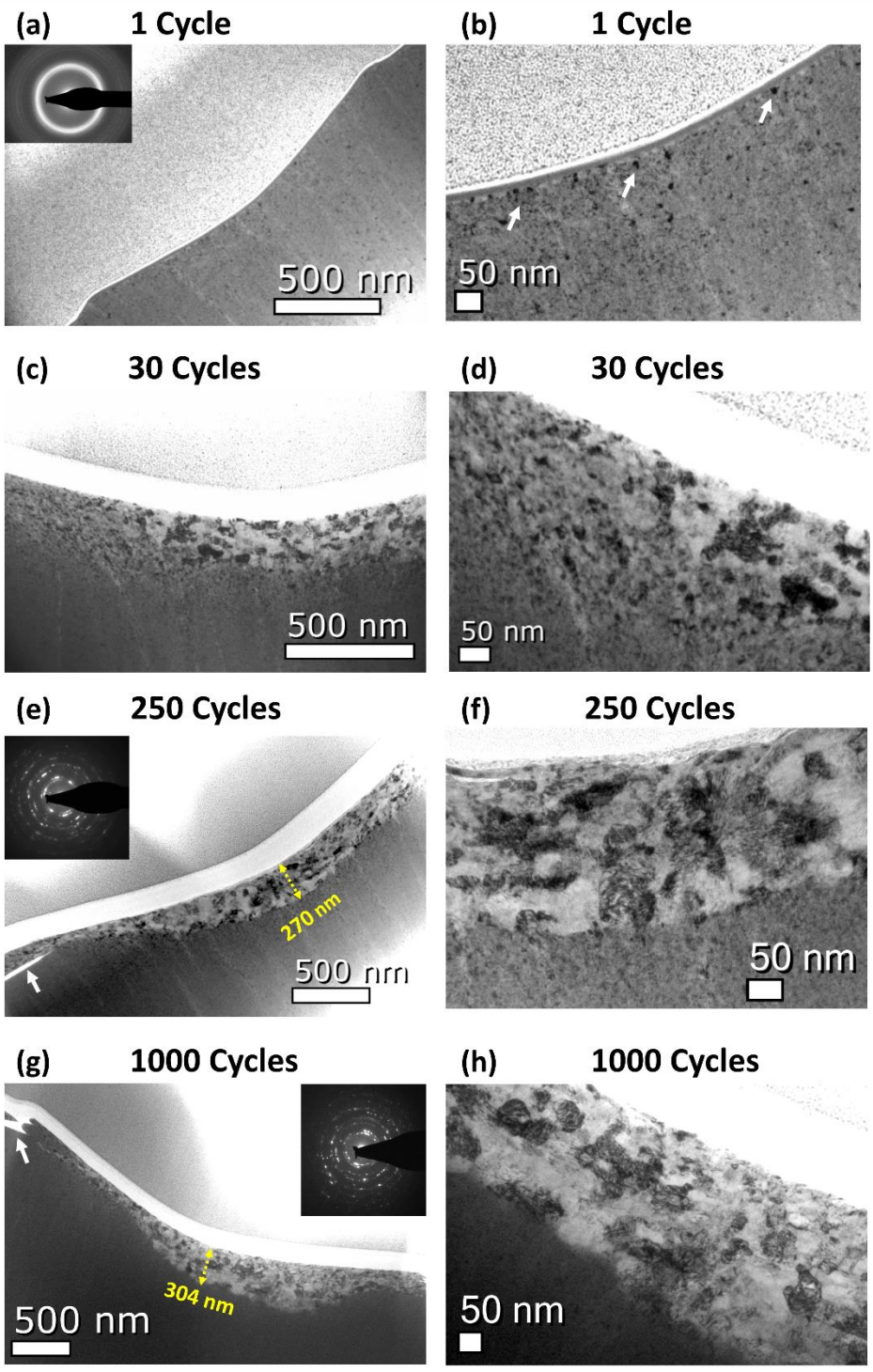

Figure 5-6 Results of the TEM analysis of near-surface microstructural evolution after 1 cycle, 30 cycles, 250 cycles, and 1000 cycles. (a), (c), (e), and (g) show the overall evolution surrounding the scratch tip, while (b), (d), (f), and (h) are magnified images of the microstructure near the center of the trench.

Most important is the fact that these three stages of plasticity: material displacement and conformity to the scratch tip, grain structure evolution, and final saturation to a larger average grain size, seem to correlate with the three wear regimes highlighted in Figure 5-4(b). The fact that the growth layer evolved from a gradient structure can be explained through the analysis of the gradient in stress which also extends down from the surface below the indenter. The magnitude of grain boundary plasticity which takes place should be proportional to the stress level experienced by each region of material. The fact that the layer eventually saturates to a defined layer of grain growth can be attributed to the repeated cyclic stress which will eventually evolve the deeper material, albeit with the help of additional cycling. Grain structure and the accompanying grain boundary network has been shown to continuously evolve during cycling by Panzarino et al. [146, 184] for various nanocrystalline starting configurations containing average grain sizes less than ~7 nm.

Additionally, Panzarino et al.[184] have shown that the grain boundary mediated modes of deformation are only active below a certain grain size threshold when analyzing both d = 5 and 10 nm average grain sizes subject to cyclic loading. Even if the exact transition grainsize does not correlate one-to-one between atomistic and experimental analyses, we suggest that we are indeed observing the crossover in deformation mechanisms which emerges in this case as a saturation point in grain growth. Due to the mechanics of our test and the plowing mechanism by which abrasion is occurring without significant material removal, the subsurface is essentially being subject to cyclic stress which is repeated with each passing of the indenter probe. Once the grain size reaches the threshold for grain boundary mediated mechanisms, the stress assisted grain growth shuts off and the emergence of dislocation plasticity begins to dominate.

Regarding wear response of the Ni-W film, it is interesting to observe the consecutive decreases in wear rate (Figure 5-4(b)), during grain growth since traditional Archard scaling considers volume removal to be inversely related to hardness. Although grain growth is occurring below the tip, we attribute this increased wear resistance to grain boundary relaxation hardening which has been previously shown to significantly alter the strength properties of as-deposited nanocrystalline materials. Additionally, our previous research on nanocrystalline Al also showed that strengthening can occur during cyclic deformation as a result of the formation of lower energy boundary configurations and overall grain boundary state. Relaxation hardening can be used to explain the increase in strength despite the increase in average grain size of the tribolayer.

As a final note, although it is clear that these main evolutionary events are largely taking place in stages, evidence these processes are ongoing throughout wear deformation is apparent when looking at the near surface microstructure below the edges of the scratch trench. For example, even though the evolved layer is well defined near the center of the trench for the 250 and 1000 cycle samples, there is still the formation of a gradient near the edges of the wear scar which can be seen in Figure 5-7(a) and (b). Evidence of the evolving gradient near the edges is logical since material removal will require a re-matching of the trench geometry with the scratch tip geometry which means that the material near the edges has essentially been subjected to a smaller number of cycles. Another interesting observation uncovered during TEM analysis can be seen in Figure 5-7(b) which indicates an area where flow localization has occurred which has allowed for the displacement of the pileup material. Inhomogeneous plasticity which is evidenced by the curved line of localized grain growth is pointed out by the black arrow in image (b). Khalajhedayati and Rupert [179] observed similar shear bands in the pileup of nanocrystalline Ni-W during nanoindentation.

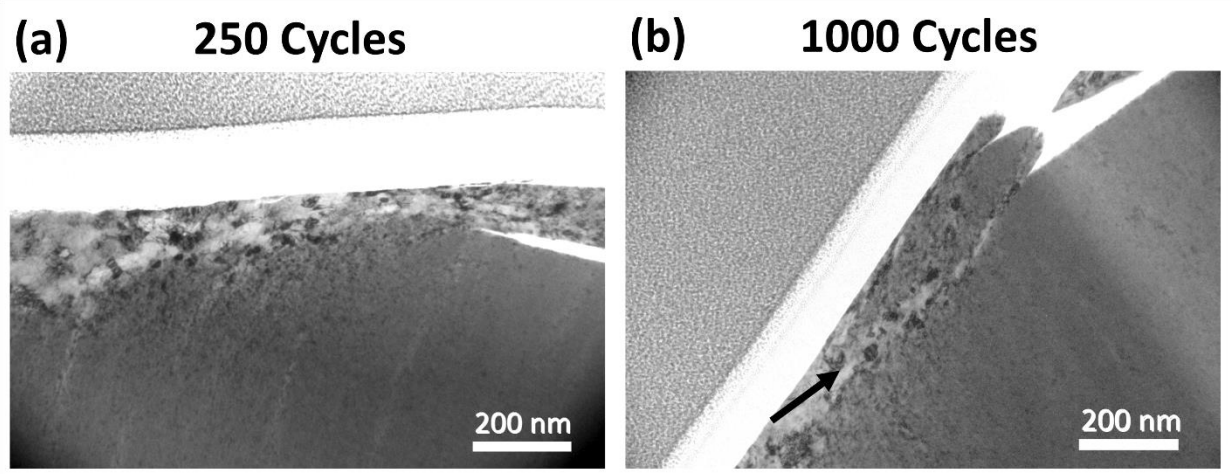

Figure 5-7. Near-surface microstructural evolution at the trench edge for (a) 250 cycles and (b) 1000 cycles illustrating the development of the grain growth gradient even at higher cycling levels. Pileup removal can be seen in both images as well a flow localization in the form of a shear band in image (b).

5.4 Conclusions

In this work, a systematic analysis of grain structure evolution during nanocrystalline wear was carried out on Ni-W with an average grain size of 2.3 nm. Nanoscratch experiments were performed which utilized a rounded canonical tip and applied repeated back-and-forth wear tests from 1 – 1000 cycles while tracking the volume of worn material at regular 10 cycle intervals. After analyzing in detail the wear volume evolution, key cycling levels of interest were pinpointed and then carried out in subsequent tests, allowing for the creation of FIB prepared TEM samples which provided insight and connections between wear volume accumulation rates and underlying microstructural evolution. The following conclusions can be drawn from this study:

- The relatively blunt scratch tip used in this analysis results in plowing-type abrasion which allows for the evolution of a grain growth layer below the scratch surface. This growth layer evolves through grain boundary mediated plasticity mechanisms which are known to be active for ultra-fine nanocrystalline grain sizes.

- Once the onset of plasticity occurs, a gradient structure develops through grain boundary mediated plasticity which results in grain growth with larger grains near the surface and a gradual transition to the bulk material below. This gradient correlates with the expected stress field below the surface.
- Continued cycling allows for a repeated stress state which evolves the deeper material to a saturation grain size that results in a clearly defined layer thickness and the disappearance of the growth gradient. This saturation in grain growth is attributed to the shut-off of nanocrystalline grain boundary plasticity mechanisms.
- Once dislocation plasticity begins governing the subsurface growth layer, material removal begins to occur and wear debris results. Since the thickness of the evolved layer increases slightly between the 250 and 1000 cycle experiments, this suggests that the rate of material removal is slower than the rate at which this growth layer develops for the testing parameters chosen in this experiment.

This study verifies that nanocrystalline microstructures act collectively to alter grain structure during cycling stresses imposed through nanocrystalline wear. By starting with an average grain size near the amorphous limit, we can verify that nanocrystalline microstructures are very dynamic during wear until a steady state grain size is reached. This is significant since material properties are highly dependent on the grain structure and the grain boundary network within nanocrystalline systems.

CHAPTER 6. Conclusions

Due to the novel mechanisms by which nanocrystalline materials deform during plastic deformation, which in turn affects their mechanical response, they have been a topic of scientific interest for the past several years. In order to tailor these materials for use in engineering, a complete understanding of how these new mechanisms alter microstructure must be possessed. While the majority of research to date focuses on specific observations of how grain boundary mechanisms can alter a certain grain boundary or atomic structural arrangement, this thesis aims to extend scientific knowledge by providing a truly quantitative analysis of how nanocrystalline plasticity alters the microstructure. The conclusions drawn from this thesis are in the following paragraphs.

In Chapter 2, we presented the Grain Tracking Algorithm, a tool which characterizes the microstructure of simulated atomistic materials. Specifically, this quantitative tool identifies crystallites, crystallographic orientation, and sample texture in atomistic microstructures without any apriori knowledge of the crystalline arrangements. This tool also documents the evolution of these features during the atomistic simulation by mapping these features between time steps. In addition, the output data is presented in a way that parallels the visualization methods used in traditional experimental techniques. The utility of the algorithm is illustrated by analyzing several types of simulation cells which are commonly found in the atomistic modeling literature, but could also be applied to a variety of other atomistic studies which require precise identification and tracking of microstructure.

In Chapter 3, Molecular dynamics simulations were used to quantify mechanically-induced structural evolution in nanocrystalline Al with an average grain size of 5 nm. A polycrystalline sample was cyclically strained at different temperatures, while the Grain Tracking Algorithm was used to measure the relative contributions of novel deformation mechanisms such as grain rotation and grain sliding. Sample texture and grain size were also tracked during cycling, to show how nanocrystalline plasticity rearranges overall grain structure and alters the grain boundary network. While no obvious texture developed during cycling, the processes responsible for plasticity did act collectively to alter the interfacial network. Cyclic loading led to the formation of many twin boundaries throughout the sample as well as the occasional coalescence of neighboring grains, with higher temperatures causing more evolution. A temperature-dependent cyclic strengthening effect was observed, demonstrating that both the structure and properties of nanocrystalline metals can be dynamic during loading.

In Chapter 4, we extend our study of cyclic plasticity to involve complete characterization of grain boundary networks in nanocrystalline Al. Molecular dynamics simulations were used to study grain boundary restructuring during both monotonic tension and cyclic loading. This task was enabled by the creation of new analysis techniques within the Grain Tracking Algorithm that allowed for a complete characterization and tracking of microstructural descriptors of the grain boundary network. Quantitative measurements of grain boundary character distribution, triple junction type, grain boundary plane normal, and other interfacial network characteristics were extracted and it was found that nanocrystalline plasticity leads to an increase in special boundary fraction as well as the disruption of two-dimensional boundary connectivity. The magnitude of grain boundary network restructuring was found to have a strong temperature dependence in

addition to grain size dependence with higher temperatures and smaller average grain size experiencing more network evolution.

In Chapter 5, we carry out an experimental analysis which drives grain structural evolution using abrasive wear testing. While previous literature has shown post-deformed evidence of subsurface tribolayers, this work is the first which captures the initiation and evolution of such a layer as it evolves from an as-deposited grain size which is near the crystalline/amorphous limit. During our TEM analysis we observe evidence that the microstructure is evolving through nanocrystalline plasticity mechanisms until a state is reached where a crossover to dislocation-based plasticity occurs. We find that this evolution is very similar to our atomistic analyses of nanocrystalline Al and find that our prior computational results help to explain the majority of the evolution observed in these experiments.

As a final note, the scientific findings of this thesis reveal that nanocrystalline grain structure and grain boundary networks are dynamic during plasticity and can act collectively to cause large-scale changes to the microstructure. The ability of grain boundary-dominated mechanisms to significantly alter grain boundary networks also has important implications regarding grain boundary engineering of nanocrystalline materials. It is our hope that these findings, as well as our contribution of several quantitative microstructure characterization techniques, will be utilized in further developing our understanding of nanocrystalline metals so that their use may flourish in the next generation of mechanical and aerospace designs.

CHAPTER 7. Directions for Future Work

Throughout the course of this doctoral research sprang new ideas which could be of interest for future exploration and areas of past research which could be extrapolated upon:

- It was found in Chapters 3 and 4 that the grain boundary network of nanocrystalline Al evolved to a lower energy state as a result of cyclic plasticity, with evidence of certain boundary types exhibiting energy minima. Although many low-energy boundary configurations are known, several others likely exist but have yet to be discovered due to the infinite number of boundary normal and disorientation combinations which define interfacial structure. One such way to discover other interesting boundary types would be to characterize several samples which contain thousands of boundaries in order to provide enough statistics to relate boundary energy, disorientation, and grain boundary plane normal. This study could be facilitated through use of the Grain Tracking Algorithm.
- Even though the Poisson-Voronoi tessellation is a common method in the literature for creating atomistic microstructures, several new methods have been developed which aim to generate more realistic renditions of microstructure, for example the two isotropic grain growth models which were analyzed in section 4.4.3. Recently there has been much speculation but minimal work which points out in a quantitative fashion the differences in grain structure and boundary network topology between thermally relaxed Voronoi microstructures with that of the newly developed methods. It would be beneficial to materials scientists to have a breakdown of how these microstructures differ regarding special boundary fraction, triple junction fraction, grain structure, boundary character, and

topological connectivity of these features so that better justification can be made when researchers select a method for microstructure generation.

- In the wear experiments of Chapter 5 we document the evolution of a surface grain growth layer which has coarsened significantly with respect to the as-deposited microstructure. Other literature exists which discovers the opposite when the starting microstructure is coarse grained, specifically, a nanocrystalline tribolayer which forms through dislocation substructures. No study currently exists which documents the evolution of both of these phenomena in the same material system. Once formed, do the layers eventually saturate to the same steady state grain size during cycling? Is the steady state layer structurally similar?
- Another possible extension of our work in Chapter 5: Other studies of nanocrystalline wear have shown that the formation and permanence of the tribolayer is highly dependent on the friction coefficient, with higher coefficients leading to fracture and removal of the evolved surface layer and lower coefficients allowing for the gradual evolution of the subsurface microstructure. Additional studies which closely track microstructural evolution and wear tribology of the Ni-W system with different nanocrystalline grain sizes, sliding speeds, and wear loads should be conducted to see how each of these variables affects evolution. Deformation mechanism maps can then be developed, allowing engineers to predict which deformation mode should be active for a particular wear application.
- It has previously been shown that solid solution additions to nanocrystalline materials can lead to strengthening or softening of the material [185], with strengthening linked to improved elastic properties of the material due to the solute addition [186]. Atomistic simulations or wear tests could be conducted on different material systems such as Cu-Ni

and Cu-Pb to quantify how solid solution strengthening and softening affects the contributions and/or rate at which grain boundary-mediated mechanisms dictate nanocrystalline plasticity.

REFERENCES

[1] Kumar KS, Van Swygenhoven H, Suresh S. Mechanical behavior of nanocrystalline metals and alloys. *Acta Mater.* 2003;51:5743.

[2] Lu L, Sui ML, Lu K. Superplastic extensibility of nanocrystalline copper at room temperature. *Science* 2000;287:1463.

[3] Lu L, Shen Y, Chen X, Qian L, Lu K. Ultrahigh strength and high electrical conductivity in copper. *Science* 2004;304:422.

[4] Dao M, Lu L, Asaro RJ, De Hosson JTM, Ma E. Toward a quantitative understanding of mechanical behavior of nanocrystalline metals. *Acta Mater.* 2007;55:4041.

[5] Weertman JR, Farkas D, Hemker K, Kung H, Mayo M, Mitra R, Van Swygenhoven H. Structure and mechanical behavior of bulk nanocrystalline materials. *MRS Bull.* 1999;24:44.

[6] Padilla HA, Boyce BL. A Review of Fatigue Behavior in Nanocrystalline Metals. *Exp. Mech.* 2010;50:5.

[7] Hanlon T, Tabachnikova ED, Suresh S. Fatigue behavior of nanocrystalline metals and alloys. *Int. J. Fatigue* 2005;27:1147.

[8] Schuh CA, Nieh TG, Yamasaki T. Hall-Petch breakdown manifested in abrasive wear resistance of nanocrystalline nickel. *Scripta Mater.* 2002;46:735.

[9] Zhang YS, Han Z, Wang K, Lu K. Friction and wear behaviors of nanocrystalline surface layer of pure copper. *Wear* 2006;260:942.

[10] Hall EO. The Deformation and Ageing of Mild Steel .3. Discussion of Results. *P. Phys. Soc. Lond. B* 1951;64:747.

[11] Petch NJ. The Cleavage Strength of Polycrystals. *J. Iron. Steel. I* 1953;174:25.

[12] Khan AS, Suh YS, Chen X, Takacs L, Zhang HY. Nanocrystalline aluminum and iron: Mechanical behavior at quasi-static and high strain rates, and constitutive modeling. *Int. J. Plasticity* 2006;22:195.

[13] Mohamed FA. Interpretation of nanoscale softening in terms of dislocation-accommodated boundary sliding. *Metall Mater Trans A* 2007;38A:340.

[14] Elsherik AM, Erb U, Palumbo G, Aust KT. Deviations from Hall-Petch Behavior in as-Prepared Nanocrystalline Nickel. *Scripta Metall. Mater.* 1992;27:1185.

[15] Chokshi AH, Rosen A, Karch J, Gleiter H. On the Validity of the Hall-Petch Relationship in Nanocrystalline Materials. *Scripta Metall. Mater.* 1989;23:1679.

[16] Trelewicz JR, Schuh CA. The Hall-Petch breakdown in nanocrystalline metals: A crossover to glass-like deformation. *Acta Mater.* 2007;55:5948.

[17] Koch CC, Narayan J. The Inverse Hall-Petch Effect—Fact or Artifact? MRS Proceedings, vol. 634: Cambridge Univ Press, 2000. p.B5. 1.1.

[18] Ke M, Hackney SA, Milligan WW, Aifantis EC. Observation and Measurement of Grain Rotation and Plastic Strain in Nanostructured Metal Thin-Films. *Nanostruct. Mater.* 1995;5:689.

[19] Shan ZW, Stach EA, Wiezorek JMK, Knapp JA, Follstaedt DM, Mao SX. Grain boundary-mediated plasticity in nanocrystalline nickel. *Science* 2004;305:654.

[20] Ma E. Watching the nanograins roll. *Science* 2004;305:623.

[21] Harris KE, Singh VV, King AH. Grain rotation in thin films of gold. *Acta Mater.* 1998;46:2623.

[22] Legros M, Gianola DS, Hemker KJ. In situ TEM observations of fast grain-boundary motion in stressed nanocrystalline aluminum films. *Acta Mater.* 2008;56:3380.

[23] Rupert TJ, Gianola DS, Gan Y, Hemker KJ. Experimental Observations of Stress-Driven Grain Boundary Migration. *Science* 2009;326:1686.

[24] Kobler A, Kashiwar A, Hahn H, Kubel C. Combination of in situ straining and ACOM TEM: A novel method for analysis of plastic deformation of nanocrystalline metals. *Ultramicroscopy* 2013;128:68.

[25] Schiotz J, Vegge T, Di Tolla FD, Jacobsen KW. Atomic-scale simulations of the mechanical deformation of nanocrystalline metals. *Phys. Rev. B* 1999;60:11971.

[26] Schiotz J. Atomic-scale modeling of plastic deformation of nanocrystalline copper. *Scr. Mater.* 2004;51:837.

[27] Schiotz J, Jacobsen KW. A maximum in the strength of nanocrystalline copper. *Science* 2003;301:1357.

[28] Van Swygenhoven H, Derlet PA. Grain-boundary sliding in nanocrystalline fcc metals. *Phys. Rev. B* 2001;64.

[29] Van Swygenhoven H, Derlet PM, Froseth AG. Stacking fault energies and slip in nanocrystalline metals. *Nat. Mater.* 2004;3:399.

[30] Derlet PM, Van Swygenhoven H, Hasnaoui A. Atomistic simulation of dislocation emission in nanosized grain boundaries. *Philos. Mag.* 2003;83:3569.
[31] Van Swygenhoven H, Derlet PM, Hasnaoui A. Atomic mechanism for dislocation emission from nanosized grain boundaries. *Phys. Rev. B* 2002;66.
[32] Van Swygenhoven H, Derlet PM, Froseth AG. Nucleation and propagation of dislocations in nanocrystalline fcc metals. *Acta Mater.* 2006;54:1975.
[33] Stukowski A. Structure identification methods for atomistic simulations of crystalline materials. *Modell. Simul. Mater. Sci. Eng.* 2012;20.
[34] Stukowski A, Albe K. Extracting dislocations and non-dislocation crystal defects from atomistic simulation data. *Modell. Simul. Mater. Sci. Eng.* 2010;18:085001.
[35] Stukowski A, Bulatov VV, Arsenlis A. Automated identification and indexing of dislocations in crystal interfaces. *Modell. Simul. Mater. Sci. Eng.* 2012;20:085007.
[36] Tucker GJ, Foiles SM. Molecular dynamics simulations of rate-dependent grain growth during the surface indentation of nanocrystalline nickel. *Mater. Sci. Eng. A* 2013;571:207.
[37] Barrett CD, Tschopp MA, El Kadiri H. Automated analysis of twins in hexagonal close-packed metals using molecular dynamics. *Scr. Mater.* 2012;66:666.
[38] Tucker GJ, Zimmerman JA, McDowell DL. Continuum metrics for deformation and microrotation from atomistic simulations: Application to grain boundaries. *Int. J. Eng. Sci.* 2011;49:1424.
[39] Xu T, Li M. Geometric methods for microstructure rendition and atomic characterization of poly- and nano-crystalline materials. *Philos. Mag.* 2010;90:2191.
[40] Derlet PM, Van Petegem S, Van Swygenhoven H. Calculation of x-ray spectra for nanocrystalline materials. *Phys. Rev. B* 2005;71:024114.
[41] Coleman SP, Spearot DE, Capolungo L. Virtual diffraction analysis of Ni 010 symmetric tilt grain boundaries. *Model. Simul. Mater. Sci. Eng.* 2013;21:055020.
[42] Vo NQ, Averback RS, Bellon P, Odunuga S, Caro A. Quantitative description of plastic deformation in nanocrystalline Cu: Dislocation glide versus grain boundary sliding. *Phys. Rev. B* 2008;77.
[43] Tucker GJ, Foiles SM. Quantifying the influence of twin boundaries on the deformation of nanocrystalline copper using atomistic simulations. *Int. J. Plasticity* 2015;65:191.
[44] Panchal JH, Kalidindi SR, McDowell DL. Key computational modeling issues in Integrated Computational Materials Engineering. *Comput.-Aided Des.* 2013;45:4.
[45] Kelchner CL, Plimpton SJ, Hamilton JC. Dislocation nucleation and defect structure during surface indentation. *Phys. Rev. B* 1998;58:11085.
[46] Faken D, Jonsson H. Systematic analysis of local atomic structure combined with 3D computer graphics. *Comput. Mater. Sci.* 1994;2:279.
[47] Tsuzuki H, Branicio PS, Rino JP. Structural characterization of deformed crystals by analysis of common atomic neighborhood. *Comput. Phys. Commun.* 2007;177:518.
[48] Ackland GJ, Jones AP. Applications of local crystal structure measures in experiment and simulation. *Phys. Rev. B* 2006;73:054104.
[49] Plimpton S. Fast parallel algorithms for short-range molecular-dynamics. *J. Comput. Phys.* 1995;117:1.
[50] Gilvarry JJ. THE LINDEMANN AND GRUNEISEN LAWS. *Phys. Rev.* 1956;102:308.
[51] Mishin Y, Farkas D, Mehl MJ, Papaconstantopoulos DA. Interatomic potentials for monoatomic metals from experimental data and ab initio calculations. *Phys. Rev. B* 1999;59:3393.
[52] Stukowski A. Visualization and analysis of atomistic simulation data with OVITO-the Open Visualization Tool. *Modell. Simul. Mater. Sci. Eng.* 2010;18:015012.
[53] Spearot DE, Jacob KI, McDowell DL. Nucleation of dislocations from 001 bicrystal interfaces in aluminum. *Acta Mater.* 2005;53:3579.
[54] Cahn JW, Mishin Y, Suzuki A. Coupling grain boundary motion to shear deformation. *Acta Mater.* 2006;54:4953.
[55] Farkas D, Patrick L. Tensile deformation of fcc Ni as described by an EAM potential. *Philos. Mag.* 2009;89:3435.
[56] Yamakov V, Wolf D, Phillpot SR, Mukherjee AK, Gleiter H. Dislocation processes in the deformation of nanocrystalline aluminium by molecular-dynamics simulation. *Nat. Mater.* 2002;1:45.
[57] Lund AC, Schuh CA. Strength asymmetry in nanocrystalline metals under multiaxial loading. *Acta Mater.* 2005;53:3193.
[58] Bitzek E, Derlet PM, Anderson PM, Van Swygenhoven H. The stress-strain response of nanocrystalline metals: A statistical analysis of atomistic simulations. *Acta Mater.* 2008;56:4846.

[59] Rupert TJ, Schuh CA. Mechanically driven grain boundary relaxation: a mechanism for cyclic hardening in nanocrystalline Ni. *Philos. Mag. Lett.* 2012;92:20.
[60] Tabachnikova ED, Podolskiy AV, Bengus VZ, Smirnov SN, Bidylo MI, Li H, Liaw PK, Choo H, Csach K, Miskuf J. Mechanical properties of nanocrystalline Ni-20%Fe alloy at temperatures from 300 to 4.2 K. *Mater. Sci. Eng. A* 2009;503:110.
[61] Monk J, Farkas D. Strain-induced grain growth and rotation in nickel nanowires. *Phys. Rev. B* 2007;75:045414.
[62] VanSwygenhoven H, Caro A. Molecular dynamics computer simulation of nanophase Ni: Structure and mechanical properties. *Nanostruct. Mater.* 1997;9:669.
[63] Meyers MA, Mishra A, Benson DJ. Mechanical properties of nanocrystalline materials. *Prog. Mater. Sci.* 2006;51:427.
[64] Schiotz J, Di Tolla FD, Jacobsen KW. Softening of nanocrystalline metals at very small grain sizes. *Nature* 1998;391:561.
[65] Farkas D, Mohanty S, Monk J. Linear grain growth kinetics and rotation in nanocrystalline Ni. *Phys. Rev. Lett.* 2007;98:165502.
[66] Cahn JW, Taylor JE. A unified approach to motion of grain boundaries, relative tangential translation along grain boundaries, and grain rotation. *Acta Mater.* 2004;52:4887.
[67] Hasnaoui A, Van Swygenhoven H, Derlet PM. Cooperative processes during plastic deformation in nanocrystalline fcc metals: A molecular dynamics simulation. *Phys. Rev. B* 2002;66:184112.
[68] Hahn H, Padmanabhan KA. A model for the deformation of nanocrystalline materials. *Philos. Mag. B-Phys. Condens. Matter Stat. Mech. Electron. Opt. Magn. Prop.* 1997;76:559.
[69] Rupert TJ. Strain localization in a nanocrystalline metal: Atomic mechanisms and the effect of testing conditions. *J. Appl. Phys.* 2013;114.
[70] Haslam AJ, Moldovan D, Yamakov V, Wolf D, Phillpot SR, Gleiter H. Stress-enhanced grain growth in a nanocrystalline material by molecular-dynamics simulation. *Acta Mater.* 2003;51:2097.
[71] Cheng S, Stoica AD, Wang XL, Wang GY, Choo H, Liaw PK. Fracture of Ni with grain-size from nanocrystalline to ultrafine scale under cyclic loading. *Scr. Mater.* 2007;57:217.
[72] Moser B, Hanlon T, Kumar KS, Suresh S. Cyclic strain hardening of nanocrystalline nickel. *Scr. Mater.* 2006;54:1151.
[73] Witney AB, Sanders PG, Weertman JR, Eastman JA. Fatigue of Nanocrystalline Copper. *Scr. Metall. Mater.* 1995;33:2025.
[74] Schiotz J. Strain-induced coarsening in nanocrystalline metals under cyclic deformation. *Mater. Sci. Eng. A* 2004;375:975.
[75] Voronoi G. New applications of continuous parameters to the theory of quadratic forms. - First memoir - Some properties of perfect positive quadratic forms. *Journal Fur Die Reine Und Angewandte Mathematik* 1908;133:97.
[76] Tucker GJ, Tiwari S, Zimmerman JA, McDowell DL. Investigating the deformation of nanocrystalline copper with microscale kinematic metrics and molecular dynamics. *J. Mech. Phys. Solids* 2012;60:471.
[77] Van Swygenhoven H, Farkas D, Caro A. Grain-boundary structures in polycrystalline metals at the nanoscale. *Phys. Rev. B* 2000;62:831.
[78] Van Swygenhoven H, Caro A. Plastic behavior of nanophase metals studied by molecular dynamics. *Phys. Rev. B* 1998;58:11246.
[79] Lesar R. Introduction To Computational Materials Science. United States of America: Cambridge University Press, 2013.
[80] Gianola DS, Van Petegem S, Legros M, Brandstetter S, Van Swygenhoven H, Hemker KJ. Stress-assisted discontinuous grain growth and its effect on the deformation behavior of nanocrystalline aluminum thin films. *Acta Mater.* 2006;54:2253.
[81] Tucker GJ, McDowell DL. Non-equilibrium grain boundary structure and inelastic deformation using atomistic simulations. *Int. J. Plast.* 2011;27:841.
[82] Vo NQ, Averback RS, Bellon P, Caro A. Limits of hardness at the nanoscale: Molecular dynamics simulations. *Phys. Rev. B* 2008;78:241402.
[83] Brandl C, Derlet PM, Van Swygenhoven H. Strain rates in molecular dynamics simulations of nanocrystalline metals. *Philos. Mag.* 2009;89:3465.
[84] Dalla Torre F, Van Swygenhoven H, Victoria M. Nanocrystalline electrodeposited Ni: microstructure and tensile properties. *Acta Mater.* 2002;50:3957.

[85] Schwaiger R, Moser B, Dao M, Chollacoop N, Suresh S. Some critical experiments on the strain-rate sensitivity of nanocrystalline nickel. *Acta Mater.* 2003;51:5159.
[86] Gianola DS, Warner DH, Molinari JF, Hemker KJ. Increased strain rate sensitivity due to stress-coupled grain growth in nanocrystalline Al. *Scr. Mater.* 2006;55:649.
[87] Wang L, Teng J, Liu P, Hirata A, Ma E, Zhang Z, Chen M, Han X. Grain rotation mediated by grain boundary dislocations in nanocrystalline platinum. *Nat. Comm.* 2014;5:4402.
[88] Panzarino JF, Rupert TJ. Tracking Microstructure of Crystalline Materials: A Post-Processing Algorithm for Atomistic Simulations. *JOM* 2014;65:417.
[89] Savitzky A, Golay MJE. Smoothing & Differentiation of Data By Simplified Least Squares Procedures. *Anal. Chem.* 1964;36:1627.
[90] Ashby MF, Verrall RA. Diffusion-Accommodated Flow and Superplasticity. *Acta Metall.* 1973;21:149.
[91] Harris K, Singh V, King A. Grain rotation in thin films of gold. *Acta Mater.* 1998;46:2623.
[92] Moldovan D, Wolf D, Phillpot S. Theory of diffusion-accommodated grain rotation in columnar polycrystalline microstructures. *Acta Mater.* 2001;49:3521.
[93] Upmanyu M, Srolovitz DJ, Lobkovsky AE, Warren JA, Carter WC. Simultaneous grain boundary migration and grain rotation. *Acta Mater.* 2006;54:1707.
[94] Gutkin MY, Ovid'ko IA, Skiba NV. Crossover from grain boundary sliding to rotational deformation in nanocrystalline materials. *Acta Mater.* 2003;51:4059.
[95] Ovid'ko IA, Sheinerman AG. Special rotational deformation in nanocrystalline metals and ceramics. *Scr. Mater.* 2008;59:119.
[96] Patala S, Mason JK, Schuh CA. Improved representations of misorientation information for grain boundary science and engineering. *Prog. Mater. Sci.* 2012;57:1383.
[97] Moldovan D, Wolf D, Phillpot S, Haslam A. Role of grain rotation during grain growth in a columnar microstructure by mesoscale simulation. *Acta Mater.* 2002;50:3397.
[98] Rupert TJ, Schuh CA. Sliding wear of nanocrystalline Ni-W: Structural evolution and the apparent breakdown of Archard scaling. *Acta Mater* 2010;58:4137.
[99] Yip S. Nanocrystals: the strongest size. 1998;391:532.
[100] Haque M, A Saif M. Mechanical behavior of 30–50 nm thick aluminum films under uniaxial tension. *Scr. Mater.* 2002;47:863.
[101] Chan S-W, Balluffi R. Study of energy vs misorientation for grain boundaries in gold by crystallite rotation method—II. Tilt boundaries and mixed boundaries. *Acta Metall.* 1986;34:2191.
[102] Chan S-W, Balluffi R. Study of energy vs misorientation for grain boundaries in gold by crystallite rotation method—I.[001] twist boundaries. *Acta Metall.* 1985;33:1113.
[103] Erb U, Gleiter H. The effect of temperature on the energy and structure of grain boundaries. *Scr. Metall.* 1979;13:61.
[104] Rupert TJ, Trelewicz JR, Schuh CA. Grain boundary relaxation strengthening of nanocrystalline Ni-W alloys. *J. Mater. Res.* 2012;27:1285.
[105] Ebrahimi F, Li HQ. The effect of annealing on deformation and fracture of a nanocrystalline fcc metal. *J. Mater. Sci.* 2007;42:1444.
[106] Brandon D. The structure of high-angle grain boundaries. *Acta Metall.* 1966;14:1479.
[107] Gottstein G, Molodov DA, Shvindlerman LS. Grain boundary migration in metals: Recent developments. *Interface Sci.* 1998;6:7.
[108] Lu L, Shen YF, Chen XH, Qian LH, Lu K. Ultrahigh strength and high electrical conductivity in copper. *Science* 2004;304:422.
[109] Zhu YT, Liao XZ, Wu XL. Deformation twinning in nanocrystalline materials. *Prog. Mater. Sci.* 2012;57:1.
[110] Wu XL, Zhu YT. Inverse grain-size effect on twinning in nanocrystalline Ni. *Phys. Rev. Lett.* 2008;101:025503.
[111] Wang L, Teng J, Liu P, Hirata A, Ma E, Zhang Z, Chen MW, Han X. Grain rotation mediated by grain boundary dislocations in nanocrystalline platinum. *Nat. Commun.* 2014;5:5402.
[112] Farkas D, Froseth A, Van Swygenhoven H. Grain boundary migration during room temperature deformation of nanocrystalline Ni. *Scr. Mater.* 2006;55:695.
[113] Schuh CA, Kumar M, King WE. Analysis of grain boundary networks and their evolution during grain boundary engineering. *Acta Mater.* 2003;51:687.
[114] Grimmer H, Bollmann W, Warrington DH. Coincidence-Site Lattices and Complete Pattern-Shift Lattices in Cubic-Crystals. *Acta Crystallogr., Sect. A* 1974;A 30:197.

[115] Bober DB, Kumar M, Rupert TJ. Nanocrystalline grain boundary engineering: Increasing Sigma 3 boundary ction in pure Ni with thermomechanical treatments. *Acta Mater.* 2015;86:43.
[116] Lejcek P. Grain boundary segregation in metals: Springer Science & Business Media, 2010.
[117] Mishin Y, Farkas D, Mehl M, Papaconstantopoulos D. Interatomic potentials for monoatomic metals from experimental data and ab initio calculations. *Phys. Rev. B* 1999;59:3393.
[118] Hasnaoui A, Van Swygenhoven H, Derlet PM. On non-equilibrium grain boundaries and their effect on thermal and mechanical behaviour: a molecular dynamics computer simulation. *Acta Mater.* 2002;50:3927.
[119] Zhang T, Zhou K, Chen Z. Strain rate effect on plastic deformation of nanocrystalline copper investigated by molecular dynamics. *Mater. Sci. Eng., A* 2015;648:23.
[120] Faken D, Jónsson H. Systematic analysis of local atomic structure combined with 3D computer graphics. *Comput. Mater. Sci.* 1994;2:279.
[121] Liu X, Choi D, Beladi H, Nuhfer NT, Rohrer GS, Barmak K. The five-parameter grain boundary character distribution of nanocrystalline tungsten. *Scr. Mater.* 2013;69:413.
[122] Kelly MN, Glowinski K, Nuhfer NT, Rohrer GS. The five parameter grain boundary character distribution of α-Ti determined from three-dimensional orientation data. *Acta Mater.* 2016;111:22.
[123] Brandon DG. Structure of High-Angle Grain Boundaries. *Acta Metall.* 1966;14:1479.
[124] King AH, Shekhar S. What does it mean to be special? The significance and application of the Brandon criterion. *J. Mater. Sci.* 2006;41:7675.
[125] Homer E, Patala S, Priedeman J. Grain Boundary Plane Orientation Fundamental Zones and Structure-Property Relationships. *Sci. Rep.* 2015;5:15476.
[126] Patala S, Schuh CA. Symmetries in the representation of grain boundary-plane distributions. *Philos. Mag.* 2013;93:524.
[127] King A, Johnson G, Engelberg D, Ludwig W, Marrow J. Observations of intergranular stress corrosion cracking in a grain-mapped polycrystal. *Science* 2008;321:382.
[128] Matsunaga K, Nishimura H, Hanyu S, Muto H, Yamamoto T, Ikuhara Y. HRTEM study on grain boundary atomic structures related to the sliding behavior in alumina bicrystals. *Appl. Surf. Sci.* 2005;241:75.
[129] Han WZ, Demkowicz MJ, Fu EG, Wang YQ, Misra A. Effect of grain boundary character on sink efficiency. *Acta Mater.* 2012;60:6341.
[130] Gertsman V, Janecek M, Tangri K. Grain boundary ensembles in polycrystals. *Acta Mater.* 1996;44:2869.
[131] Watanabe T. The Impact of Grain-Boundary-Character-Distribution on Fracture in Polycrystals. *Mater. Sci. Eng., A* 1994;176:39.
[132] Schuh CA, Minich RW, Kumar M. Connectivity and percolation in simulated grain-boundary networks. *Philos. Mag.* 2003;83:711.
[133] Schuh CA, Kumar M, King WE. Universal features of grain boundary networks in FCC materials. *J. Mater. Sci.* 2005;40:847.
[134] Basinger J, Homer E, Fullwood D, Adams B. Two-dimensional grain boundary percolation in alloy 304 stainless steel. *Scr. Mater.* 2005;53:959.
[135] Minich RW, Schuh CA, Kumar M. Role of topological constraints on the statistical properties of grain boundary networks. *Phys. Rev. B* 2002;66:052101.
[136] Frary M, Schuh CA. Connectivity and percolation behaviour of grain boundary networks in three dimensions. *Philos. Mag.* 2005;85:1123.
[137] Kadau K, Germann TC, Lomdahl PS, Holian BL, Kadau D, Entel P, Kreth M, Westerhoff F, Wolf DE. Molecular-dynamics study of mechanical deformation in nano-crystalline aluminum. *Metall. Mater. Trans. A* 2004;35a:2719.
[138] Wells DB, Stewart J, Herbert AW, Scott PM, Williams DE. The Use of Percolation Theory to Predict the Probability of Failure of Sensitized, Austenitic Stainless-Steels by Intergranular Stress-Corrosion Cracking. *Corrosion* 1989;45:649.
[139] Lim LC, Watanabe T. Fracture-toughness and brittle-ductile transition controlled by grain-boundary character distribution (GBCD) in polycrystals. *Acta Metall. Mater.* 1990;38:2507.
[140] Palumbo G, King PJ, Aust KT, Erb U, Lichtenberger PC. Grain-Boundary Design and Control for Intergranular Stress-Corrosion Resistance. *Scr. Metall. Mater.* 1991;25:1775.
[141] Gertsman VY, Tangri K. Modelling of intergranular damage propagation. *Acta Mater.* 1997;45:4107.
[142] Ikuhara Y, Watanabe T, Yamamoto T, Saito T, Yoshida H, Sakuma T. Grain boundary structure and sliding of alumina bicrystals. *Mater. Res. Soc. Symp. P.* 2000;601:125.
[143] Tsurekawa S, Nakamichi S, Watanabe T. Correlation of grain boundary connectivity with grain boundary character distribution in austenitic stainless steel. *Acta Mater.* 2006;54:3617.

[144] Olmsted DL, Foiles SM, Holm EA. Survey of computed grain boundary properties in face-centered cubic metals: I. Grain boundary energy. *Acta Mater.* 2009;57:3694.
[145] Merkle K, Wolf D. Low-energy configurations of symmetric and asymmetric tilt grain boundaries†. *Philos. Mag. A* 1992;65:513.
[146] Panzarino JF, Ramos JJ, Rupert TJ. Quantitative tracking of grain structure evolution in a nanocrystalline metal during cyclic loading. *Modell. Simul. Mater. Sci. Eng.* 2015;23:025005.
[147] Erb U, Gleiter H. Effect of Temperature on the Energy and Structure of Grain-Boundaries. *Scr. Metall.* 1979;13:61.
[148] Herrmann G, Gleiter H, Baro G. Investigation of Low-Energy Grain-Boundaries in Metals by a Sintering Technique. *Acta Metall.* 1976;24:353.
[149] Xu T, Li M. Topological and statistical properties of a constrained Voronoi tessellation. *Philos. Mag.* 2009;89:349.
[150] Gross D, Li M. Constructing microstructures of poly-and nanocrystalline materials for numerical modeling and simulation. *Appl. Phys. Lett.* 2002;80:746.
[151] Li M, Xu T. Topological and atomic scale characterization of grain boundary networks in polycrystalline and nanocrystalline materials. *Prog. Mater. Sci.* 2011;56:864.
[152] Leonardi A, Scardi P, Leoni M. Realistic nano-polycrystalline microstructures: beyond the classical Voronoi tessellation. *Philos. Mag.* 2012;92:986.
[153] Leonardi A, Leoni M, Scardi P. Atomistic modelling of polycrystalline microstructures: An evolutional approach to overcome topological restrictions. *Comput. Mater. Sci.* 2013;67:238.
[154] Lazar EA, Mason JK, MacPherson RD, Srolovitz DJ. A more accurate three-dimensional grain growth algorithm. *Acta Mater.* 2011;59:6837.
[155] Syha M, Weygand D. A generalized vertex dynamics model for grain growth in three dimensions. *Modell. Simul. Mater. Sci. Eng.* 2010;18:015010.
[156] MacPherson RD, Srolovitz DJ. The von Neumann relation generalized to coarsening of three-dimensional microstructures. *Nature* 2007;446:1053.
[157] Prakash A, Hummel M, Schmauder S, Bitzek E. Nanosculpt: A methodology for generating complex realistic configurations for atomistic simulations. *MethodsX* 2016;3:219.
[158] Bringa EM, Farkas D, Caro A, Wang YM, McNaney J, Smith R. Fivefold twin formation during annealing of nanocrystalline Cu. *Scr. Mater.* 2008;59:1267.
[159] Mishra R, Basu B, Balasubramaniam R. Effect of grain size on the tribological behavior of nanocrystalline nickel. *Mat Sci Eng a-Struct* 2004;373:370.
[160] Wang LP, Gao Y, Xu T, Xue QJ. A comparative study on the tribological behavior of nanocrystalline nickel and cobalt coatings correlated with grain size and phase structure. *Mater Chem Phys* 2006;99:96.
[161] Jeong DH, Gonzalez F, Palumbo G, Aust KT, Erb U. The effect of grain size on the wear properties of electrodeposited nanocrystalline nickel coatings. *Scripta Mater* 2001;44:493.
[162] Farhat ZN, Ding Y, Northwood DO, Alpas AT. Effect of grain size on friction and wear of nanocrystalline aluminum. *Mat Sci Eng a-Struct* 1996;206:302.
[163] Hughes DA, Dawson DB, Korellis JS, Weingarten LI. Near-Surface Microstructures Developing under Large Sliding Loads. *J Mater Eng Perform* 1994;3:459.
[164] Rigney DA, Glaeser WA. Significance of near-Surface Microstructure in Wear Process. *Wear* 1978;46:241.
[165] Emge A, Karthikeyan S, Rigney DA. The effects of sliding velocity and sliding time on nanocrystalline tribolayer development and properties in copper. *Wear* 2009;267:562.
[166] Singh JB, Cai W, Bellon P. Dry sliding of Cu-15 wt%Ni-8 wt%Sn bronze: Wear behaviour and micro structures. *Wear* 2007;263:830.
[167] Singh JB, Wen JG, Bellon P. Nanoscale characterization of the transfer layer formed during dry sliding of Cu-15 wt.% Ni-8 wt.% Sn bronze alloy. *Acta Mater* 2008;56:3053.
[168] Rigney DA, Chen LH, Naylor MGS, Rosenfield AR. Wear Processes in Sliding Systems. *Wear* 1984;100:195.
[169] Cashion JD, Aghan RL, Doyle ED. Mossbauer Study of Fine Grinding Chips. *Scripta Metall. Mater.* 1974;8:1261.
[170] Turley DM, Samuels LE. The Nature of Mechanically Polished Surfaces of Copper. *Metallography* 1981;14:275.
[171] Doyle ED, Aghan RL. Mechanism of metal removal in the polishing and fine grinding of hard metals. *Metall. Mater. Trans. B* 1975;6:143.

[172] Hanlon T, Chokshi AH, Manoharan M, Suresh S. Effects of grain refinement and strength on friction and damage evolution under repeated sliding contact in nanostructured metals. *Int. J. Fatigue* 2005;27:1159.
[173] Qi ZQ, Jiang JC, Meletis EI. Wear Mechanism of Nanocrystalline Metals. *J. Nanosci. Nanotechno.* 2009;9:4227.
[174] Prasad SV, Battaile CC, Kotula PG. Friction transitions in nanocrystalline nickel. *Scripta Mater.* 2011;64:729.
[175] Padilla HA, Boyce BL, Battaile CC, Prasad SV. Frictional performance and near-surface evolution of nanocrystalline Ni–Fe as governed by contact stress and sliding velocity. *Wear* 2013;297:860.
[176] Argibay N, Furnish T, Boyce B, Clark B, Chandross M. Stress-dependent grain size evolution of nanocrystalline Ni-W and its impact on friction behavior. *Scr. Mater.* 2016;123:26.
[177] Detor AJ, Schuh CA. Tailoring and patterning the grain size of nanocrystalline alloys. *Acta Mater.* 2007;55:371.
[178] Giannuzzi LA. Introduction to focused ion beams: instrumentation, theory, techniques and practice: Springer Science & Business Media, 2006.
[179] Khalajhedayati A, Rupert TJ. Disruption of Thermally-Stable Nanoscale Grain Structures by Strain Localization. *Sci. Rep-Uk* 2015;5.
[180] Schuh CA, Nieh TG, Iwasaki H. The effect of solid solution W additions on the mechanical properties of nanocrystalline Ni. *Acta Mater.* 2003;51:431.
[181] Hamilton GM. Explicit equations for the stresses beneath a sliding spherical contact. *Proc. Inst. Mech. Eng., Part C* 1983;197:53.
[182] Sharon JA, Su PC, Prinz FB, Hemker KJ. Stress-driven grain growth in nanocrystalline Pt thin films. *Scripta Mater.* 2011;64:25.
[183] Zhang K, Weertman JR, Eastman JA. Rapid stress-driven grain coarsening in nanocrystalline Cu at ambient and cryogenic temperatures. *Appl. Phys. Lett.* 2005;87.
[184] Panzarino JF, Pan Z, Rupert TJ. Plasticity-induced restructuring of a nanocrystalline grain boundary network. *Acta Mater. In Press*.
[185] Rupert TJ, Trenkle JC, Schuh CA. Enhanced solid solution effects on the strength of nanocrystalline alloys. *Acta Mater.* 2011;59:1619.
[186] Rupert TJ. Solid solution strengthening and softening due to collective nanocrystalline deformation physics. *Scripta Mater.* 2014;81:44.